

OVERSHOOT AND SHRINKAGE IN CLASSIFIER-FREE GUIDANCE: FROM THEORY TO PRACTICE

000
001
002
003
004
005 **Anonymous authors**
006 Paper under double-blind review
007
008
009
010

ABSTRACT

011 Classifier-Free Guidance (CFG) is widely used in diffusion and flow-based gener-
012 ative models for high-quality conditional generation, yet its theoretical properties
013 remain incompletely understood. By connecting CFG to the high-dimensional
014 framework of diffusion regimes, we show that in sufficiently high dimensions it
015 reproduces the correct target distribution—a “blessing-of-dimensionality” result.
016 Leveraging this theoretical framework, we analyze how the well-known artifacts
017 of mean overshoot and variance shrinkage emerge in lower dimensions, character-
018 izing how they become more pronounced as dimensionality decreases. Build-
019 ing on these insights, we propose a simple nonlinear extension of CFG, proving
020 that it mitigates both effects while preserving CFG’s practical benefits. Finally,
021 we validate our approach through numerical simulations on Gaussian mixtures
022 and real-world experiments on diffusion and flow-matching state-of-the-art class-
023 conditional and text-to-image models, demonstrating continuous improvements in
024 sample quality, diversity, and consistency.



025
026
027
028
029
030
031
032
033
034
035
036
037
038 **Figure 1: Qualitative comparison of unguided sampling, standard Classifier-Free Guidance (CFG), and**
039 **our proposed non-linear power-law CFG (DiT/XL-2 on ImageNet-1K 256 × 256).** Standard CFG increases
040 fidelity at a substantial expense to diversity and semantic meaning compared to unguided CFG. Our power-law
041 guidance improves fidelity at no cost to semantics or diversity. Each column sample starts from the same seed.

1 INTRODUCTION

044 Diffusion (Sohl-Dickstein et al., 2015; Song & Ermon, 2020; Ho et al., 2020) and flow-based
045 methods (Lipman et al., 2022; Albergo et al., 2023; Liu et al., 2022) have emerged as the de facto
046 state-of-the-art for generating high-dimensional signals. Diffusion relies on Orstein-Uhlenbeck
047 Langevin dynamics, where noise is progressively added to the data until it becomes completely
048 random. New samples are generated by reversing this process through a time-reversed Langevin
049 equation. This backward evolution is steered by a force, the *score*, estimated from the data. In
050 contrast, flow matching circumvents the diffusion construction by directly specifying the probability
051 paths between noise and data. This is done by regressing onto a target vector field which in turn
052 generates the desired probability paths. An important task for both paradigms is generating data
053 conditioned on a class label or textual description of the image content. This can be achieved
through conditioning mechanisms in the model architecture, as well as guidance techniques

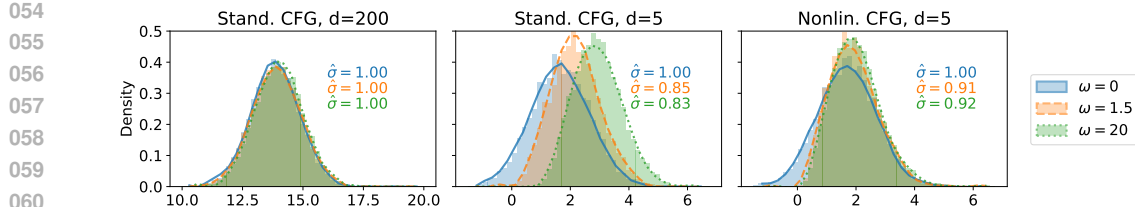


Figure 2: **CFG accurately generates the target distribution in high dimensions, causes mean overshoot and variance shrinkage in low dimensions, which are mitigated by nonlinear CFG.** We simulate the backward process using a two-Gaussian mixture with target mean $\vec{m} = (1, 1, \dots)^d$ and variance $\sigma^2 = 1$, and project the generated samples onto the target mean, $q(t=0) = \vec{x} \cdot \vec{m}/|\vec{m}|$. **Left:** in high dimensions ($d = 200$), CFG accurately recovers the target distribution. **Center:** in low dimensions ($d = 5$), CFG exhibits mean overshoot and variance shrinkage. **Right:** Our proposed nonlinear extension of CFG reduces these artifacts, partially restoring the target distribution.

(Dhariwal & Nichol, 2021; Ho & Salimans, 2022) that steer the generation process towards samples aligned with user intentions or desired properties.

The notion of guidance was first introduced in classifier guidance (Song et al., 2020; Dhariwal & Nichol, 2021), where a pre-trained classifier is leveraged to induce class conditioning in the sampling of unconditional models. Relying on a pre-trained classifier is, however, computationally expensive and requires classifiers robust to noisy samples. Classifier-free guidance (CFG) (Ho & Salimans, 2022) was developed as an alternative, and was quickly adopted as a standard technique (Nichol et al., 2022; Betker et al., 2023; Saharia et al., 2022; Esser et al., 2024). CFG does not rely on an auxiliary classifier, instead, the model is trained to generate unconditional and conditional samples, and at inference extrapolates the denoising path towards the conditional one. Using CFG, however, the process *is no longer guaranteed* to sample the original conditional distribution.

CFG affects the generation process mainly in two ways; theoretically, this has been characterized in case of Gaussian mixtures in one and finite dimensions, where CFG causes **mean overshoot**, **causing samples more shifted towards the boundary of the class, and variance shrinkage**, resulting in a sharper distribution than the target one (Chidambaram et al., 2024; Xia et al., 2024; Wu et al., 2024; Bradley & Nakkiran, 2024). These two effects are linked closely with the effects that the practitioners have observed, with CFG steering the samples towards the “mode” of high-quality and input-consistent samples corresponding directly to the well-observed increased **saturation/contrast**, while also **reducing sample diversity** in the process (Astolfi et al., 2024; Saharia et al., 2022).

Theoretically, it is unknown whether the unwanted effects can be damped and whether in fact CFG can ever generate the correct distribution. In practice, as CFG has indeed shown beneficial regardless of these effects, it would be useful if similar guidances existed that reduce these effects, while keeping the practical benefits of increased quality of the generated samples. In this work, we provide theoretical analysis of the properties of the distribution generated by CFG, and how they compare to the target one. We examine how these effects arise, what influences them, and whether they can be damped. Our results are backed by numerical simulations, and finally we test how do our findings extend to real world settings.

In summary, our contributions are the following:

(1) We provide blessing-of-dimensionality result showing that, in infinite and sufficiently high dimensions, CFG-guided trajectories generate the correct distribution, one that is generated by unguided conditional trajectories. This is established by relating CFG to the emergence of dynamical regimes (Biroli et al., 2024). In this setting, we show that CFG accelerates convergence of samples toward the target class.

(2) We demonstrate that, as dimensionality decreases, the commonly-observed artifacts of mean overshoot and variance shrinkage appear (illustrated on a toy Gaussian example in Fig. 2). We precisely characterize these effects and support our theoretical analysis with numerical simulations.

(3) Finally, we introduce a simple nonlinear generalization of CFG and prove theoretically that it mitigates both mean overshoot and variance shrinkage. We further show its superiority in numerical simulations (as in Fig. 2, right), and validate its practical benefits on state-of-the-art diffusion and flow-matching models, achieving improved sample quality, consistency, and diversity.

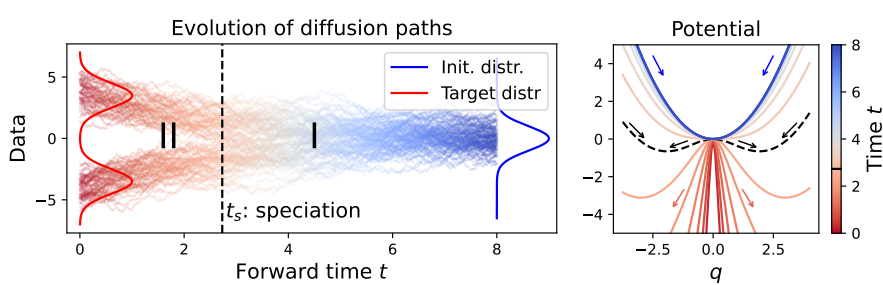


Figure 3: **Dynamical regimes in diffusion.** **Left:** Illustration of the speciation phenomenon using a one-dimensional Gaussian mixture. Starting from pure Gaussian noise at large time t , the backward diffusion begins in Regime I, where the class has not been decided yet. After speciation time t_s (dashed line), the class membership is decided. **Right:** Evolution of the effective potential (conditional potential in Eq. (6)) over time for high-dimensional Gaussian mixture showcasing the symmetry breaking phenomenon.

Our results can intuitively be described as follows: as the dimension grows, the "attraction force" for each class grows exponentially. One can visualize a well-separated class acting as a magnet that pulls diffusion trajectories towards itself (the attraction force depending on the mean and variance magnitude). During the backward process this force becomes very strong when the system starts to approach one class. Unless the magnitude of the CFG guidance scale also grows exponentially with the dimension (which is not the case in practice), these natural attraction forces completely dominate the CFG term. The backward dynamics and the attraction forces are portrayed in Figure 3 (left and right respectively).

2 RELATED WORK

Having introduced CFG, Ho & Salimans (2022) highlighted the trade-off between image quality, measured by Fréchet inception distance (FID, Heusel et al. (2017)), and diversity, measured by inception score (Salimans et al., 2016) when adjusting the guidance strength parameter ω . Since then, a significant body of research has examined CFG from various perspectives.

Theoretical works on CFG. Several works employed Gaussian mixture models (GMMs) to analyze diffusion and guidance (Shah et al., 2023; Liang et al., 2024; Cui et al., 2023; Bai et al., 2024; Song et al., 2020). In contrast, Du et al. (2023) explored alternative conditioning, while Bradley & Nakkiran (2024) characterized CFG as a predictor-corrector (Song et al., 2020). Most relevant to this work, Chidambaram et al. (2024) demonstrated CFG's mean overshoot and variance shrinkage in one-dimensional settings, while Wu et al. (2024) extended the findings to multi-dimensional settings using GMMs. We expand on these by developing a high-dimensional statistical analysis and precisely characterizing how these effects diminish as dimensionality increases, ultimately demonstrating that the CFG-generated distribution in fact aligns with the target one for $d \rightarrow \infty$.

CFG variants and experimental analyses. Among experimental analyses of CFG, Karras et al. (2024a) propose guiding generation using a less-trained version of the model, Kynkänniemi et al. (2024) apply CFG during a limited interval, and Wang et al. (2024) use weight schedulers for the classifier strength parameter. Several other CFG alternatives have been proposed, such as rectified guidance (Xia et al., 2024), projected score guidance (Kadkhodaie et al., 2024), characteristic guidance (Zheng & Lan, 2023), second-order CFG (Sun et al., 2023), CADS (Sadat et al., 2023), CFG++ (Chung et al., 2024), REG (Xia et al., 2024), APG (Sadat et al., 2024) and Feedback Guidance (Koulischer et al., 2025). In later sections, we demonstrate our proposed nonlinear CFG generalizes to these methods, consistently enhancing their performance.

Dynamical regimes, statistical physics and high-dimensional settings. Statistical physics methods have shown particularly useful in analyzing high-dimensional generative models, *e.g.*, data from Curie-Weiss models (Biroli & Mézard, 2023), high-dimensional Gaussian mixtures (Biroli et al., 2024), and hierarchical models (Sclocchi et al., 2024). Furthermore, several recent works studied dynamical regimes diffusion models (Biroli & Mézard, 2023; Raya & Ambrogioni, 2024; Biroli

162 et al., 2024; Sclocchi et al., 2024; Yu & Huang, 2024; Li & Chen, 2024; Aranguri et al., 2025),
 163 however none of them analyzed the effects brought by classifier-free guidance.
 164

165 3 BACKGROUND AND HIGH-LEVEL DISCUSSION

167 We begin by providing an overview of the standard framework for generative diffusion, serving as
 168 the foundation for our analysis. Our exposition focuses on diffusion, though our findings directly
 169 extend to flow-matching with Gaussian paths (see, e.g., Lipman et al. (2024), Sec. 4.10.2).
 170

171 3.1 GENERAL SETUP

173 Let $\{\vec{a}_i\}_{i=1}^n \in \mathbb{R}^d$ represent n independent data points sampled from the *true* underlying data dis-
 174 tribution $P_0(\vec{a})$. The forward diffusion process, starting from data points $\{\vec{a}_i\}_{i=1}^n$, is modeled by an
 175 Ornstein-Uhlenbeck process, described by the following stochastic differential equation (SDE):

$$176 \quad d\vec{x}(t) = -\vec{x}(t) dt + \sqrt{2} d\vec{B}(t), \quad (1)$$

178 where $d\vec{B}(t)$ denotes the standard Brownian motion in \mathbb{R}^d . At any given time t , the state $\vec{x}(t)$ is
 179 distributed according to a Gaussian with mean $\vec{a}e^{-t}$ and variance $\Delta_t = 1 - e^{-2t}$. The forward
 180 process is terminated at time $t_f \gg 1$, when $\vec{x}(t_f)$ is effectively pure Gaussian noise, distributed as
 181 $\mathcal{N}(0, \mathcal{I}_d)$, with \mathcal{I}_d being the identity matrix in \mathbb{R}^d .

182 The backward diffusion process operates in reverse time $\tau = t_f - t$, described with:

$$184 \quad d\vec{x}(\tau) = \vec{x}(\tau) d\tau + 2\vec{S}(\vec{x}, \tau) d\tau + \sqrt{2} d\vec{B}(\tau), \quad (2)$$

185 where $\vec{S}(\vec{x}, t) = \vec{\nabla} \log P_t(\vec{x})$ denotes the score function. The backward diffusion process generates
 186 points \vec{x} sampled from the distribution $P_t(\vec{x})$ for every time step τ . At the end of the backward
 187 process, *i.e.*, when $\tau = t_f$, the process generates points drawn from the original distribution P_0 .
 188

189 In this work, we focus on generating data that can be categorized into distinct classes. We begin by
 190 assuming that the underlying data distribution is a d -dimensional probability distribution $P_0(\vec{x}, c)$,
 191 where c represents a discrete class index and \vec{x} a d -dimensional vector. The aim is to generate
 192 data conditioned on c , the class label. The procedure that is mathematically guaranteed to generate
 193 the exact conditional target distribution consists of using the true conditional score, $\vec{S}_t(\vec{x}, c) =$
 194 $\vec{\nabla} \log P_t(\vec{x}|c)$ in Eq. (2). CFG, however, does not do that; it instead further directs diffusion in a
 195 manner proportional to the difference between conditional and unconditional scores:

$$196 \quad S_t^{\text{CFG}}(\vec{x}, c) = S_t(\vec{x}, c) + \Delta S_t^{\text{CFG}}, \quad \Delta S_t^{\text{CFG}} := \omega(S_t(\vec{x}, c) - S_t(\vec{x})). \quad (3)$$

197 While CFG has shown practical benefits, such as improved fidelity and classification confidence
 198 (Wu et al., 2024), several key questions remain open: (1) Can one establish a theoretical frame-
 199 work proving that CFG can indeed generate the target distribution? (2) If so, can this framework
 200 also account for the well-documented artifacts of mean overshoot and variance shrinkage? (3) If
 201 these artifacts are indeed inherent to standard CFG, can one design alternative guidance schemes
 202 that provably mitigate them—and, crucially, do such schemes also deliver practical improvements
 203 beyond the theoretical setting? In this paper, we draw on the statistical-physics framework of Biroli
 204 & Mézard (2023); Biroli et al. (2024) to provide affirmative answers to all of the above.

206 3.2 CONNECTING DYNAMICAL REGIMES OF DIFFUSION TO CLASSIFIER-FREE GUIDANCE

207 To analyze CFG, we build on the statistical-physics framework of Biroli & Mézard (2023); Biroli
 208 et al. (2024), which identifies three dynamical regimes in diffusion models. Our exposition focuses
 209 on the first two, since we show that CFG has the same effect in the second and third regime. These
 210 regimes are distinguished by the presence or absence of symmetry breaking, characterized via the
 211 leading eigenvalue of the data covariance matrix.

212 **Previous findings: dynamical regimes in diffusion.** Using this framework, Biroli et al. (2024)
 213 analyze the dynamical regimes of the backward process in Eq. (2) for two classes in the $d \rightarrow \infty$
 214 limit. They identify the *speciation time* t_s as the transition between Regime I and Regime II.
 215 In Regime I, the backward trajectories have not yet committed to a particular data class, while

in Regime II, they have committed and begin generating the class-specific features necessary to produce samples. The core structure of these regimes persists (in the infinite-dimensional limit) well beyond Gaussian mixtures, extending to models such as data lying on manifolds (Ventura et al., 2024; Bae et al., 2024; George et al., 2025).

Our findings: connecting dynamical regimes to CFG. A central insight of our work is that the dynamical-regime framework provides a principled perspective for understanding CFG, from which three main results emerge:

Result I. *In sufficiently large and infinite dimensions, CFG generates the correct target distribution.* Specifically: (i) Before speciation time t_s , CFG accelerates convergence toward the target class. (ii) Just before t_s , CFG-guided paths realign with the unguided trajectory that produces the correct distribution. (iii) After t_s , CFG has no effect on the generation process.

Result II. *In finite dimensions, mean overshoot and variance shrinkage arise.* Using Gaussian mixtures, we characterize how the overshoot amplitude increases as dimensionality decreases and how CFG modifies the dynamics' potential, resulting in reduced variance of the generated distribution.

Result III. *There exist many simple guidances that effectively mitigate these effects.* Specifically, we introduce a simple nonlinear extension of CFG that reduces overshoot and variance shrinkage by multiplying the score difference ΔS_t^{CFG} in (3) with $|\Delta S_t^{\text{CFG}}|^\alpha$, $\alpha > 0$. This modification is theoretically justified and effective in simulations on Gaussian mixtures. As shown in Sec. 5, it is also beneficial in real-world applications.

While this framework provides valuable insights, it has a key limitation: it relies on access to the exact score. As a result, although it explains how to mitigate overshoot and variance shrinkage and supports nonlinear guidance schemes that improve practical performance, it does not clarify why standard CFG—despite these artifacts—often achieves strong empirical results. Addressing this question is beyond the scope of our current work, as it would require tools or analyses not available within our framework. Nonetheless, our theoretical analysis and nonlinear guidance show how to control these effects, providing meaningful theoretical insights and practical improvements.

4 MAIN RESULTS

The framework of Biroli & Mézard (2023); Biroli et al. (2024) characterizes dynamical regimes using a simple two-GMM. Its strength lies in broad applicability: such regimes appear across diverse generative models and data modalities (Ventura et al., 2024; George et al., 2025; Bae et al., 2024), and the framework has been validated on both real data and manifold-supported distributions (Biroli & Mézard, 2023). We provide its generalizations to non-centered/multi-component mixtures (Appx. C.1, C.2), heterogeneous variances, and high-dimensional manifold-structured data (Appx. C.3).

We focus here on the simplest case—two Gaussians of equal weight and isotropic variance—which already captures the essential phenomena and serves as the foundation for our theoretical framework.

THEORETICAL FRAMEWORK

We examine the case where $P_0(\vec{a})$ is a superposition of two Gaussians with equal weight, means $\pm \vec{m}$ and isotropic variance σ^2 . To ensure the two Gaussians are well separated, we take the large d limit with fixed values of $|\vec{m}|^2/d$ and σ^1 . As mentioned above, we assume exact scores are available.

In this setting, the speciation transition between Reg. I and II occurs on timescales $t_s = \frac{1}{2} \log(d)$. Biroli et al. (2024) showed that t_s corresponds to the time at which diffusion paths commit to a specific class, as determined by changes in the potential of the backward Langevin equation (see Fig. 3, Appx. A). This speciation time plays a central role in our first contribution: before t_s , CFG guides trajectories toward the target, accelerating convergence, while just prior to t_s , guided and unguided paths become aligned. After t_s , trajectories naturally follow unguided paths, ensuring that CFG produces the correct target distribution in infinite and sufficiently high dimensions.

¹The choice $|m| = \sqrt{d}$ is standard for modeling data with well-defined classes and has been adopted in several previous works (Li & Chen, 2024; Wu et al., 2024; Shah et al., 2023; Biroli et al., 2024).

Building on this foundation, our analysis also reveals two additional phenomena: (i) how finite-dimensional corrections give rise to mean overshoot and variance shrinkage, which we characterize exactly, and (ii) how a nonlinear extension of CFG can mitigate these effects.

In practice, our framework generalizes effectively to text-to-image models where one can view T2I learning as learning a mixture of zero-variance Gaussians corresponding to unique prompt-image pairs. In the presence of noise or non-unique mappings, this representation evolves into a standard Mixture of Gaussians (MoG). Given that MoGs are universal approximators, this formulation offers a strong theoretical basis for not only class-conditional, but also text-to-image training, which we later show by evaluating on various state-of-the-art models.

In the following, we present the theoretical arguments underlying these three results in a concise, conceptual manner, with the full derivations and proofs deferred to Appx. B through Appx. E.

4.1 KEY FINDING I: CFG GENERATES THE CORRECT DISTRIBUTION IN INFINITE AND LARGE DIMENSIONS

To establish our first result, we analyze the distribution of \vec{x} at time t , which can be written as

$$P_t(\vec{x}) \propto \exp \left[-\frac{(\vec{x} - \vec{m}e^{-t})^2}{2\Gamma_t} \right] + \exp \left[-\frac{(\vec{x} + \vec{m}e^{-t})^2}{2\Gamma_t} \right],$$

with $\Gamma_t = 1 + (\sigma^2 - 1)e^{-2t}$. In this setting, the CFG score (Eq. (3)) simplifies to

$$S_t^{\text{CFG}}(\vec{x}, c) = -\frac{\vec{x}}{\Gamma_t} + \frac{c\vec{m}e^t}{\Gamma_t} + \omega \frac{\vec{m}e^{-t}}{\Gamma_t} \left\{ c - \tanh \left(\frac{\vec{x} \cdot \vec{m}e^{-t}}{\Gamma_t} \right) \right\}, \quad (4)$$

with $c = \pm 1$ and $\omega > 0$. Our analysis develops the first result through three successive steps, all linked to the speciation time $t_s = \frac{1}{2} \log d$, the point at which trajectories commit to a specific class.

Step I: CFG guides trajectories before speciation. As we show in Appx. B.1, before t_s , CFG provides an extra push toward the target class, accelerating convergence. Importantly, as seen in the CFG score formula (4), CFG only affects the \vec{m} directions; all directions orthogonal to \vec{m} remain unaffected. Formally, projecting the backward dynamics onto a vector $\vec{v} \perp \vec{m}$ shows that the resulting dynamics are independent of ω , confirming only the \vec{m} direction is influenced.

Therefore, we project onto \vec{m} and define $q(t) = \vec{x} \cdot \vec{m} / |\vec{m}|$ with $|\vec{m}| = \sqrt{d}$. Then the backward evolution guided toward class $c = 1$ satisfies

$$dq = \left(q + 2 \left[-q + e^{-(t_f - t_s - \tau)} ((1 + \omega) - \omega \tanh(qe^{-(t_f - t_s - \tau)})) \right] \right) d\tau + d\eta(\tau), \quad (5)$$

where $\tau = t_f - t$ and $d\eta(\tau)$ denotes $\sqrt{2}$ times Brownian motion (specific theoretical arguments provided in Appx. B). This can be rewritten in terms of an effective potential $V^{\text{CFG}}(q, \tau)$:

$$V^{\text{CFG}} = \underbrace{\frac{1}{2}q^2 - 2e^{-(t-t_s)}q}_{\text{Conditional potential}} + \underbrace{\omega \left[-qe^{-(t-t_s)} + \ln \cosh(qe^{-(t-t_s)}) \right]}_{\text{CFG-induced potential}}. \quad (6)$$

Examining the effective potential in (6), we observe that the CFG-induced term provides an additional push along the \vec{m} direction toward the target class $c = 1$. This effect is especially significant for trajectories that deviate from typical paths, correcting those that would otherwise move toward the wrong class (see Fig. 7 in Section B). These observations allow us to conclude that, prior to the speciation t_s , CFG amplifies the push toward the desired class, establishing Step I.

Step II: CFG paths align before exiting Regime I. At late times in Regime I, q becomes of order \sqrt{d} (Biroli & Mézard, 2023), and the CFG-added term in Eq. (4) produces only exponentially small corrections to the dynamics. Although different values of ω may have led to different positions for q earlier in the backward process, these differences are quickly forgotten. The full theoretical argument is spelled out in Sec. B.2, i.e., we provide the proof of the dynamics naturally readjusting, and the trajectories converging toward the same distribution they would follow without CFG.

Step II is therefore obtained by analyzing the corresponding SDE starting from this late stage of Regime I: we show its solution no longer depends on the earlier CFG-induced deviations and coincides statistically with the backward evolution of a single Gaussian corresponding to the target class $c = +1$, implying the path alignment (see Fig. 8 in Section B for numerical simulations).

Step III: After speciation time t_s , CFG paths follow the unguided path. At the end of Regime I, as we show in Sec. B.3, the projection q diverges, and one has to analyze the rescaled variable $\vec{x} \cdot \vec{m}/d$. By this stage, the CFG-guided paths have realigned with the unguided conditional paths.

Specifically, we use results from Biroli et al. (2024) to show that in Regime II the extra CFG term in Eq. (4) effectively vanishes, since $1 - \tanh(\vec{x} \cdot \vec{m}e^{-t}/\Gamma_t) \rightarrow 0$ as $d \rightarrow \infty$. As a result, the dynamics as well as the trajectories follow the unguided backward evolution, yielding Step III.

Consistent conclusions in large, finite d . Within Regime I, for large, yet finite dimension, the CFG-added-term in the score in Eq. (4) remains of the same order as the conditional score of the unguided path so CFG has the same effect as in the infinite limit. The full proof is provided in Appx. D; when exiting Regime I and during Regime II, the extra CFG term is exponentially small in d , so the results from all three steps carry over for large but finite d (we discuss below the strength of the corrections for finite d).

In summary, during Regime I, CFG accelerates convergence toward the target class. Just before speciation, the paths realign with the unguided trajectory, subsequently following them throughout Regime II. This behavior is illustrated in Section B, Fig. 8. This result shows that, contrary to previous beliefs (Chidambaram et al., 2024; Wu et al., 2024), CFG can indeed generate the correct distribution, and serves as key guiding principle for the remainder of our work.

4.2 KEY FINDING II: CFG EFFECTS IN FINITE DIMENSIONAL SETTINGS

So far, we have shown that for any value of ω the target distribution is correctly reproduced in the infinite dimensional limit. We now show that the mean overshoot and variance shrinkage arise as the dimensionality of the system decreases. Full arguments can be found in Appx. D.

Mean overshoot and variance shrinkage in finite d . In finite dimensions, the paths do not realign when exiting Regime I. The additional push introduced by CFG within Regime I has an effect on Regime II, resulting in an overshoot of the target distribution of relative amplitude of order $1/\sqrt{d}$. The CFG-added-term also results in a larger second derivative of the potential $V^{\text{CFG}}(q, t)$. Thus, the CFG Langevin equation is associated to a more confining potential, ultimately shrinking the variance of the CFG-generated distribution. These are in line with previous empirical (Ho & Salimans, 2022) and theoretical findings (Chidambaram et al., 2024; Wu et al., 2024). In Appendix Figs. 8 and 12, we further analyze how CFG behavior changes with increasing dimensionality and number of classes both for numerical simulations and real-world scenarios. This concludes our second finding.

4.3 KEY FINDING III: NONLINEAR POWER-LAW CFG MITIGATES FINITE-DIM. EFFECTS

Building on the finite-dim. deviations identified in Key Finding II, we propose Power-Law CFG: a simple nonlinear extension of standard CFG. Our scheme raises the cond. score difference (3) along \vec{m} to a power $\alpha > 0$, allowing guidance to scale with the local strength of the conditional signal:

$$\vec{S}_t^{\text{PL}}(\vec{x}, c) = \vec{S}_t(\vec{x}, c) + \omega \left[\vec{S}_t(\vec{x}, c) - \vec{S}_t(\vec{x}) \right] \left| \vec{S}_t(\vec{x}, c) - \vec{S}_t(\vec{x}) \right|^\alpha. \quad (7)$$

Intuitively, this modification has two complementary effects: (i) When the score difference $\delta S_t = |\vec{S}_t(\vec{x}, c) - \vec{S}_t(\vec{x})|$ (vector norm) is small and potentially unreliable, guidance is naturally dampened. (ii) When the signal is strong, guidance is amplified, enhancing the push toward the correct class.

Importantly, as a direct consequence of our large- d theoretical analysis, nonlinear power-law CFG retains the exact high-dim. guarantees of standard CFG: in the limit of large dimension, it recovers the correct conditional distribution without distortion, ensuring that the benefits of nonlinear scaling are confined to the finite-dimensional regime. This is discussed in Appx. H.

378 **Reduced overshoot and shrinkage.** Our analysis in App. E identifies the key term $B(q) :=$
 379 $de^{-(t_f-t)}/\Gamma u(q)$ as the driver for mean overshoot and variance shrinkage. This term is intrinsically
 380 linked to the Hessian (curvature) of the potential, and the effect of nonlinear guidance is shown
 381 to directly modify $B(q)$, with $0 < B(q) < 1$ almost everywhere. **Mean Overshoot:** Overshoot
 382 is proportional to $B(q)$ and the parameter α controls this through $B(q)^\alpha$: $\alpha > 0$ suppresses the
 383 overshoot, while $\alpha < 0$ increases it. **Variance Shrinkage** is positively correlated with $B(q)$; $B(q)$
 384 determines the ratio of curvature increments between nonlinear and linear CFG through $B(q)^\alpha$.
 385 Specifically, $\alpha > 0$ reduces the curvature increase (decreasing shrinkage), while $\alpha < 0$ amplifies it
 386 (increasing shrinkage). Simulations (see, e.g., Fig. 2 (right) or Fig. 35) confirm this.

387 **Application to flow matching.** The power-law formula can be directly applied to flow-matching
 388 as well; in order to be fully consistent with our theoretical proposition, we expressed the Power-Law
 389 formula as $\phi_t(s) = (\frac{1-t}{t})^\alpha s^\alpha$, rather than $\phi_t(s) = s^\alpha$. However, even using $\phi_t(s) = s^\alpha$ (which is a
 390 valid guidance within our framework) yields very similar results and behavior - this is described in
 391 detail in appendix G.2.1.

392
 393 **Magnitude vs. Directional Scaling.** Our Power-Law formulation uses the Euclidean norm
 394 $\|S_t(\vec{x}, c) - S_t(\vec{x})\|$ which captures both score *direction* and *magnitude*, unlike, e.g., cosine met-
 395 rics that would isolate alignment. While the Euclidean norm is resolution-sensitive, luckily, the
 396 guidance parameter ω acts as a renormalization factor, which ultimately removes the need for an
 397 additional explicit resolution-based adjustments. As detailed in App. G.7, our analyses showed that
 398 this combined signal yields superior performance compared to purely directional metrics, though
 399 alternative cosine-based methods remain a promising avenue for future work.

401 4.4 DISCUSSION: OTHER NONLINEAR EXTENSIONS

402 Beyond the power-law modification, our analysis indicates a broad class of theoretically valid, po-
 403 tentially beneficial nonlinear guidances. Our framework and the “blessing of dimensionality”, en-
 404 suring CFG recovers the correct target distribution in high dimensions, are not limited to the specific
 405 construction above: many nonlinear extensions share the same guarantees.

406 Formally, our results can be extended to nonlinear guidances of the form

$$407 S_t^{\text{CFG-NL}}(\vec{x}, c) = S_t(\vec{x}, c) + [S_t(\vec{x}, c) - S_t(\vec{x})] \phi_t \left(\left| \vec{S}_t(\vec{x}, c) - \vec{S}_t(\vec{x}) \right| \right), \quad (8)$$

408 under the condition $\lim_{s \rightarrow 0} s\phi_t(s) = 0$, ensuring guidance vanishes smoothly when cond. and
 409 uncond. scores coincide. This condition essentially relies on the part of our proof showing that
 410 scores equalize at low noise levels (as often observed in practice), preventing pathological guid-
 411 ances that break this property). This framework recovers a number of existing methods as special
 412 cases: constant $\phi_t(s) = \omega$ yields standard CFG; $\phi_t(s) = \omega \cdot \mathbb{I}_{[t_1, t_2]}(t)$ gives limited-interval CFG
 413 (Kynkänniemi et al., 2024); and time-varying $\phi_t(s) = \omega_t$ recovers weight schedulers (Wang et al.,
 414 2024; Gao et al., 2023). Other recent proposals (Chung et al., 2024; Xia et al., 2024; Ventura et al.,
 415 2024) can also be expressed as specific, simple choices of ϕ_t . Importantly, all of these remain linear
 416 in the score difference δS_t , whereas our nonlinear power-law scheme \vec{S}_t^{PL} demonstrates that altering
 417 the score difference in a nonlinear manner is both theoretically natural and practically beneficial.

418 This perspective opens a larger design space of alternative nonlinear functions ϕ_t , which could as
 419 well be directly optimized, yielding theoretically sound guidance mechanisms, potentially outper-
 420 forming existing approaches. Building on this, we next evaluate the nonlinear power-law guidance in
 421 both controlled GMM settings and large-scale generative models, validating theoretical predictions,
 422 assessing robustness, and comparing directly to linear CFG and alternative CFG schemes.

423 5 NUMERICAL SIMULATIONS AND REAL-WORLD EXPERIMENTS

424 We now turn to experiments, testing nonlinear CFG derived from our large- d theoretical guidelines.
 425 Through num. simulations and real-world experiments, we evaluate if the theoretically motivated
 426 power-law CFG delivers tangible benefits, e.g., in mitigating overshoot and preserving variance.

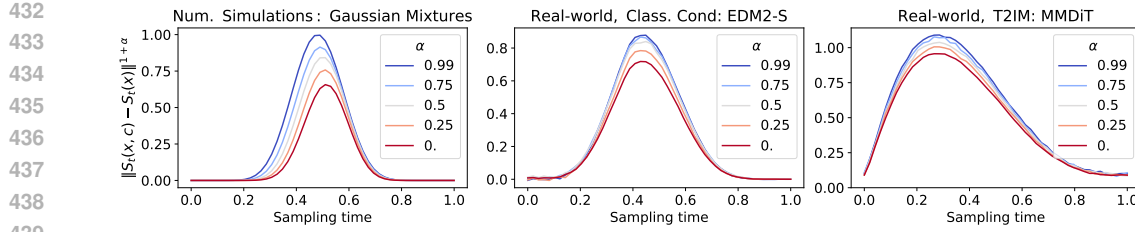


Figure 4: **The flexibility of nonlinear power-law CFG, key ingredient in our theoretical argument, appears consistently in num. simulations and real-world models.** Left: Num. simulations on GMMs. Center: Real-world, Class. Cond: EDM2-S. Right: Real-world, T2IM: MMDiT. All exhibit the same hump-shaped behavior of $\|S_t(\vec{x}, c) - S_t(\vec{x})\|^{1+\alpha}$, consistent with our theoretical analysis.

Experimental details. We examine power-law CFG in GMM simulations and four generative models: DiT (Peebles & Xie, 2023) and EDM2 (Karras et al., 2024b), trained and evaluated on ImageNet-1K (res. 256 and 512). We also consider two text-to-image (T2IM) models: first is trained on ImageNet-1k and CC12M (Changpinyo et al., 2021), evaluated on CC12M, using the diffusion DDPM training objective (Ho et al., 2020) with MMDiT architecture (Esser et al. (2024), similar to SD3). The second model, using MMDiT scaled to 1.6B parameters, is trained with flow matching on YFCC100M (Thomee et al., 2016), CC12M and a proprietary dataset of 320M Shutterstock images, evaluated on COCO dataset (Lin et al., 2014). Section G contains another T2IM model trained with DDPM objective with the MDTv2 (Gao et al., 2023) architecture scaled to 800M parameters.

Comparing GMM simulations to real-world experiments. Fig. 4 shows both GMM simulations and large-scale gen. models exhibit the same characteristic hump-shaped behavior of the amplitude of the guidance term $\|S_t(\vec{x}, c) - S_t(\vec{x})\|^{1+\alpha}$, suggesting our theoretical insights might be beneficial in practice. Crucially, the power-law param. α allows to alter the shape of these curves, offering the precise flexibility our analysis identifies as necessary for improving guidance. We further examine this in Fig. 35 in Appx. H, showing nonlin. CFG results in faster convergence, with paths of smaller Jensen-Shannon divergence to the target (across all time τ), while also reducing the overshoot.

Power-law CFG is robust. We perform sensitivity analysis, showing that large values of α consistently yield improved performance, increasing robustness and stability when tuning for ω .² This is shown in Fig. 5 for EDM2-S, in Section G for DiT/XL-2, two T2IM models, together with further ablation studies showing that non-lin. CFG consistently outperforms standard CFG when varying number of sampling steps.

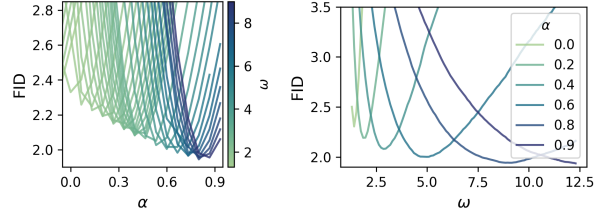


Figure 5: **Sensitivity analysis** (EDM2-S, ImageNet-1K 512 \times 512). Left: Increasing parameter α consistently improves FID to standard CFG ($\alpha = 0$). Right: Increasing α yields more stable FID values across a larger range of ω .

Power-law CFG improves image quality and diversity. We quantitatively evaluate our method using FID (Heusel et al., 2017) measuring image quality, and precision and recall (Sajjadi et al., 2018) measuring diversity. In Table 1, we compare power-law CFG to state-of-the-art guidance methods. As power-law is easily combined with other guidances, we test combining it with CADS (Sadat et al., 2023) and limited-guidance (Kynkänniemi et al., 2024), the strongest competitors. Power-law CFG improves over standard CFG in most cases and improves results of CADS and lim.-interval guidance. We provide qualitative results in Fig. 6, observing that power-law improves both quality and diversity, while being more robust to changing ω .

Latent-space vs Pixel-space. The power-law method consistently showed robust improvements with the nonlinear parameter $\alpha = 0.9$ set across all experiments in latent space. For pixel space (see Table 11 in Appx.), the optimal α seemed to fluctuate slightly more and tuning α as well as

²Although power-law CFG introduces another hyperparameter, α , we did not have to perform extensive hyperparameter search, and found large values, e.g., $\alpha = 0.9$ to consistently perform well.

486

Table 1: **Power-law CFG often improves both fidelity and diversity metrics.** We applied power-law to standard CFG, limited and CADS variants, as the two were strongest competitors. Applying power-law improved their performance further, achieving competitive results. Best results are **bolded**, second best underlined. (\uparrow) indicates power-law CFG improves the guidance method compared to its version with stand. CFG, while (\downarrow) means the metric deteriorated. T2IM represents text-to-image models, CC class-conditional; FM is short for flow-matching objective and diff. stands diffusion. Experimental details are provided in Section G.

Model	EDM2-S (CC, IM-1K 512)			DiT/XL-2 (CC, IM-1K 256)			Diff. MMDIT (T2IM, CC12m)			FM MMDIT (T2IM, COCO)		
	FID	Precision	Recall	FID	Precision	Recall	FID	Precision	Recall	FID	Precision	Recall
Standard (Ho & Salimans, 2022)	2.29	0.751	0.582	2.27	0.829	0.584	8.58	0.661	0.569	5.20	0.629	0.594
Scheduler (Wang et al., 2024)	2.03	0.762	0.591	2.14	0.840	0.614	8.30	0.681	0.559	5.00	0.606	0.623
Limited (Kynkänniemi et al., 2024)	1.87	0.760	0.598	1.97	0.801	0.632	8.58	0.680	0.553	5.00	0.609	0.602
Cosine (Gao et al., 2023)	2.15	0.770	0.619	2.30	0.861	0.520	8.29	0.659	0.564	5.14	0.630	0.616
CADS (Sadat et al., 2023)	1.60	0.792	0.619	1.70	0.772	0.627	8.32	0.692	0.559	4.91	0.633	0.613
APG (Sadat et al., 2024)	2.13	0.756	0.640	2.11	0.815	0.628	8.49	0.661	<u>0.571</u>	5.23	0.614	0.631
REG (Xia et al., 2024)	1.99	0.761	0.608	1.76	0.799	0.601	<u>8.10</u>	0.673	0.540	5.06	0.619	0.619
CFG++ (Chung et al., 2024)	N/A	N/A	N/A	N/A	N/A	N/A	8.35	0.668	0.552	4.85	0.632	0.629
Power-law CFG (Ours)	1.93 (\uparrow)	0.780 (\uparrow)	0.631 (\uparrow)	2.05 (\downarrow)	0.831 (\uparrow)	0.595 (\uparrow)	8.11 (\downarrow)	0.670 (\uparrow)	0.553 (\downarrow)	4.81 (\downarrow)	0.621 (\downarrow)	0.619 (\uparrow)
Power-law CFG + Limited (Ours)	1.73 (\downarrow)	0.752 (\downarrow)	0.600 (\downarrow)	1.87 (\downarrow)	0.849 (\uparrow)	0.642 (\uparrow)	8.27 (\downarrow)	0.692 (\uparrow)	0.555 (\downarrow)	4.84 (\downarrow)	0.615 (\downarrow)	0.622 (\uparrow)
Power-law CFG + CADS (Ours)	1.52 (\uparrow)	0.770 (\downarrow)	0.622 (\uparrow)	<u>1.63</u> (\downarrow)	0.754 (\downarrow)	0.639 (\downarrow)	7.98 (\downarrow)	0.690 (\downarrow)	<u>0.573</u> (\downarrow)	4.71 (\downarrow)	0.640 (\uparrow)	0.624 (\downarrow)

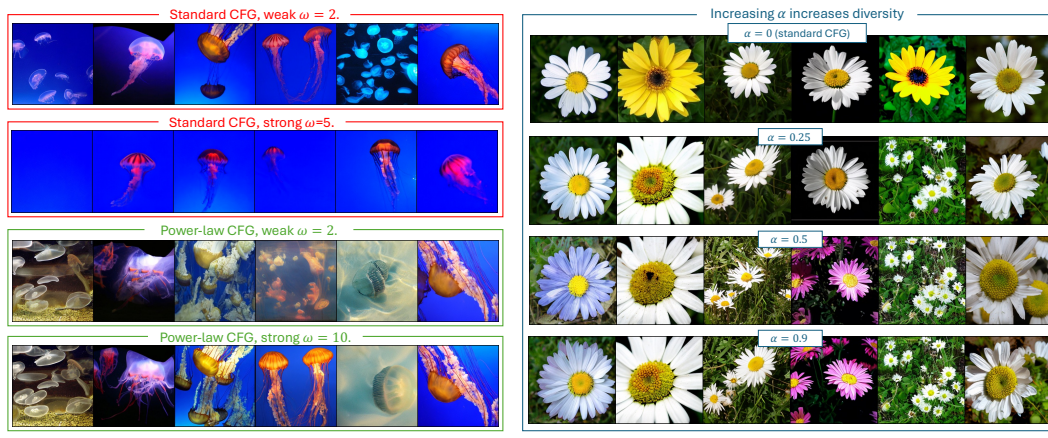


Figure 6: **Qualitative comparison of Standard and Power-Law CFG on DiT/XL-2 trained on ImageNet-1k (256 \times 256).** **Left:** while standard CFG results in diversity decrease or mode collapse (first image for $\omega = 5$), power-law CFG ($\alpha = 0.9$) improves in diversity at no cost to fidelity, showing robustness to varying of ω (note very large $\omega = 10$). **Right:** Increasing non-linear parameter α yields larger diversity, while preserving image quality. Experimental details with further examples (as well as text-to-image) are provided in App. G.

ω resulted in stronger improvement in performance. While Power-Law demonstrates consistent benefits, its performance relative to other non-linear strategies remains unexplored. There may be more strategies (particularly for pixel-space), which are worth exploring.

6 CONCLUSION

By connecting CFG to the high-dimensional framework of diffusion regimes, we theoretically analyzed its behavior and showed that, in sufficiently high dimensions, CFG reproduces the correct target distribution—a “blessing-of-dimensionality” result. We further demonstrated that the well-known artifacts of mean overshoot and variance shrinkage emerge as dimensionality decreases. Finally, we proposed a simple nonlinear extension of CFG, proving that it mitigates both effects while preserving CFG’s practical benefits, consistently improving sample quality and diversity across state-of-the-art text-to-image and class-conditional models.

Limitations and future work. Our theory demonstrates that in high-dimensional settings, CFG generates the correct target distribution, extending previous results showing CFG alters it in finite-dimensions. In practice, CFG improves fidelity while reducing diversity: although our theory allows discovery of guidances that maintain strong fidelity while significantly boosting diversity, the reason why CFG-modified distribution is more effective in practice is not explained by our theory which relies on perfect score estimation. We hypothesize, therefore, that the practical benefits of (non-linear) CFG might be tied to the imperfect score estimators used in practice. Investigating how score approximation errors impact guidance effectiveness is an important area for future research.

540
541 ETHICS STATEMENT542 This study contributes to the growing body of research aimed at deepening our theoretical under-
543 standing of diffusion models and their broader implications for generative modeling. By bridging
544 the gap between theory and practice, we strive to improve the performance and efficiency of these
545 models, which have far-reaching applications in various fields.546 However, as with any powerful technology, there are also potential risks associated with develop-
547 ment and deployment of advanced generative models. The increasing sophistication of deepfakes
548 raises concerns about misinformation, propaganda, and the erosion of trust in digital media. More-
549 over, the misuse of generative models for malicious purposes, such as creating fake identities or
550 spreading disinformation, poses significant threats to society as a whole.551 In light of these challenges, we hope that our paper, along with many others that aim to improve
552 understanding of the models, will contribute to a deeper understanding of their strengths and limi-
553 tations. We believe it is essential for developing effective strategies to mitigate the risks associated
554 with generative models, and we hope that our work will be a step toward achieving this goal.555
556 REPRODUCIBILITY STATEMENT557 We have clearly stated the main assumptions underlying our work, along with their limitations and
558 how they influence our conclusions. To support our theoretical contributions, Appendices B-E con-
559 tain the full proofs of our claims, while Appendix G.3 lists all hyperparameter configurations re-
560 quired to reproduce our experiments exactly. For real-world experiments, we specify the GPUs used
561 as well as the Gflops of the models, offering transparency in the computational resources required.
562 Finally, our experiments on class-conditional models rely on and reference publicly available check-
563 points, enabling straightforward verification and further exploration by the community.564
565
566
567
568
569
570
571
572
573
574
575
576
577
578
579
580
581
582
583
584
585
586
587
588
589
590
591
592
593

594 REFERENCES
595

596 Beatrice Achilli, Luca Ambrogioni, Carlo Lucibello, Marc Mézard, and Enrico Ventura. Memo-
597 rization and generalization in generative diffusion under the manifold hypothesis. *arXiv preprint*,
598 2502.09578, 2025.

599 Michael S Albergo, Nicholas M Boffi, and Eric Vanden-Eijnden. Stochastic interpolants: A unifying
600 framework for flows and diffusions. *arXiv preprint*, 2303.08797, 2023.

601

602 Santiago Aranguri, Giulio Biroli, Marc Mezard, and Eric Vanden-Eijnden. Optimizing noise sched-
603 ules of generative models in high dimensions. *arXiv preprint*, 2501.00988, 2025.

604

605 Pietro Astolfi, Marlène Careil, Melissa Hall, Oscar Mañas, Matthew Muckley, Jakob Verbeek, Adri-
606 ana Romero Soriano, and Michal Drozdzal. Consistency-diversity-realism Pareto fronts of con-
607 ditional image generative models. *arXiv preprint*, 2406.10429, 2024.

608 Stefano Bae, Enzo Marinari, and Federico Ricci-Tersenghi. A very effective and simple diffusion
609 reconstruction for the diluted Ising model. *arXiv preprint*, 2407.07266, 2024.

610

611 Weimin Bai, Yifei Wang, Wenzheng Chen, and He Sun. An expectation-maximization algorithm for
612 training clean diffusion models from corrupted observations. *arXiv preprint*, 2407.01014, 2024.

613

614 Fan Bao, Chongxuan Li, Yue Cao, and Jun Zhu. All are worth words: a vit backbone for score-based
615 diffusion models. In *NeurIPS 2022 Workshop on Score-Based Methods*, 2022.

616

617 James Betker, Gabriel Goh, Li Jing, Tim Brooks, Jianfeng Wang, Linjie Li, Long Ouyang, Juntang
618 Zhuang, Joyce Lee, Yufei Guo, et al. Improving image generation with better captions. Technical
619 report, OpenAI, 2023. URL <https://cdn.openai.com/papers/dall-e-3.pdf>.

620

621 Giulio Biroli and Marc Mézard. Generative diffusion in very large dimensions. *Journal of Statistical
622 Mechanics: Theory and Experiment*, 2023(9):093402, 2023.

623

624 Giulio Biroli, Tony Bonnaire, Valentin De Bortoli, and Marc Mézard. Dynamical regimes of diffu-
625 sion models. *arXiv preprint*, 2402.18491, 2024.

626

627 Arwen Bradley and Preetum Nakkiran. Classifier-free guidance is a predictor-corrector. *arXiv
628 preprint*, 2408.09000, 2024.

629

630 Soravit Changpinyo, Piyush Sharma, Nan Ding, and Radu Soricut. Conceptual 12m: Pushing web-
631 scale image-text pre-training to recognize long-tail visual concepts. In *CVPR*, 2021.

632

633 Hansheng Chen, Kai Zhang, Hao Tan, Zexiang Xu, Fujun Luan, Leonidas Guibas, Gordon Wet-
634 ztein, and Sai Bi. Gaussian mixture flow matching models. *arXiv preprint*, 2504.05304, 2025a.

635

636 Shoufa Chen, Chongjian Ge, Shilong Zhang, Peize Sun, and Ping Luo. Pixelflow: Pixel-space
637 generative models with flow. *arXiv preprint arXiv:2504.07963*, 2025b.

638

639 Muthu Chidambaram, Khashayar Gatmiry, Sitan Chen, Holden Lee, and Jianfeng Lu. What does
640 guidance do? A fine-grained analysis in a simple setting. *arXiv preprint*, 2409.13074, 2024.

641

642 Hyungjin Chung, Jeongsol Kim, Geon Yeong Park, Hyelin Nam, and Jong Chul Ye. CFG++:
643 Manifold-constrained classifier free guidance for diffusion models. *arXiv preprint*, 2406.08070,
644 2024.

645

646 Hugo Cui, Florent Krzakala, Eric Vanden-Eijnden, and Lenka Zdeborová. Analysis of learning a
647 flow-based generative model from limited sample complexity. *arXiv preprint*, 2310.03575, 2023.

648

649 Jia Deng, Wei Dong, Richard Socher, Li-Jia Li, Kai Li, and Li Fei-Fei. Imagenet: A large-scale
650 hierarchical image database. In *CVPR*, 2009.

651

652 Prafulla Dhariwal and Alexander Nichol. Diffusion models beat GANs on image synthesis. In
653 *Advances in neural information processing systems*, 2021.

648 Yilun Du, Conor Durkan, Robin Strudel, Joshua B Tenenbaum, Sander Dieleman, Rob Fergus,
 649 Jascha Sohl-Dickstein, Arnaud Doucet, and Will Sussman Grathwohl. Reduce, reuse, recycle:
 650 Compositional generation with energy-based diffusion models and MCMC. In *International con-*
 651 *ference on machine learning*, 2023.

652 Patrick Esser, Sumith Kulal, Andreas Blattmann, Rahim Entezari, Jonas Müller, Harry Saini, Yam
 653 Levi, Dominik Lorenz, Axel Sauer, Frederic Boesel, et al. Scaling rectified flow transformers for
 654 high-resolution image synthesis. In *International conference on machine learning*, 2024.

655 Shanghua Gao, Pan Zhou, Ming-Ming Cheng, and Shuicheng Yan. Masked diffusion transformer is
 656 a strong image synthesizer. In *ICCV*, 2023.

657 Anand Jerry George, Rodrigo Veiga, and Nicolas Macris. Analysis of diffusion models for manifold
 658 data. *arXiv preprint*, 2502.04339, 2025.

659 Jiatao Gu, Shuangfei Zhai, Yizhe Zhang, Josh Susskind, and Navdeep Jaitly. Matryoshka diffusion
 660 models. *arXiv preprint arXiv:2310.15111*, 2023.

661 Melissa Hall, Oscar Mañas, Reyhane Askari, Mark Ibrahim, Candace Ross, Pietro Astolfi,
 662 Tariq Berrada Ifriqi, Marton Havasi, Yohann Benchetrit, Karen Ullrich, et al. EvalGIM: A li-
 663 brary for evaluating generative image models. *arXiv preprint*, 2412.10604, 2024.

664 Martin Heusel, Hubert Ramsauer, Thomas Unterthiner, Bernhard Nessler, and Sepp Hochreiter.
 665 Gans trained by a two time-scale update rule converge to a local Nash equilibrium. In *Advances*
 666 *in neural information processing systems*, 2017.

667 Jonathan Ho and Tim Salimans. Classifier-free diffusion guidance. *arXiv preprint*, 2207.12598,
 668 2022.

669 Jonathan Ho, Ajay Jain, and Pieter Abbeel. Denoising diffusion probabilistic models. In *Advances*
 670 *in neural information processing systems*, 2020. URL <https://arxiv.org/abs/2006.11239>.

671 Zahra Kadkhodaie, Stéphane Mallat, and Eero P Simoncelli. Feature-guided score diffusion for
 672 sampling conditional densities. *arXiv preprint*, 2410.11646, 2024.

673 Tero Karras, Miika Aittala, Timo Aila, and Samuli Laine. Elucidating the design space of diffusion-
 674 based generative models. In *Advances in neural information processing systems*, 2022.

675 Tero Karras, Miika Aittala, Tuomas Kynkänniemi, Jaakko Lehtinen, Timo Aila, and Samuli Laine.
 676 Guiding a diffusion model with a bad version of itself. *arXiv preprint*, 2406.02507, 2024a.

677 Tero Karras, Miika Aittala, Jaakko Lehtinen, Janne Hellsten, Timo Aila, and Samuli Laine. Analyz-
 678 ing and improving the training dynamics of diffusion models. In *CVPR*, 2024b.

679 Felix Koulischer, Florian Handke, Johannes Deleu, Thomas Demeester, and Luca Ambrogioni.
 680 Feedback guidance of diffusion models. *arXiv preprint*, 2506.06085, 2025.

681 Tuomas Kynkänniemi, Miika Aittala, Tero Karras, Samuli Laine, Timo Aila, and Jaakko Lehtinen.
 682 Applying guidance in a limited interval improves sample and distribution quality in diffusion
 683 models. *arXiv preprint*, 2404.07724, 2024.

684 Sangyun Lee, Beomsu Kim, and Jong Chul Ye. Minimizing trajectory curvature of ode-based gen-
 685 erative models. In *International conference on machine learning*, 2023.

686 Marvin Li and Sitan Chen. Critical windows: non-asymptotic theory for feature emergence in
 687 diffusion models. *arXiv preprint*, 2403.01633, 2024.

688 Yingyu Liang, Zhenmei Shi, Zhao Song, and Yufa Zhou. Unraveling the smoothness properties of
 689 diffusion models: A Gaussian mixture perspective. *arXiv preprint*, 2405.16418, 2024.

690 Tsung-Yi Lin, Michael Maire, Serge Belongie, James Hays, Pietro Perona, Deva Ramanan, Piotr
 691 Dollár, and C Lawrence Zitnick. Microsoft COCO: Common objects in context. In *ECCV*, 2014.

702 Yaron Lipman, Ricky TQ Chen, Heli Ben-Hamu, Maximilian Nickel, and Matt Le. Flow matching
 703 for generative modeling. *arXiv preprint*, 2210.02747, 2022.
 704

705 Yaron Lipman, Marton Havasi, Peter Holderrieth, Neta Shaul, Matt Le, Brian Karrer, Ricky TQ
 706 Chen, David Lopez-Paz, Heli Ben-Hamu, and Itai Gat. Flow matching guide and code. *arXiv*
 707 *preprint*, 2412.06264, 2024.

708 Xingchao Liu, Chengyue Gong, and Qiang Liu. Flow straight and fast: Learning to generate and
 709 transfer data with rectified flow. *arXiv preprint*, 2209.03003, 2022.
 710

711 Alex Nichol, Prafulla Dhariwal, Aditya Ramesh, Pranav Shyam, Pamela Mishkin, Bob McGrew,
 712 Ilya Sutskever, and Mark Chen. GLIDE: Towards photorealistic image generation and editing
 713 with text-guided diffusion models. In *International conference on machine learning*, 2022. URL
 714 <https://arxiv.org/abs/2112.10741>.

715 William Peebles and Saining Xie. Scalable diffusion models with transformers. In *ICCV*, 2023.
 716

717 Gabriel Raya and Luca Ambrogioni. Spontaneous symmetry breaking in generative diffusion mod-
 718 els. In *Advances in neural information processing systems*, 2024.

719 Seyedmorteza Sadat, Jakob Buhmann, Derek Bradley, Otmar Hilliges, and Romann M Weber.
 720 CADS: Unleashing the diversity of diffusion models through condition-annealed sampling. *arXiv*
 721 *preprint*, 2310.17347, 2023.

722 Seyedmorteza Sadat, Otmar Hilliges, and Romann M Weber. Eliminating oversaturation and ar-
 723 tifacts of high guidance scales in diffusion models. In *International Conference on Learning
 724 Representations (ICLR)*, 2024.

725 Chitwan Saharia, William Chan, Saurabh Saxena, Lala Li, Jay Whang, Emily Denton, Seyed Kam-
 726 yar Seyed Ghasemipour, Burcu Karagol Ayan, S. Sara Mahdavi, Rapha Gontijo Lopes, Tim Sal-
 727 imans, Jonathan Ho, David J Fleet, and Mohammad Norouzi. Photorealistic text-to-image dif-
 728 fusion models with deep language understanding. In *Advances in neural information processing
 729 systems*, 2022. URL <https://arxiv.org/abs/2205.11487>.

730

731 Mehdi SM Sajjadi, Olivier Bachem, Mario Lucic, Olivier Bousquet, and Sylvain Gelly. Assessing
 732 generative models via precision and recall. In *Advances in neural information processing systems*,
 733 2018.

734

735 Tim Salimans, Ian Goodfellow, Wojciech Zaremba, Vicki Cheung, Alec Radford, and Xi Chen.
 736 Improved techniques for training GANs. In *Advances in neural information processing systems*,
 737 2016.

738

739 Antonio Sclocchi, Alessandro Favero, and Matthieu Wyart. A phase transition in diffusion models
 740 reveals the hierarchical nature of data. *arXiv preprint*, 2402.16991, 2024.

741

742 Kulin Shah, Sitan Chen, and Adam Klivans. Learning mixtures of Gaussians using the DDPM
 743 objective. In *Advances in neural information processing systems*, 2023.

744

745 Jascha Sohl-Dickstein, Eric A. Weiss, Niru Maheswaranathan, and Surya Ganguli. Deep unsuper-
 746 vised learning using nonequilibrium thermodynamics. *arXiv preprint*, 1503.03585, 2015. URL
 747 <https://arxiv.org/abs/1503.03585>.

748

749 Yang Song and Stefano Ermon. Generative modeling by estimating gradients of the data distribution.
 750 *arXiv preprint*, 1907.05600, 2020. URL <https://arxiv.org/abs/1907.05600>.

751

752 Yang Song, Jascha Sohl-Dickstein, Diederik P Kingma, Abhishek Kumar, Stefano Ermon, and Ben
 753 Poole. Score-based generative modeling through stochastic differential equations. *arXiv preprint*,
 2011.13456, 2020.

754

755 Shikun Sun, Longhui Wei, Zhicai Wang, Zixuan Wang, Junliang Xing, Jia Jia, and Qi Tian. Inner
 classifier-free guidance and its Taylor expansion for diffusion models. In *International Confer-
 ence on Learning Representations (ICLR)*, 2023.

756 Bart Thomee, David A Shamma, Gerald Friedland, Benjamin Elizalde, Karl Ni, Douglas Poland,
 757 Damian Borth, and Li-Jia Li. YFCC100M: the new data in multimedia research. *Communications*
 758 *of the ACM*, 59(2):64–73, 2016.

759

760 Enrico Ventura, Beatrice Achilli, Gianluigi Silvestri, Carlo Lucibello, and Luca Ambrogioni. Man-
 761 ifolds, random matrices and spectral gaps: The geometric phases of generative diffusion. *arXiv*
 762 *preprint*, 2410.05898, 2024.

763

764 Qing Wang, Sanjeev R Kulkarni, and Sergio Verdú. Divergence estimation for multidimensional
 765 densities via k-nearest-neighbor distances. *IEEE Transactions on Information Theory*, 55(5):
 766 2392–2405, 2009.

767

768 Xi Wang, Nicolas Dufour, Nefeli Andreou, Marie-Paule Cani, Victoria Fernández Abrevaya, David
 769 Picard, and Vicky Kalogeiton. Analysis of classifier-free guidance weight schedulers. *arXiv*
 770 *preprint*, 2404.13040, 2024.

771

772 Yuchen Wu, Minshuo Chen, Zihao Li, Mengdi Wang, and Yuting Wei. Theoretical insights for
 773 diffusion guidance: A case study for Gaussian mixture models. *arXiv preprint*, 2403.01639,
 774 2024.

775

776 Mengfei Xia, Nan Xue, Yujun Shen, Ran Yi, Teliang Gong, and Yong-Jin Liu. Rectified diffusion
 777 guidance for conditional generation. *arXiv preprint*, 2410.18737, 2024.

778

779 Zhendong Yu and Haiping Huang. Nonequilibrium physics of generative diffusion models. *arXiv*
 780 *preprint*, 2405.11932, 2024.

781

782 Candi Zheng and Yuan Lan. Characteristic guidance: Non-linear correction for DDPM at large
 783 guidance scale. *arXiv preprint*, 2312.07586, 2023.

784

785 Jean Zinn-Justin. *Quantum field theory and critical phenomena*, volume 171. Oxford university
 786 press, 2021.

787

788

789

790

791

792

793

794

795

796

797

798

799

800

801

802

803

804

805

806

807

808

809

810
811
812
813
814
815
816
817
818
819
820
821
822
823
824
825
826
827
828
829
830
831
832
833
834
835
836
837
838
839
840
841
842
843
844
845
846
847
848
849
850
851
852
853
854
855
856
857
858
859
860
861
862
863
SUPPLEMENTARY MATERIAL

The supplementary material is structured as follows:

- In Section A, we give a brief introduction to related work, focusing on [Biroli et al. \(2024\)](#).
- In Section B, we give proofs for two equidistant, symmetric Gaussian mixtures.
- In Section C, we present arguments how to extend the proofs to non-centered Gaussian mixtures (subsec. C.1) and multiple Gaussian mixtures (subsec. C.2).
- In Section D, we present the theoretical and numerical findings for finite dimension (including low dimension d).
- In Section E, we provide the arguments showing that the nonlinear Power-Law CFG improves mean overshoot and variance shrinkage.
- In Section F, we present experimental details for Gaussian mixture numerical simulations.
- In Section G, we provide experimental details involving real-world experiments.
- In Section H, we propose another non-linear CFG alternative and provide num. experiments.

A INTRODUCTION TO RELATED WORK: CLASSIFIER-FREE GUIDANCE (CFG) AND SPECIFICATION TIME IN THE HIGH-DIMENSIONAL LIMIT

We start by briefly introducing the calculation required for estimating the speciation time t_s for a case of two equally weighted Gaussians. This section is a direct adaptation of the framework introduced by [Biroli et al. \(2024\)](#). The diffusion process, consisting of d independent Ornstein-Uhlenbeck Langevin equations, reads as follows (using $f(t) = -1$ and $g(t) = \sqrt{2}$ in Eq. (1)):

$$d\vec{x}(t) = -\vec{x}dt + d\vec{B}(t), \quad (9)$$

where $d\vec{B}(t)$ equals the square root of two times the standard Brownian motion in \mathbb{R}^d . At time $t = 0$, the process starts from the probability distribution $P_0(\vec{a})$, consisting of two Gaussian clusters that have means at $\pm\vec{m}$ and share the same variance σ^2 . To guarantee that these Gaussians remain distinct in high-dimensional space, we assume that $|\vec{m}|^2 = d\tilde{\mu}^2$, where both σ and $\tilde{\mu}$ are of order 1.

As the process evolves, the emergence of speciation resembles symmetry breaking observed during thermodynamic phase transitions. A common approach to analyzing this phenomenon is to construct a perturbative expansion of the free energy as a function of the field. Therefore, [Biroli et al. \(2024\)](#) derive an expression for $\log P_t(\vec{x})$ using a perturbative expansion in terms of e^{-t} , which is valid for large time values. This method is justified since speciation occurs at large times.

One can rewrite the probability to be at \vec{x} at time t as

$$\begin{aligned} P_t(\vec{x}) &= \int d\vec{a} P_0(\vec{a}) \frac{1}{\sqrt{2\pi\Delta_t^d}} \exp\left(-\frac{1}{2} \frac{(\vec{x} - \vec{a}e^{-t})^2}{\Delta_t}\right) \\ &= \frac{1}{\sqrt{2\pi\Delta_t}} \exp\left(-\frac{1}{2} \frac{\vec{x}^2}{\Delta_t} + g(\vec{x})\right), \end{aligned}$$

where the function $g(\vec{x})$, defined as

$$g(\vec{x}) = \log \int d\vec{a} P_0(\vec{a}) \exp\left(-\frac{1}{2} \frac{\vec{a}^2 e^{-2t}}{\Delta_t}\right) \exp\left(\frac{e^{-t} \vec{x} \cdot \vec{a}}{\Delta_t}\right)$$

can be viewed through a field-theoretic (or equivalently, a probabilistic) approach, where it serves as a generative function for connected correlations among the variables \vec{a} ([Zinn-Justin, 2021](#)). By

864 expanding this function at large times, one can show:
 865

$$866 \quad g(\vec{x}) = \frac{e^{-t}}{\Delta_t} \sum_{i=1}^d x_i \langle a_i \rangle + \frac{1}{2} \frac{e^{-2t}}{\Delta_t^2} \sum_{i,j=1}^d x_i x_j \left[\langle a_i a_j \rangle - \langle a_i \rangle \langle a_j \rangle \right] + O\left((xe^{-t})^3\right),$$

$$867$$

$$868$$

869 where we utilize the brackets $\langle \cdot \rangle$ to denote the expectation value with respect to the effective distribution
 870 $P_0(\vec{a})e^{-\vec{a}^2 e^{-2t}/(2\Delta_t)}$. Therefore, the expansion can be used to show that at large times:
 871

$$872 \quad \log P_t(\vec{x}) = C + \frac{e^{-t}}{\Delta_t} \sum_{i=1}^d x_i \langle a_i \rangle - \frac{1}{2\Delta_t} \sum_{i,j=1}^d x_i M_{ij} x_j + O\left((xe^{-t})^3\right),$$

$$873$$

$$874$$

$$875$$

876 where C is an \vec{x} -independent term and
 877

$$878 \quad M_{ij} = \delta_{ij} - e^{-2t} \left[\langle a_i a_j \rangle - \langle a_i \rangle \langle a_j \rangle \right].$$

$$879$$

880 The curvature of $\log P_t(\vec{x})$ is closely linked to the spectral properties of the matrix M . In the large
 881 time regime, M approaches the identity matrix, and consequently, all its eigenvalues are positive.
 882 However, a qualitative shift in shape occurs at the maximum time t_s , where the largest eigenvalue
 883 of M transitions through zero. This marks the onset of the **speciation time**, distinguished by a
 884 change in curvature of the effective potential $-\log P_t(\vec{x})$. In this case, it can be easily computed:
 885 the matrix M is given by $M_{ij} = (1 - \sigma^2 e^{-2t}) \delta_{ij} - e^{-2t} m_i m_j$ and its largest eigenvalue is
 886 $(1 - \sigma^2 e^{-2t} - d\tilde{\mu}^2 e^{-2t})$. We get therefore in the large d limit $t_s = \frac{1}{2} \log(d\tilde{\mu}^2)$ which up to
 887 subleading corrections identifies the speciation timescale as
 888

$$889 \quad t_s = \frac{1}{2} \log(d).$$

$$890$$

892 B THEORETICAL PROOFS: TWO EQUIDISTANT, SYMMETRIC GAUSSIAN 893 MIXTURES

894 ASYMPTOTIC STOCHASTIC PROCESS IN REGIME I AND SYMMETRY BREAKING

895 In the limit of large dimensions, a comprehensive analytical examination of the dynamics in Regime
 896 I, taking place on time-scales $t_s + O(1) = (1/2) \log d + O(1)$, can be provided, specifically at the
 897 beginning of the backward process. Assuming no collapse (for further details, refer to [Biroli et al.](#)
 898 (2024)), an investigation into diffusion dynamics shows that the empirical distribution $P_t^e(\vec{x})$ at time
 899 t can be approximated with high accuracy by $P_t(\vec{x})$. This approximation represents the convolution
 900 of the initial distribution P_0 , comprising a mixture of Gaussians centered at $\pm \vec{m}$, and a diffusion
 901 kernel proportional to $e^{-(\vec{x} - \vec{a}e^{-t})^2/2}$. Consequently, the explicit expression for this approximation
 902 is
 903

$$904 \quad P_0(\vec{x}) = \frac{1}{2 \left(\sqrt{2\pi\sigma^2} \right)^d} \left[e^{-(\vec{x} - \vec{m})^2/(2\sigma^2)} + e^{-(\vec{x} + \vec{m})^2/(2\sigma^2)} \right], \text{ and} \quad (10)$$

$$905$$

$$906$$

$$907$$

$$908$$

$$909 \quad P_t(\vec{x}) = \frac{1}{2 \left(\sqrt{2\pi\Gamma_t} \right)^d} \left[e^{-(\vec{x} - \vec{m}e^{-t})^2/(2\Gamma_t)} + e^{-(\vec{x} + \vec{m}e^{-t})^2/(2\Gamma_t)} \right]$$

$$910$$

$$911$$

$$912$$

913 where $\Gamma_t = \sigma^2 e^{-2t} + \Delta_t$ goes to 1 at large times. The log of this probability is
 914

$$915 \quad \log P_t(\vec{x}) = -\frac{\vec{x}^2}{2\Gamma_t} + \log \cosh \left(\vec{x} \cdot \vec{m} \frac{e^{-t}}{\Gamma_t} \right),$$

$$916$$

$$917$$

918 and hence the score reads
 919

$$920 \\ 921 \quad S_t^i(\vec{x}) = -\frac{x^i}{\Gamma_t} + m_i \frac{e^{-t}}{\Gamma_t} \tanh \left(\vec{x} \cdot \vec{m} \frac{e^{-t}}{\Gamma_t} \right). \\ 922 \\ 923$$

924 As there are two classes: $+\vec{m}$ and $-\vec{m}$, the score conditioned to one class equals the score associated
 925 to a given Gaussian. Therefore, for the two classes we have:

$$926 \\ 927 \quad + \vec{m} : S_t^i(\vec{x}, +) = \frac{-x^i + m_i e^{-t}}{\Gamma_t}, \text{ and} \\ 928 \\ 929 \quad - \vec{m} : S_t^i(\vec{x}, -) = \frac{-x^i - m_i e^{-t}}{\Gamma_t}. \\ 930 \\ 931$$

932 B.1 RESULT I: WHAT IS THE ROLE OF CLASSIFIER-FREE GUIDANCE?

933 Let us first analyze the “transverse” directions $\vec{v} \perp \vec{m}$. For these directions, for all ω , the score is the
 934 same and equals $\vec{S}_t^{\text{CFG}}(\vec{x}, c) \cdot \vec{v} = -\frac{\vec{x} \cdot \vec{v}}{\Gamma_t}$. Let us project the backward Eq. (2) on a unit vector $\vec{v} \perp \vec{m}$.
 935 We write $p = \vec{x} \cdot \vec{v}$, and the backward equation now reads $dp = p(1 - 2/\Gamma_{t_f - \tau})d\tau + \sqrt{2}dB$ which
 936 is the backward equation for a single Gaussian variable. When $\tau \rightarrow t_f$ the projection $p = \vec{x} \cdot \vec{v}$ is
 937 thus distributed as $\mathcal{N}(0, \sigma^2)$, for all values of ω .
 938

939 Therefore, as all the components except the one in the \vec{m} direction are not affected, we can consider
 940 only the component along \vec{m} :

$$941 \\ 942 \quad \vec{S}_{t_{CFG}}(\vec{x}, c) \cdot \frac{\vec{m}}{|\vec{m}|} = -\frac{\vec{x} \cdot \vec{m}/|\vec{m}|}{\Gamma_t} + \omega \frac{|\vec{m}|^2 e^{-t}}{|\vec{m}| \Gamma_t} \cdot \left\{ c - \tanh \left(\frac{\vec{x} \cdot \vec{m} e^{-t}}{\Gamma_t} \right) \right\} + \frac{|\vec{m}| e^{-t} c}{\Gamma_t}. \\ 943 \\ 944$$

945 By denoting $\frac{\vec{x} \cdot \vec{m}}{|\vec{m}|} = q(t)$, where $|\vec{m}| = \sqrt{d}$, we can obtain the backward equation:

$$946 \\ 947 \quad dx^i = (x^i + 2S_{t_{CFG}}^i) d\tau + d\eta_i(\tau), \\ 948$$

949 where $\tau = t_f - t$, i.e., the backward time. Therefore, we can obtain for Regime I and by projecting
 950 onto the $\frac{\vec{m}}{|\vec{m}|}$ direction, we have that:

$$951 \\ 952 \quad dq = dx^i \cdot \frac{\vec{m}}{|\vec{m}|} = \left(q + 2 \left[-q + e^{-(t_f - t_s - \tau)} \left((1 + \omega) - \omega \tanh \left(q e^{-(t_f - t_s - \tau)} \right) \right) \right] \right) d\tau + d\eta(\tau), \\ 953$$

954 as, in Regime I, we have that $\Gamma_t \approx 1$, and also $\sqrt{d} = e^{-t_s}$.

955 Again, from this point onward by $t(\tau)$ we denote the backward time for ease of notation. This is
 956 like having an effective potential:

$$957 \\ 958 \quad dq = -\frac{\partial V^{\text{CFG}}(q, \tau)}{\partial q} d\tau + d\eta(\tau), \\ 959$$

960 where

$$961 \\ 962 \quad V^{\text{CFG}} = \frac{1}{2} q^2 + 2 \left[-(1 + \omega) c q e^{-(t - t_s)} + \omega \ln \cosh \left(q e^{-(t - t_s)} \right) \right] \\ 963 \\ 964 \quad = \underbrace{\left(\frac{1}{2} q^2 - 2 e^{-(t - t_s)} c q \right)}_{\text{Classifier's potential}} + \underbrace{\omega \left[-c q e^{-(t - t_s)} + \ln \cosh \left(q e^{-(t - t_s)} \right) \right]}_{\text{Extra potential } V_{\text{extra}}}. \\ 965 \\ 966$$

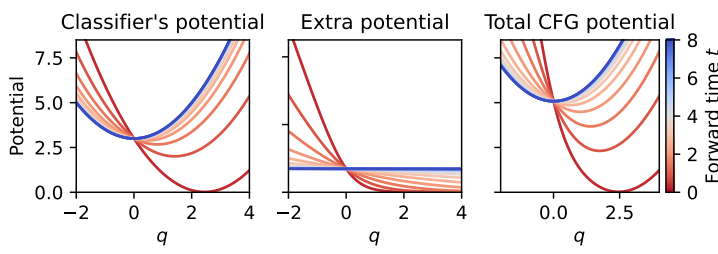


Figure 7: **Effect of CFG on the guiding potential of a Gaussian mixture.** The backward diffusion for the variable q giving the projection of \vec{x} on the center \vec{m} of the Gaussian where one wants to guide the backward diffusion. From left to right: Potential within the class, CFG-added-potential V_{extra} with $\omega = 2$, and their sum as in Eq. (6). CFG exhibits faster convergence to the target ($t = 0$), but results in narrower potential for small t (with t ranging from 0 to 8, as indicated on the right panel).

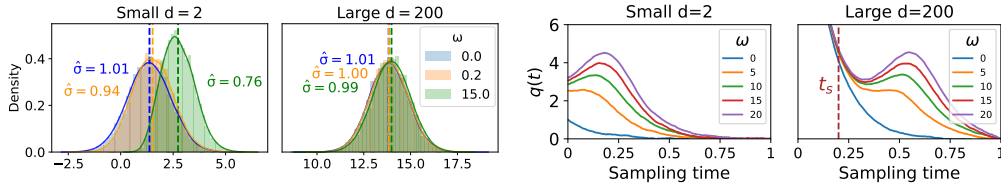


Figure 8: **Left: CFG produces the exact target distribution in high dimensions.** We simulate the backward process using a two Gaussian mixture. We project and plot the generated samples onto the target mean $+\vec{m}$: $q(t = 0) = \vec{x} \cdot \vec{m} / |\vec{m}|$. For small $d = 2$, CFG generates a distribution with larger magnitude mean (dashed line) and smaller variance than the target one (for $\omega = 0$). This effect diminishes as the dimension increases: for $d = 200$ it is practically absent. **Right: High-dimensionality of the data allows CFG trajectories to align.** We plot the evolution of the mean of trajectories $q(t)$: starting at large forward times denoted with $t = 1$ (noise), for small $d = 2$, CFG trajectories do not align with the unconditional trajectories at $t = 0$ (data) causing the CFG overshoot. For large dimension $d = 200$, the high-dimensionality of the data allows trajectories to realign with the unguided one at speciation time t_s , resulting in the correct target distribution.

Therefore, for class $c = +1$ (equivalently for $c = -1$), there is little effect for $qe^{-(t-t_s)} \gg 1$, as then $-qe^{-(t-t_s)} + \ln \cosh(qe^{-(t-t_s)}) \approx 0$. Instead, for $qe^{-(t-t_s)} \sim O(1)$, we have that $-qe^{-(t-t_s)} + \ln \cosh(qe^{-(t-t_s)}) \sim O(1)$. Therefore, we can conclude our first result:

Result I. In Regime I, before speciation time t_s , CFG is effective in aiding class selection and speeds up the convergence towards the target class c .

The utility of CFG is therefore to "push" in the right direction in Regime I where arguably the class-based score/potential is likely not accurate in the rare region ($q > 0$ for $c = -1$ and $q < 0$ for $c = +1$). The behavior of the two potentials is displayed in Figure 7.

B.2 RESULT II: PATH ALIGNMENT

The role of CFG in Regime I is to push the trajectories more in the direction of the selected class. We recall that the SDE verified by q when pushed towards class $c = +1$ reads:

$$dq = \left(q + 2 \left[-q + e^{-(t_f-t_s-\tau)} \left((1 + \omega) - \omega \tanh(qe^{-(t_f-t_s-\tau)}) \right) \right] \right) d\tau + d\eta(\tau), \quad (13)$$

For large times but still during Regime I, i.e. $t_f - t_s \ll \tau \ll 1/2 \log d$, q is very large (positive or negative). In this regime the CFG term can be neglected as it leads to exponentially small corrections to the SDE (of order $e^{-2qe^{-(t_f-t_s-\tau)}}$) with $t_f - t_s - \tau \gg 1$. In consequence, in Regime I at large times, the SDE just reads:

$$dq = -q + 2e^{-(t_f-t_s-\tau)} + d\eta(\tau),$$

The effect of CFG is to lead to different values of q when entering this late regime of Regime I. We call these values $q(\tau_i)$ and denote τ_i the fixed time at which the CFG contribution can be neglected. The value $q(\tau_i)$ is quickly (exponentially) forgotten when τ departs from τ_i , i.e., the evolution readjust to the correct value without CFG. This can be shown by solving the SDE starting from a given τ_i :

$$q(\tau) = q(\tau_i)e^{-(\tau-\tau_i)} + e^{-(t_f-t_s)} \left(e^\tau - e^{-\tau+2\tau_i} \right) + \sqrt{1 - e^{-(2(\tau-\tau_i))}} z_\tau$$

where z_τ is a Gaussian variable with mean zero and unit variance. When $\tau \gg \tau_i$ but still in Regime I the solution of the SDE does not depend any longer on $q(\tau_i)$ and it coincides statistically with the one of the backward process of the single Gaussian corresponding to the class $c = +1$. This allows to conclude the second result:

Result II. Just before speciation time t_s , CFG-guided paths realign with the unguided path that generates the correct, unmodified target distribution.

B.3 RESULT III: WHEN DOES CLASSIFIER-FREE GUIDANCE TAKE EFFECT?

We can proceed to answer this question by examining the classifier-free guidance score, as defined in [Ho & Salimans \(2022\)](#):

$$S_{t_{CFG}}^i(\vec{x}, c) = (1 + \omega)S_t^i(\vec{x}, c) - \omega S_t^i(\vec{x}), \quad (14)$$

where $c = \pm 1$ and $\omega > 0$. By plugging in the cond. (12) and uncond. scores (11), we can obtain:

$$\begin{aligned} S_{t_{CFG}}^i(\vec{x}, c) &= -\frac{x^i}{\Gamma_t} + (1 + \omega) \frac{cm_i e^{-t}}{\Gamma_t} - \omega \frac{m_i e^{-t}}{\Gamma_t} \tanh\left(\frac{\vec{x} \cdot \vec{m} e^{-t}}{\Gamma_t}\right) \\ &= -\frac{x^i}{\Gamma_t} + \omega \frac{m_i e^{-t}}{\Gamma_t} \left\{ c - \tanh\left(\frac{\vec{x} \cdot \vec{m} e^{-t}}{\Gamma_t}\right) \right\} + \frac{cm_i e^{-t}}{\Gamma_t}. \end{aligned} \quad (15)$$

Now, in Regime II, when the trajectory has committed to a given class, $\vec{x} \cdot \vec{m} \sim O(d)$ and $\text{sign}(\vec{x} \cdot \vec{m}) = c$. Therefore, $c - \tanh\left(\frac{\vec{x} \cdot \vec{m} e^{-t}}{\Gamma_t}\right) \approx 0$, and one finds from (15), that $S_{t_{CFG}}^i(\vec{x}, c) = S_t^i(\vec{x})$. This implies that, within this regime, classifier-free guidance equals the conditional score. Therefore, Classifier free-guidance only affects Regime I, as $S_{t_{CFG}}^i(\vec{x}, c) = S_t^i(\vec{x})$ for $t > t_s = \frac{1}{2} \log(d)$. This allows us to conclude the third result:

Result III. In Regime II, after speciation time t_s , CFG has no effect on the generation process.

C GENERALIZATIONS OF THE PROOF

In this section, we present arguments for extending our proofs to more general cases. We start by discussing proof generalization for non-centered Gaussian mixtures (Section C.1) and then move on to a mixture of four Gaussians (C.2). Finally, we conclude with some remarks on how to further extend these results to more complex scenarios.

C.1 GENERALIZATION TO NON-CENTERED GAUSSIAN MIXTURES

C.2 ASYMPTOTIC STOCHASTIC PROCESS IN REGIME I AND SYMMETRY BREAKING

Here we provide an example on how to generalize the study of Gaussian mixtures to the case where the two Gaussians are centered in \vec{m}_1 and \vec{m}_2 . We take \vec{m}_1, \vec{m}_2 as two arbitrary vectors in d dimensions, on the sphere $|\vec{m}_c|^2 = d$ the case where they have different norms, both scaling proportionally to d , could be studied as well with the same formalism.

The initial probability density is

1080
1081
1082
$$P_0(\vec{x}) = \frac{1}{2 \left(\sqrt{2\pi\sigma^2} \right)^d} \left[e^{-(\vec{x}-\vec{m}_1)^2/(2\sigma^2)} + e^{-(\vec{x}-\vec{m}_2)^2/(2\sigma^2)} \right], \text{ and} \quad (16)$$

1083
1084
1085
$$P_t(\vec{x}) = \frac{1}{2 \left(\sqrt{2\pi\Gamma_t} \right)^d} \left[e^{-(\vec{x}-\vec{m}_1 e^{-t})^2/(2\Gamma_t)} + e^{-(\vec{x}-\vec{m}_2 e^{-t})^2/(2\Gamma_t)} \right]$$

1086
1087
1088

where $\Gamma_t = \sigma^2 e^{-2t} + \Delta_t$ goes to 1 at large times. The log of this probability is

1090
1091
$$\log P_t(\vec{x}) = -\frac{\vec{x}^2}{2\Gamma_t} + \log \left(e^{\vec{x} \cdot \vec{m}_1 \frac{e^{-t}}{\Gamma_t}} + e^{\vec{x} \cdot \vec{m}_2 \frac{e^{-t}}{\Gamma_t}} \right) + C,$$

1092
1093

where C is a constant, and hence the score reads

1094
1095
1096
$$S_t^i(\vec{x}) = -\frac{x^i}{\Gamma_t} + \frac{e^{-t}}{\Gamma_t} \frac{m_1^i e^{\vec{x} \cdot \vec{m}_1 \frac{e^{-t}}{\Gamma_t}} + m_2^i e^{\vec{x} \cdot \vec{m}_2 \frac{e^{-t}}{\Gamma_t}}}{e^{\vec{x} \cdot \vec{m}_1 \frac{e^{-t}}{\Gamma_t}} + e^{\vec{x} \cdot \vec{m}_2 \frac{e^{-t}}{\Gamma_t}}} \quad (17)$$

1097
1098

As there are two classes: \vec{m}_1 and \vec{m}_2 , the score conditioned to one class equals the score associated to a given Gaussian. Therefore, for the two classes we have:

1101
1102
$$\vec{m}_1 : S_t^i(\vec{x}, +) = \frac{-x^i + m_1^i e^{-t}}{\Gamma_t}, \text{ and} \quad (18)$$

1103
1104
1105
$$\vec{m}_2 : S_t^i(\vec{x}, -) = \frac{-x^i - m_2^i e^{-t}}{\Gamma_t}.$$

1106

WHAT IS THE ROLE OF CLASSIFIER-FREE GUIDANCE?

We shall use as basis the vectors $\vec{m}_+ = (\vec{m}_1 + \vec{m}_2)/2$, $\vec{m}_- = (\vec{m}_1 - \vec{m}_2)/2$, and we shall denote by \vec{v} the vectors orthogonal to the place generated by \vec{m}_1, \vec{m}_2 .

For these “transverse” directions $\vec{v} \perp (\vec{m}_1, \vec{m}_2)$. for all ω , the score is the same and equals $\vec{S}_t^{\text{CFG}}(\vec{x}, c) \cdot \vec{v} = -\frac{\vec{x} \cdot \vec{v}}{\Gamma_t}$. Let us project the backward equation on a unit vector \vec{v} in the transverse space. We write $p = \vec{x} \cdot \vec{v}$, and the backward equation now reads $dp = p(1 - 2/\Gamma_{t_f} - \tau) d\tau + \sqrt{2} dB$ which is the backward equation for a single Gaussian variable. When $\tau \rightarrow t_f$ the projection $p = \vec{x} \cdot \vec{v}$ is thus distributed as $\mathcal{N}(0, \sigma^2)$, for all values of ω .

Therefore, as all the components except the ones in the \vec{m}_+ and \vec{m}_- directions are not affected.

We now project the score on \vec{m}_+ and \vec{m}_- , using $\vec{m}_+ \cdot \vec{m}_- = 0$, $\vec{m}_+ \cdot \vec{m}_1 = \vec{m}_+ \cdot \vec{m}_2 = d^2/2$ and $\vec{m}_- \cdot \vec{m}_1 = -\vec{m}_- \cdot \vec{m}_2 = d^2/2$:

1120
1121
$$\vec{S}_{t_{CFG}}(\vec{x}, c) \cdot \vec{m}_+ = \frac{(\vec{m}_+ e^{-t} - \vec{x}) \cdot \vec{m}_+}{\Gamma_t}$$

1122
1123
$$\vec{S}_{t_{CFG}}(\vec{x}, c) \cdot \vec{m}_- = \frac{(\vec{m}_- e^{-t} - \vec{x}) \cdot \vec{m}_-}{\Gamma_t} + \omega \frac{|\vec{m}_-|^2 e^{-t}}{\Gamma_t} \cdot \left\{ 1 - \tanh \left(\frac{\vec{x} \cdot \vec{m}_- e^{-t}}{\Gamma_t} \right) \right\}$$

1124
1125

Inserting these scores into the backward diffusion equation, one finds that:

1126
1127
1128

- $\vec{x} \cdot \vec{m}_+ / |\vec{m}_+|$ evolves as a Gaussian variable. At time $\tau \rightarrow t_f$ the distribution of this variable is $\mathcal{N}(|\vec{m}_+|, \sigma^2)$.
1129
1130 - The variable $q_-(t) = \frac{\vec{x} \cdot \vec{m}_-}{|\vec{m}_-|}$ satisfies the same equation as the variable $q(t)$ which we analyzed in the ‘centered’ case where $\vec{m}_1 = -\vec{m}_2 = \vec{m}$
1131
1132

Therefore, we can conclude that in this case, CFG has the same effect: it is effective in aiding class selection, speeding up the convergence toward the correct target class c .

1134 WHEN DOES CLASSIFIER-FREE GUIDANCE TAKE EFFECT?

1135
1136 We can proceed to answer this question by examining the classifier-free guidance score:

1137

1138
$$S_{t_{CFG}}^i(\vec{x}, c) = (1 + \omega)S_t^i(\vec{x}, c) - \omega S_t^i(\vec{x}), \quad (19)$$

1139 where $c \in \{1, 2\}$ and $\omega > 0$. The CFG score guiding to class $c = 1$ is thus:

1140
1141
$$S_{t_{CFG}}^i(\vec{x}, c) = -\frac{x^i}{\Gamma_t} + (1 + \omega) \frac{m_1^i e^{-t}}{\Gamma_t} - \omega \frac{e^{-t}}{\Gamma_t} \frac{m_1^i e^{\vec{x} \cdot \vec{m}_1 \frac{e^{-t}}{\Gamma_t}} + m_2^i e^{\vec{x} \cdot \vec{m}_2 \frac{e^{-t}}{\Gamma_t}}}{e^{\vec{x} \cdot \vec{m}_1 \frac{e^{-t}}{\Gamma_t}} + e^{\vec{x} \cdot \vec{m}_2 \frac{e^{-t}}{\Gamma_t}}} \quad (20)$$

1142 Now, in Regime II, when the trajectory has committed to a given class say class $1*$, $\vec{x} \cdot \vec{m}_1 - \vec{x} \cdot \vec{m}_2$ is
1143 positive and of order $O(d)$. Therefore $S_{t_{CFG}}^i(\vec{x}, c) = S_t^i(\vec{x}, c)$. This implies that, within this regime,
1144 classifier-free guidance equals the conditional score. Therefore, Classifier free-guidance only affects
1145 Regime I, as $S_{t_{CFG}}^i(\vec{x}, c) = S_t^i(\vec{x})$ for $t > t_s = \frac{1}{2} \log(d)$. This allows us to conclude that in Regime
1146 II, CFG is innocuous.1147 Therefore all the results obtained for the centered case $\vec{m}_1 = -\vec{m}_2 = \vec{m}$ also hold for the more
1148 general case when the two Gaussians are centered in \vec{m}_1 and \vec{m}_2 .1149
1150 C.2 EXTENSION TO THE MIXTURE OF FOUR GAUSSIANS1151 Here we present the computation for a mixture of four Gaussians, in order to analyze the behavior of
1152 the system for an increasing number of classes and emphasize the extendability of our framework.
1153 As before, assuming no collapse, we can approximate the empirical distribution $P_t^e(\vec{x})$ at time t by
1154 $P_t(\vec{x})$ with high accuracy. In this case, the approximation represents the convolution of the initial
1155 distribution P_0 , being a mixture of 4 Gaussians centered at $\pm \vec{\mu}_1 \pm \vec{\mu}_2$, s.t. $\vec{\mu}_1 \cdot \vec{\mu}_2 = 0$, and a diffusion
1156 kernel proportional to $e^{-(\vec{x} - \vec{a}e^{-t})^2/2}$. The explicit expression for the distribution is:

1157
1158
$$P_0(\vec{x}) = \frac{1}{4(\sqrt{2\pi\sigma^2})^d} \left[e^{-(\vec{x} - (\vec{\mu}_1 - \vec{\mu}_2))^2/(2\sigma^2)} + e^{-(\vec{x} - (\vec{\mu}_1 + \vec{\mu}_2))^2/(2\sigma^2)} \right. \\ \left. + e^{-(\vec{x} + (\vec{\mu}_1 - \vec{\mu}_2))^2/(2\sigma^2)} + e^{-(\vec{x} + (\vec{\mu}_1 + \vec{\mu}_2))^2/(2\sigma^2)} \right]$$

1159 and

1160
1161
$$P_t(\vec{x}) = \frac{1}{4(\sqrt{2\pi\Gamma_t})^d} \left[e^{-(\vec{x} - (\vec{\mu}_1 - \vec{\mu}_2)e^{-t})^2/(2\Gamma_t)} + e^{-(\vec{x} - (\vec{\mu}_1 + \vec{\mu}_2)e^{-t})^2/(2\Gamma_t)} \right. \\ \left. + e^{-(\vec{x} + (\vec{\mu}_1 - \vec{\mu}_2)e^{-t})^2/(2\Gamma_t)} + e^{-(\vec{x} + (\vec{\mu}_1 + \vec{\mu}_2)e^{-t})^2/(2\Gamma_t)} \right]$$

1162 where $\Gamma_t = \sigma^2 e^{-2t} + \Delta_t$ goes to 1 at large times. This can be rewritten as:

1163
1164
$$P_t(\vec{x}) = \frac{1}{2(\sqrt{2\pi\Gamma_t})^d} e^{-(\vec{x}^2 + \vec{\mu}_1^2 e^{-2t} + \vec{\mu}_2^2 e^{-2t})/(2\Gamma_t)} \left[e^{-\vec{\mu}_1 \cdot \vec{\mu}_2 e^{-2t}/\Gamma_t} \cosh\left(\vec{x} \cdot (\vec{\mu}_1 + \vec{\mu}_2) \frac{e^{-t}}{\Gamma_t}\right) \right. \\ \left. + e^{\vec{\mu}_1 \cdot \vec{\mu}_2 e^{-2t}/\Gamma_t} \cosh\left(\vec{x} \cdot (\vec{\mu}_1 - \vec{\mu}_2) \frac{e^{-t}}{\Gamma_t}\right) \right]$$

1165 The log of this probability is:

1166
1167
$$\log P_t(\vec{x}) = \frac{-\vec{x}^2}{2\Gamma_t} + \log \left(e^{-\vec{\mu}_1 \cdot \vec{\mu}_2 e^{-2t}/\Gamma_t} \cosh\left(\vec{x} \cdot (\vec{\mu}_1 + \vec{\mu}_2) \frac{e^{-t}}{\Gamma_t}\right) + e^{\vec{\mu}_1 \cdot \vec{\mu}_2 e^{-2t}/\Gamma_t} \cosh\left(\vec{x} \cdot (\vec{\mu}_1 - \vec{\mu}_2) \frac{e^{-t}}{\Gamma_t}\right) \right)$$

1188 And the score reads:
 1189

$$1190 \quad S_t^i(\vec{x}) = \frac{-x^i}{\Gamma_t} \\ 1191 \quad S_t^i(\vec{x}) = \frac{-x^i}{\Gamma_t} \\ 1192 \quad + \frac{e^{-t} (\vec{\mu}_1 + \vec{\mu}_2)_i e^{-\vec{\mu}_1 \cdot \vec{\mu}_2 e^{-2t}/\Gamma_t} \sinh\left(\vec{x} \cdot (\vec{\mu}_1 + \vec{\mu}_2) \frac{e^{-t}}{\Gamma_t}\right) + (\vec{\mu}_1 - \vec{\mu}_2)_i e^{\vec{\mu}_1 \cdot \vec{\mu}_2 e^{-2t}/\Gamma_t} \sinh\left(\vec{x} \cdot (\vec{\mu}_1 - \vec{\mu}_2) \frac{e^{-t}}{\Gamma_t}\right)}{\Gamma_t} e \\ 1193 \quad + \frac{e^{-\vec{\mu}_1 \cdot \vec{\mu}_2 e^{-2t}/\Gamma_t} \cosh\left(\vec{x} \cdot (\vec{\mu}_1 + \vec{\mu}_2) \frac{e^{-t}}{\Gamma_t}\right) + e^{\vec{\mu}_1 \cdot \vec{\mu}_2 e^{-2t}/\Gamma_t} \cosh\left(\vec{x} \cdot (\vec{\mu}_1 - \vec{\mu}_2) \frac{e^{-t}}{\Gamma_t}\right)}{\Gamma_t} e \\ 1194 \quad + \frac{e^{-\vec{\mu}_1 \cdot \vec{\mu}_2 e^{-2t}/\Gamma_t} \cosh\left(\vec{x} \cdot (\vec{\mu}_1 + \vec{\mu}_2) \frac{e^{-t}}{\Gamma_t}\right) + e^{\vec{\mu}_1 \cdot \vec{\mu}_2 e^{-2t}/\Gamma_t} \cosh\left(\vec{x} \cdot (\vec{\mu}_1 - \vec{\mu}_2) \frac{e^{-t}}{\Gamma_t}\right)}{\Gamma_t} e \\ 1195 \quad + \frac{e^{-\vec{\mu}_1 \cdot \vec{\mu}_2 e^{-2t}/\Gamma_t} \cosh\left(\vec{x} \cdot (\vec{\mu}_1 + \vec{\mu}_2) \frac{e^{-t}}{\Gamma_t}\right) + e^{\vec{\mu}_1 \cdot \vec{\mu}_2 e^{-2t}/\Gamma_t} \cosh\left(\vec{x} \cdot (\vec{\mu}_1 - \vec{\mu}_2) \frac{e^{-t}}{\Gamma_t}\right)}{\Gamma_t} e \\ 1196$$

1197 As \vec{x} approaches one of the means $\pm \vec{\mu}_1 \pm \vec{\mu}_2$, the second summand reduces to $(\vec{\mu}_1 \pm \vec{\mu}_2) \tanh\left(x \cdot (\vec{\mu}_1 \pm \vec{\mu}_2) \frac{e^{-t}}{\Gamma_t}\right)$ ³, resulting in an expression akin to the one for mixture of 2 Gaussians in (11).

1201 C.3 CONCLUSION AND FURTHER EXTENSIONS

1202 The results above can be generalized to any finite number of Gaussians, centered around \vec{m}_i where
 1203 \vec{m}_i is a vector of norm $\mu_i \sqrt{d}$. CFG will only have effect on space spanned by vectors \vec{m}_i and
 1204 only in regime I. One can also consider non-isotropic Gaussians. As long as the covariance has
 1205 eigenvalues not scaling with d , the backward process displays the two distinct regimes I and II, which
 1206 is examined in detail for the mixture of two Gaussians. This result can be obtained by analyzing the
 1207 forward process. The key point is that on all times of order one the noised Gaussian mixture still
 1208 consists in non-overlapping Gaussian (regime II). On times of order one close to the speciation time
 1209 $1/2 \log d$ the Gaussians overlap and the center are of the same order of the noise (regime I). Because
 1210 of the existence of these two regimes, the general arguments presented at the beginning of the paper
 1211 hold and CFG does reproduce the correct distribution in the large d limit.

1212 The results derived for the Gaussian mixture model provide a foundation for broader application.
 1213 We also note two key points regarding the robustness and scope of this analysis:

1214 **Robustness and Generalization Beyond Gaussian Mixtures:** The core features of regimes I and
 1215 II persist even in more complex, high-dimensional settings, extending beyond the specific case of
 1216 Gaussian mixtures. Several studies Ventura et al. (2024); Achilli et al. (2025); Bae et al. (2024)
 1217 have demonstrated that these regimes apply more broadly to models where data is distributed on
 1218 manifolds, among other configurations. This robustness is a direct consequence of the infinite-
 1219 dimensional limit, a phenomenon also observed in other domains like supervised learning.

1220 **Scope and Future Work:** The spirit of our approach is twofold: (i) To analyze CFG in the tractable
 1221 yet rich setting of infinite dimensions. (ii) To start with the simplest nontrivial case—a mixture of
 1222 two Gaussians—to characterize the fundamental mechanisms that can guide future work.

1223 As noted, a natural and straightforward extension is to consider mixtures involving any finite num-
 1224 ber of Gaussians. Further generalizations—such as data supported on hidden manifolds—can be
 1225 pursued by following the methodologies established in studies like Bae et al. (2024) and George
 1226 et al. (2025).

1228 C.4 RELATION TO OTHER MODELS

1229 In this section we briefly note how our theoretical results connect to a broader range of methods
 1230 related to diffusion and flow matching, specifically how nonlinear CFG applies to 1-step flow models
 1231 (Chen et al., 2025a) and methods that learn optimal source distributions (Lee et al., 2023).

1232 **Regarding one-step models.** Since the main distinction between regimes lies in whether class
 1233 membership is decided, a 1-step flow model effectively jumps from the initial point (part of Regime
 1234 I) directly into Regime II (in fact, directly into the third regime described in Chen et al. (2025a)).
 1235 However, this does not pose a problem as theoretically the difference between the conditional and
 1236 unconditional score equals zero (under the correct score assumption and in sufficiently high di-
 1237 mension); thus, regardless whether CFG is applied or not these models obtain the correct target
 1238 distribution. In practice, we believe that the models could still benefit from non-linear guidances.

1239
 1240 ³For large values of $x \cdot (\vec{\mu}_1 \pm \vec{\mu}_2) e^{-t}/\Gamma_t$, we utilized the *log-sum-exp trick* to calculate the value of the
 1241 fraction.

1242 **Regarding methods that learn an optimal source distribution for flows** Methods such as Fast-
 1243 ODE (Lee et al., 2023) that successfully map similar inputs to the same class indeed shorten, or
 1244 even eliminate Regime I—for example, if the initial distribution is a Gaussian mixture (GM) where
 1245 each mixture has successfully been mapped to a distinct class, e.g., by using GM-Flow matching
 1246 (Lee et al., 2023), Regime I would be eliminated altogether. One should note that in these cases it is
 1247 likely that CFG would not prove as beneficial. In fact, this is exactly the finding of the authors in Lee
 1248 et al. (2023), in which an alternative guidance method is proposed as CFG was not found to perform
 1249 as well. However, our nonlinear guidance retains an advantage: the flexibility of $\alpha > 0$ vs. $\alpha < 0$.
 1250 In our experiments (starting from standard Gaussian noise with significant class overlap in the initial
 1251 distribution), the former proved beneficial by amplifying guidance when score differences are large
 1252 and suppressing CFG when small. It would be interesting future work to test whether indeed $\alpha < 0$
 1253 would be beneficial in settings with prominent separations in the initial distributions, as might occur
 1254 in FastODE-like mappings or GM-Flows (Chen et al., 2025a).

D FINITE DIMENSION

1255 In this section, we give exact analyses describing the effect of CFG in finite- (possibly low-) di-
 1256 mensional settings, outlined in Section 4.2 in the main manuscript. We start the backward equation
 1257 at a time t_f large enough that the distribution of x is a isotropic Gaussian with variance one. The
 1258 backward equation for $x(t)$ with the CFG score reads:

$$\begin{aligned} \frac{dx^i}{d\tau} = & x^i \left(1 - \frac{2}{\Gamma(t_f - \tau)} \right) + \frac{2m_i}{\Gamma(t_f - \tau)} e^{-(t_f - \tau)} \\ & + 2\omega m_i \frac{e^{-(t_f - \tau)}}{\Gamma_{t_f - \tau}} \left\{ 1 - \tanh \left(\frac{\vec{x} \cdot \vec{m} e^{-(t_f - \tau)}}{\Gamma_{t_f - \tau}} \right) \right\} + \eta_i(\tau) \end{aligned} \quad (21)$$

1259 where $\tau = 0$ at the beginning of the backward process and $\tau = t_f (\gg 1)$ at the end.

1260 This can be projected on the evolution of the single parameter $q(\tau) = \vec{x} \cdot \vec{m} / \sqrt{d}$. We obtain

$$\begin{aligned} \frac{dq}{d\tau} = & q \left(1 - \frac{2}{\Gamma(t_f - \tau)} \right) + \frac{2\sqrt{d}}{\Gamma(t_f - \tau)} e^{-(t_f - \tau)} \\ & + 2\omega \sqrt{d} \frac{e^{-(t_f - \tau)}}{\Gamma_{t_f - \tau}} \left\{ 1 - \tanh \left(\frac{q\sqrt{d} e^{-(t_f - \tau)}}{\Gamma_{t_f - \tau}} \right) \right\} + \eta(\tau). \end{aligned} \quad (22)$$

1261 Considering the right-hand side as a force due to a moving external potential $-\partial_q V(q, t)$, the effect
 1262 of CFG is to add an extra term which has two main effects: (1) it adds a positive term to the force
 1263 and, in consequence, it pushes q faster away from zero, (2) it increases the value of the Hessian at
 1264 any point in q with respect to its $\omega = 0$ counterpart, thus making the potential more confining.

1265 The initial condition is $q(\tau = 0) \sim \mathcal{N}(0, \sigma^2)$ and

$$1266 \Gamma(t_f - \tau) = \sigma^2 e^{-2(t_f - \tau)} + 1 - e^{-2(t_f - \tau)}. \quad (23)$$

1267 CASE: $\omega = 0$

1268 The solution of the backward equation is:

$$1269 q(\tau) = q(0) e^{\tau - 2 \int_0^\tau \frac{1}{\Gamma(t_f - \tau'')} d\tau''} + \int_0^\tau \left[\frac{2\sqrt{d} e^{-(t_f - \tau')}}{\Gamma(t_f - \tau')} + \eta_i(\tau') \right] e^{(\tau - \tau') - 2 \int_{\tau'}^\tau \frac{1}{\Gamma(t_f - \tau'')} d\tau''} d\tau'. \quad (24)$$

1270 Its probability distribution must coincide with the one of the solutions of the forward equation, which
 1271 reads:

$$1272 q(t) = \sqrt{d} e^{-t} + \sqrt{1 - e^{-2t}} z_i + e^{-t} \sigma \tilde{z}_i,$$

1296 where $z_i, \tilde{z}_i \sim \mathcal{N}(0, 1)$ and $t = t_f - \tau$. Let us now focus on the mean of q . When we consider
 1297

$$1298 \int_0^\tau \left[\frac{2\sqrt{d}e^{-(t_f-\tau')}}{\Gamma(t_f-\tau')} \right] e^{(\tau-\tau')-2\int_{\tau'}^\tau \frac{1}{\Gamma(t_f-\tau'')} d\tau''} d\tau',$$

1300 using that
 1301

$$1302 \frac{d}{d\tau'} \exp \left[-2 \int_{\tau'}^\tau \frac{1}{\Gamma(t_f-\tau'')} d\tau'' \right] = \frac{2}{\Gamma(t_f-\tau')} \exp \left[-2 \int_{\tau'}^\tau \frac{1}{\Gamma(t_f-\tau'')} d\tau'' \right],$$

1305 one finds that the mean of q for the evolution with $\omega = 0$, starting from any value $q(0)$ at any time
 1306 t_f , is
 1307

$$1308 q(\tau) = q(0) e^{\tau - 2 \int_0^\tau \frac{1}{\Gamma(t_f-\tau')} d\tau'} + \sqrt{d} e^{-(t_f-\tau)} \left(1 - \exp \left(-2 \int_0^\tau \frac{1}{\Gamma(t_f-\tau')} d\tau' \right) \right). \quad (25)$$

1311 Using
 1312

$$1313 \int_0^\tau \frac{1}{\Gamma(t_f-\tau')} d\tau' = -\frac{1}{2} \log \frac{e^{-2\tau} + (\sigma^2 - 1)e^{-2t_f}}{1 + (\sigma^2 - 1)e^{-2t_f}},$$

1314 we find that
 1315

$$1316 q(\tau) = q(0) e^\tau \frac{e^{-2\tau} + (\sigma^2 - 1)e^{-2t_f}}{1 + (\sigma^2 - 1)e^{-2t_f}} + \sqrt{d} e^{-(t_f-\tau)} \frac{1 - e^{-2\tau}}{1 + (\sigma^2 - 1)e^{-2t_f}}. \quad (26)$$

1317 One can check that, when $q(0)$ is obtained by the equilibrium process with $\omega = 0$, namely $q(0) = \sqrt{d}e^{-t_f}$, then at all times $q(\tau) = \sqrt{d}e^{-(t_f-\tau)}$.
 1318
 1319

1320 CASE: INTERRUPTED GUIDANCE
 1321

1322 Now let us consider a protocol of interrupted guidance. We start the backward process at $t_f \gg 1$
 1323 with a CFG coefficient $\omega > 0$. Then at time backward time τ_1 (forward time $t_1 = t_f - \tau_1$) we
 1324 switch to $\omega = 0$. At time t_1 the mean of q obtained from the backward process with $\omega > 0$ is larger
 1325 than the value $\sqrt{d}e^{-t_1}$ which would be obtained with the $\omega = 0$ dynamics (the reason is that the
 1326 extra force in (22) is positive). Let us write this mean as
 1327

$$1328 q(t_1, \omega) = \sqrt{d} e^{-t_1} + \delta q(t_1, \omega).$$

1329 Let us measure the backward time starting from $t = t_1$. We thus write $t = t_1 - \tilde{\tau}$. We can use
 1330 formula (26) with $t_f \rightarrow t_1$, $\tau \rightarrow \tilde{\tau}$ and $q(0) \rightarrow q(t_1, \omega)$. This gives for the mean value of q :
 1331

$$1332 \tilde{q}(\tilde{\tau}, \omega) = \sqrt{d} e^{-(t_1-\tilde{\tau})} + \delta q(t_1, \omega) \frac{e^{-\tilde{\tau}} + (\sigma^2 - 1)e^{\tilde{\tau}-2t_1}}{1 + (\sigma^2 - 1)e^{-2t_1}},$$

1334 which, translated in terms of the forward time $t = t_1 - \tilde{\tau}$, gives:
 1335

$$1336 q(t) = \sqrt{d} e^{-t} + \delta q(t_1, \omega) e^{t-t_1} \frac{1 + (\sigma^2 - 1)e^{-2t}}{1 + (\sigma^2 - 1)e^{-2t_1}}. \quad (27)$$

1338 In particular at the end of the backward process, for $\tilde{\tau} = t_1$ we get
 1339

$$1340 q(t=0) = \sqrt{d} + \delta q(t_1, \omega) e^{-t_1} \frac{\sigma^2}{1 + (\sigma^2 - 1)e^{-2t_1}}$$

1343 If we choose $t_1 = t_s = (1/2) \log d$, and assuming that the dynamics at $t > t_1$ has produced an
 1344 average $q(t_1) = \sqrt{d}e^{-t_1} + \delta q$, we find that
 1345

$$1346 q(t=0) = \sqrt{d} \left(1 + \delta q \frac{\sigma^2/d}{1 + (\sigma^2 - 1)/d} \right).$$

1348 This shows that the guidance interrupted at t_s gives a good result only in the limit $\sigma^2/d \ll 1$. Figs.
 1349 9 and 10 illustrate the effect of the choice of t_1 .
 1350

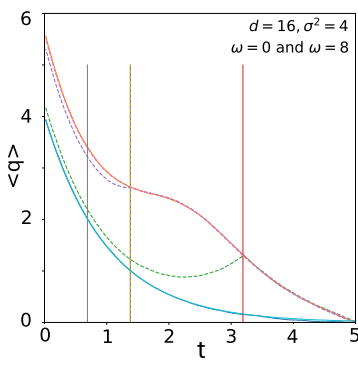


Figure 9: Mean value of q obtained from the backward diffusion in a Gaussian mixture model with $d = 16, \sigma^2 = 4$ (speciation time $t_s = 1.38$). The CFG is run with $\omega = 8$ from $t = 5$ to $t = t_1$, then one switches to the class guidance $\omega = 0$. The top curve is when CFG is kept all the time ($t_1 = 0$). The bottom curve is the case without CFG ($\omega = 0$). Three values of t_1 are studied $t_1 = 0.69, 1.38, 3.19$ (vertical lines). The dashed curves give the mean value of q for each of these three cases. They are in perfect agreement with the theoretical prediction (27).

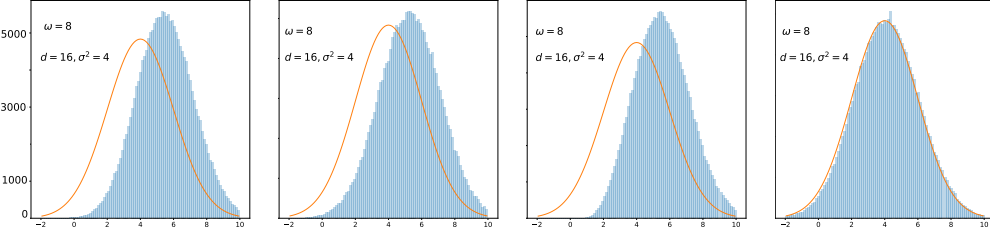


Figure 10: Histograms of $q(t = 0)$ obtained from the backward diffusion in a Gaussian mixture model with $d = 16, \sigma^2 = 4$ (the speciation time is 1.38), run with 200,000 trajectories. Left: CFG with $\omega = 8$ is applied at all times. The final distribution has a larger mean and a smaller variance than the desired class distribution (full line). Next three figures: The CFG is run with $\omega = 8$ from $t = 5$ to $t = t_1$, then one switches to standard CFG $\omega = 0$. From left to right, $t_1 = 0.69, 1.38, 3.19$. The mean values of q in the four cases are respectively 5.56, 5.51, 5.29, 4.12 and the standard deviations 1.68, 1.74, 1.87, 1.98, with targets $\mu = 4, \sigma = 2$. In order to minimize the bias due to CFG one must interrupt it before the speciation takes place in the background diffusion, hence at $t_1 > t_s$.

CFG CONTRIBUTION TO THE MAGNETIZATION IN REGIME I

Using Equation (14), one can derive the equation for the average $\langle q(\tau) \rangle_\omega$:

$$\begin{aligned} \frac{d\langle q(\tau) \rangle_\omega}{d\tau} &= \langle q(\tau) \rangle_\omega \left(1 - \frac{2}{\Gamma(t_f - \tau)} \right) + \frac{2\sqrt{d}}{\Gamma(t_f - \tau)} e^{-(t_f - \tau)} \\ &\quad + 2\omega\sqrt{d} \frac{e^{-(t_f - \tau)}}{\Gamma(t_f - \tau)} \left\langle 1 - \tanh \left(\frac{q\sqrt{d}e^{-(t_f - \tau)}}{\Gamma(t_f - \tau)} \right) \right\rangle_\omega. \end{aligned} \quad (28)$$

The extra ω term is strictly positive. Therefore, we have:

$$\langle q(\tau) \rangle_\omega \geq \langle q(\tau) \rangle_{\omega=0}, \quad \forall \tau.$$

Moreover, using that the right-hand side is less than or equal to:

1404

$$\langle q(\tau) \rangle_\omega \left(1 - \frac{2}{\Gamma(t_f - \tau)} \right) + \frac{2(1 + \omega)\sqrt{d}}{\Gamma(t_f - \tau)} e^{-(t_f - \tau)},$$

1405

1406 which corresponds to the backward equation one would obtain if $\|\vec{m}\|^2 = (1 + \omega)d$. We then find:

1407

$$\langle q(\tau) \rangle_{\omega=0} < \langle q(\tau) \rangle_\omega < \sqrt{d}e^{-t}(1 + \omega).$$

1408

1409 We conclude that $\langle q(\tau) \rangle_\omega$ gets an extra contribution due to CFG of the order $\sqrt{d}e^{-t}$.

1410

1411 CFG indeed shifts the mean value. The amount of shift is of order $\sqrt{d}e^{-t}$ in Regime I. However, as
1412 we shall see next the CFG has almost no effect in Regime II, so we can use the result of the previous
1413 section to argue that the total shift due to CFG is the one of CFG in Regime I followed by a switch
1414 at $\omega = 0$ in Regime II, i.e., it is of order one.

1415

1416 CFG CONTRIBUTION TO THE SCORE IN REGIME I VS IN REGIME II

1417

1418 Another interesting inequality can be derived for the difference between the CFG and the standard,
1419 non-guided score, $S_{\text{CFG}} - S_C$, evaluated on trajectories corresponding to CFG:

1420

1421

1422

1423

1424

1425

1426

1427

1428

1429

1430

1431

1432

1433

1434

1435

1436

1437

1438

1439

1440

1441

1442

1443

1444

1445

1446

1447

1448

1449

1450

1451

1452

1453

1454

1455

1456

1457

CFG CONTRIBUTION TO THE SCORE IN REGIME I VS IN REGIME II

Another interesting inequality can be derived for the difference between the CFG and the standard, non-guided score, $S_{\text{CFG}} - S_C$, evaluated on trajectories corresponding to CFG:

$$S_{\text{CFG}} - S_C = \omega \frac{\sqrt{d}e^{-(t_f - \tau)}}{\Gamma(t_f - \tau)} \left(1 - \tanh \left(\frac{q\sqrt{d}e^{-(t_f - \tau)}}{\Gamma(t_f - \tau)} \right) \right). \quad (29)$$

We use the fact that for the same thermal noise, we have $q_\omega(\tau) \geq q_{\omega=0}(\tau)$ because the CFG force is always equal or larger than the $\omega = 0$ one. Therefore for a given (the same) thermal history we have:

$$- \tanh \left(\frac{q_\omega(\tau)\sqrt{d}e^{-(t_f - \tau)}}{\Gamma(t_f - \tau)} \right) \leq - \tanh \left(\frac{q_{\omega=0}(\tau)\sqrt{d}e^{-(t_f - \tau)}}{\Gamma(t_f - \tau)} \right), \quad (30)$$

and we can obtain:

$$S_{\text{CFG}} - S_C \leq \frac{\sqrt{d}e^{-(t_f - \tau)}}{\Gamma(t_f - \tau)} \left(1 - \tanh \left(\frac{q_{\omega=0}(\tau)\sqrt{d}e^{-(t_f - \tau)}}{\Gamma(t_f - \tau)} \right) \right). \quad (31)$$

This inequality tells us, as expected, that the extra CFG contribution to the score is very small at the beginning of the backward process. Its mean increases, and is of the order of one during the backward process in Regime I. However, after the speciation time $q_{\omega=0}(\tau)$ is a Gaussian variable with a mean $\sqrt{d}e^{-(t_f - \tau)}$ much larger than the square root of the variance. Therefore, replacing the fluctuating variable by its mean we obtain

$$S_{\text{CFG}} - S_C \leq \frac{\sqrt{d}e^{-(t_f - \tau)}}{\Gamma(t_f - \tau)} \left(1 - \tanh \left(\frac{de^{-2(t_f - \tau)}}{\Gamma(t_f - \tau)} \right) \right). \quad (32)$$

In Regime II, $t_f - \tau$ is of order one, and using the asymptotic form of the hyperbolic tangent one finds that

$$S_{\text{CFG}} - S_C \leq \frac{\sqrt{d}e^{-(t_f - \tau)}}{\Gamma(t_f - \tau)} \exp \left(-2 \frac{de^{-2(t_f - \tau)}}{\Gamma(t_f - \tau)} \right). \quad (33)$$

Therefore in Regime II the extra contribution to the score is exponentially small in d and its effect is completely negligible with respect to the one in Regime I.

1458 ANALYSIS OF THE CFG EFFECT ON THE VARIANCE

1459

1460 Let us derive the equation for $\langle q^2(\tau) \rangle_\omega - \langle q(\tau) \rangle_\omega^2$.

1461

1462 Using Itô calculus, we have (multiplying by $q(\tau)$ in the equation for $\frac{dq(\tau)}{d\tau}$):

1463

$$\begin{aligned}
 \frac{dq^2(\tau)}{d\tau} &= 2 + 2q^2(\tau) \left(1 - \frac{2}{\Gamma(t_f - \tau)} \right) + 2q(\tau) \frac{2\sqrt{d}}{\Gamma(t_f - \tau)} e^{-(t_f - \tau)} \\
 &\quad + 2 \frac{2\omega\sqrt{d}}{\Gamma(t_f - \tau)} e^{-(t_f - \tau)} \left(q(\tau) - q(\tau) \tanh \left(\frac{q(\tau)\sqrt{d}e^{-(t_f - \tau)}}{\Gamma(t_f - \tau)} \right) \right) \\
 &\quad + 2q(\tau)\eta(\tau).
 \end{aligned} \tag{34}$$

1470

1471

1472 Taking the average and subtracting $2\langle q(\tau) \rangle_\omega \frac{d\langle q(\tau) \rangle_\omega}{d\tau}$, we find the equation for $\langle q^2(\tau) \rangle_\omega - \langle q(\tau) \rangle_\omega^2$:

1473

$$\begin{aligned}
 \frac{d\langle q^2(\tau) \rangle_\omega - \langle q(\tau) \rangle_\omega^2}{d\tau} &= 2 + 2 \left(\langle q^2(\tau) \rangle_\omega - \langle q(\tau) \rangle_\omega^2 \right) \left(1 - \frac{2}{\Gamma(t_f - \tau)} \right) \\
 &\quad + \omega \frac{4\sqrt{d}e^{-(t_f - \tau)}}{\Gamma(t_f - \tau)} \left(\langle q(\tau) \rangle_\omega \left\langle \tanh \left(\frac{q\sqrt{d}e^{-(t_f - \tau)}}{\Gamma(t_f - \tau)} \right) \right\rangle_\omega \right. \\
 &\quad \left. - \langle q(\tau) \tanh \left(\frac{q\sqrt{d}e^{-(t_f - \tau)}}{\Gamma(t_f - \tau)} \right) \rangle_\omega \right).
 \end{aligned} \tag{35}$$

1484

1485 At the beginning of the backward process, one can expand $\tanh(x)$ and observe that the term in the
1486 parentheses is proportional to:

1487

1488
$$- \left(\langle q(\tau)^2 \rangle_\omega - \langle q(\tau) \rangle_\omega^2 \right), \tag{36}$$

1489

1490 which is negative. Therefore, we can conclude that the classifier-free-guidance-added term will
1491 result in shrinkage of the variance.1492 As for the mean, the main CFG effect on the variance is produced in Regime I, since the CFG score
1493 term is exponentially small in Regime II.

1494

1495

E EFFECT OF NONLINEAR CLASSIFIER-FREE GUIDANCE IN FINITE
1496 DIMENSIONS

1497

1498

E.1 NONLINEAR CFG ALONG M

1499

1500

Recall the useful quantities:

1501

1502

1503

$$\theta \equiv \frac{\vec{x} \cdot \vec{m} e^{-t}}{\Gamma_t}, \quad \hat{\vec{m}} \equiv \frac{\vec{m}}{\|\vec{m}\|}. \tag{37}$$

1504

1505

From Eqs. equation 11-equation 12, the score difference is aligned with \vec{m} :

1506

1507

$$\vec{S}_t(\vec{x}, c) - \vec{S}_t(\vec{x}) = \frac{\|\vec{m}\| e^{-t}}{\Gamma_t} (c - \tanh \theta) \hat{\vec{m}}. \tag{38}$$

1508

1509

1510

Denote $A \equiv \frac{\|\vec{m}\| e^{-t}}{\Gamma_t} (c - \tanh \theta)$, so that $\vec{S}_t(\vec{x}, c) - \vec{S}_t(\vec{x}) = A \hat{\vec{m}}$. With the power-law guidance
 $\phi_t(s) = \omega s^\alpha$, the nonlinear CFG score reads

1511

$$\vec{S}_t^{\text{PL}}(\vec{x}, c) = \vec{S}_t(\vec{x}, c) + \omega (\vec{S}_t(\vec{x}, c) - \vec{S}_t(\vec{x})) |\vec{S}_t(\vec{x}, c) - \vec{S}_t(\vec{x})|^\alpha, \tag{39}$$

1512 Hence the projection onto $\hat{\vec{m}}$ becomes
 1513

$$\vec{S}_t^{\text{PL}}(\vec{x}, c) \cdot \hat{\vec{m}} = \vec{S}_t(\vec{x}, c) \cdot \hat{\vec{m}} + \omega A |A|^\alpha \quad (40)$$

$$= -\frac{\vec{x} \cdot \hat{\vec{m}}}{\Gamma_t} + \frac{\|\vec{m}\| e^{-t}}{\Gamma_t} c + \omega \left(\frac{\|\vec{m}\| e^{-t}}{\Gamma_t} \right)^{1+\alpha} (c - \tanh \theta) |c - \tanh \theta|^\alpha. \quad (41)$$

1519 Therefore, the SDE for q becomes with $\|\vec{m}\| = d$ and selecting $c = +1$:
 1520

$$\frac{dq}{d\tau} = q \left(1 - \frac{2}{\Gamma} \right) + \frac{2d}{\Gamma} e^{-(t_f - \tau)} + 2\omega \frac{d^{1+\alpha}}{2^{1+\alpha}} \left(\frac{1}{\Gamma} e^{-(t_f - \tau)} \right)^{1+\alpha} (1 - \tanh(\beta q))^{1+\alpha} + \eta(\tau). \quad (42)$$

1525 Again, setting $\alpha = 0$ recovers the earlier linear-CFG equation (Eq. 22) exactly.
 1526

1528 NONLINEAR VS LINEAR EXTRA-DRIFT

1529 We use the same notation as before. Define
 1530

$$u(q) = 1 - \tanh(\beta q), \quad \beta = \frac{1}{\Gamma} d e^{-(t_f - \tau)}.$$

1533 (Note that for the “ $+\vec{m}$ ” class one has $u(q) > 0$, hence $u|u|^\alpha = u^{1+\alpha}$.)
 1534

1535 The nonlinear extra drift (coming from the power-law CFG, for the $+\vec{m}$ class) is

$$\Delta F(q) = 2\omega \frac{d^{1+\alpha}}{2^{1+\alpha}} \left(\frac{1}{\Gamma} e^{-(t_f - \tau)} \right)^{1+\alpha} u(q)^{1+\alpha},$$

1539 while the linear-CFG ($\alpha = 0$) extra drift is
 1540

$$\Delta F_0(q) = 2\omega \frac{d}{2\Gamma} e^{-(t_f - \tau)} u(q).$$

1543 Therefore we look at the following identity:
 1544

1545 Pointwise ratio (nonlinear / linear):

$$\frac{\Delta F(q)}{\Delta F_0(q)} = \left[\underbrace{\frac{d e^{-(t_f - \tau)}}{\Gamma} u(q)}_{=: B(q)} \right]^\alpha = B(q)^\alpha, \quad B(q) := \frac{d e^{-(t_f - \tau)}}{\Gamma} u(q).$$

1550 Hence whether the nonlinear guidance amplifies (ratio > 1) or suppresses (ratio < 1) the linear-CFG
 1551 push at a given q depends only on the sign of α and whether the base $B(q)$ is greater or smaller than
 1552 1:
 1553

- 1554 • If $B(q) > 1$: $\alpha > 0$ amplifies the push, $\alpha < 0$ suppresses it.
- 1555 • If $B(q) < 1$: $\alpha > 0$ suppresses the push, $\alpha < 0$ amplifies it.

1557 **Hessian / curvature effect.** Recall that the drift (deterministic part) is written $F(q, \tau)$ and the
 1558 potential V satisfies $F = -\partial_q V$. The curvature (Hessian) is $\partial_q^2 V = -\partial_q F$. The nonlinear term
 1559 contributes an extra piece to $\partial_q F$ through the q -derivative of $u^{1+\alpha}$. Since $u(q) > 0$ we have

$$\frac{d}{dq} [u(q)^{1+\alpha}] = (1 + \alpha) u(q)^\alpha u'(q).$$

1563 Using $u'(q) = -\beta \operatorname{sech}^2(\beta q)$ we obtain
 1564

$$\frac{d}{dq} [u(q)^{1+\alpha}] = -(1 + \alpha) \beta \operatorname{sech}^2(\beta q) u(q)^\alpha.$$

1566 Therefore the additional contribution to $\partial_q F$ coming from the nonlinear term is (up to the multi-
 1567 plicative prefactors shown above)

$$1569 \Delta(\partial_q F) = -2\omega \frac{d}{1+\alpha} \left(\frac{1}{\Gamma} e^{-(t_f - \tau)} \right)^{1+\alpha} (1+\alpha) \beta \operatorname{sech}^2(\beta q) u(q)^\alpha,$$

1571 which simplifies to

$$1573 \Delta(\partial_q F) = -2\omega d \left(\frac{1}{\Gamma} e^{-(t_f - \tau)} \right)^{1+\alpha} \beta \operatorname{sech}^2(\beta q) u(q)^\alpha.$$

1575 Since $\partial_q^2 V = -\partial_q F$, the corresponding increment in curvature is

$$1577 \Delta(\partial_q^2 V) = +2\omega (1+\alpha) \frac{d}{1+\alpha} \left(\frac{1}{\Gamma} e^{-(t_f - \tau)} \right)^{1+\alpha} \beta \operatorname{sech}^2(\beta q) u(q)^\alpha,$$

1578 or, more compactly (omitting positive constants),

$$1580 \Delta(\partial_q^2 V) \propto d \left(\frac{1}{\Gamma} e^{-(t_f - \tau)} \right)^{1+\alpha} \beta \operatorname{sech}^2(\beta q) u(q)^\alpha.$$

1582 **Comparison with the linear ($\alpha = 0$) curvature increment.** The ratio of nonlinear vs linear
 1583 curvature increments is essentially

$$1585 \frac{\Delta(\partial_q^2 V)_\alpha}{\Delta(\partial_q^2 V)_0} \approx B(q)^\alpha,$$

1588 so (for the same reasons as for the drift) whether the nonlinear term *increases* or *decreases* the
 1589 curvature relative to $\alpha = 0$ depends on the sign of α and on whether $B(q) > 1$ or $B(q) < 1$:

- 1590 • If $B(q) > 1$: $\alpha > 0$ amplifies the curvature increase, $\alpha < 0$ reduces it.
- 1591 • If $B(q) < 1$: $\alpha > 0$ reduces the curvature increase, $\alpha < 0$ amplifies it.

1593 SELECTING α IN THE NONLINEAR CFG SCHEME

1595 Consider the projected SDE for the component $q = \vec{x} \cdot \vec{m} / \sqrt{d}$ under the nonlinear power-law CFG
 1596 scheme equation 42. We claim that, given a fixed dimension d , mean vector \vec{m} , variance σ^2 , and
 1597 a linear CFG scheme with weight ω , one can always construct a simple nonlinear alternative with
 1598 $\alpha \in \{\alpha', 0\}$, where $\alpha' > -1$. We first develop the argument for $\alpha' > 0$. The reasoning extends
 1599 directly to $-1 < \alpha' < 0$, with the roles of the cases $B(q) < 1$ and $B(q) > 1$ reversed. The essential
 1600 conclusion is that, in very low dimensions, effective use of nonlinear CFG requires avoiding an
 1601 overly strong push, even in the correct direction, since the system is unstable and highly sensitive.
 1602 For case $\alpha' > 0$ our claims are as follows:

- 1603 1. The nonlinear term either suppresses the mean push along the conditioning direction (when
 1604 the score difference is small, $B(q) < 1$) or preserves it (when the score difference is large,
 1605 $B(q) > 1$).
- 1606 2. The confinement of the effective potential is either reduced (when the score difference is
 1607 small, $B(q) < 1$) or kept the same relative to the linear CFG case (when the score difference
 1608 is large, $B(q) > 1$).

1609 Recall that

$$1611 B(q) = \frac{\|\vec{m}\| e^{-t}}{\Gamma_t} (1 - \tanh \Theta), \quad \Theta = \frac{\vec{x} \cdot \vec{m} e^{-t}}{\Gamma_t},$$

1613 which quantifies the conditional–unconditional score difference projected along \vec{m} .

1614 In small dimensions, the generative dynamics of diffusion or flow-matching are highly sensitive
 1615 to large guidance weights ω when $\alpha = 0$. In this regime, the system is not “self-correcting” via
 1616 high-dimensional averaging, so a large push along \vec{m} can cause overshooting or instability.

1617 - When $B(q) > 1$, the score difference $\Delta S = S_t(\vec{x}, c) - S_t(\vec{x})$ is already large, meaning that the
 1618 conditional signal is strong. In this case, setting $\alpha = 0$ preserves the linear push exactly, ensuring
 1619 that the system is guided correctly without amplification. Choosing $\alpha > 0$ here would amplify the
 already strong signal, risking overshoot.

1620 - When $B(q) < 1$, the score difference is small, and the conditional signal is weak. Setting $\alpha = \alpha' >$
 1621 *dampens* the nonlinear CFG term, preventing small and unreliable differences from producing
 1622 disproportionate guidance. The nonlinear term is therefore suppressed where it is least reliable, and
 1623 preserved where the signal is sufficiently strong but not too large.

1624 Thus, by selecting $\alpha = \alpha'$ for $B(q) < 1$ and $\alpha = 0$ otherwise, the dynamics retain a stable,
 1625 interpretable push along \vec{m} , while ensuring that curvature is never increased beyond that of the linear
 1626 CFG case. In low dimensions, this prevents both over-confinement of the potential and excessive
 1627 push, providing a natural safeguard against instability.

1629 **Existence of regimes with $B(q) < 1$.** The base factor introduced above was

$$1630 \quad B(q) = \frac{d e^{-(t_f - \tau)}}{\Gamma} u(q), \quad u(q) = 1 - \tanh(\beta q), \quad \Gamma = \Gamma_{t_f - \tau}.$$

1633 Two simple observations guarantee that the nonlinear scheme will *sometimes* suppress the linear-
 1634 CFG effects (i.e. produce $B(q) < 1$) and therefore provide a benefit relative to standard CFG.

1635 First, in the long-time limit $t \equiv t_f - \tau \rightarrow \infty$ we have $e^{-t} \rightarrow 0$ and $\Gamma \rightarrow 1$, hence

$$1636 \quad \lim_{t \rightarrow \infty} B(q) = 0 < 1,$$

1638 for every fixed q . Thus there always exist times during the backward process where $B(q) < 1$ and
 1639 the nonlinear scheme suppresses the linear-CFG push and curvature increase.

1640 Second, at the other endpoint $t = 0$ (the earliest time in the backward process) one has $\Gamma(0) =$
 1641 $1 + (\sigma^2 - 1)e^{-0.2} = \sigma^2$, so

$$1643 \quad B(q)|_{t=0} = \frac{d}{\sigma^2} u(q) \leq \frac{2d}{\sigma^2}.$$

1644 Consequently, in very small dimension, if the problem parameters satisfy the condition

$$1646 \quad \frac{2d}{\sigma^2} < 1 \implies B(q)|_{t=0} < 1 \text{ for all } q,$$

1648 then $B(q) < 1$ already at $t = 0$ (and hence in a neighbourhood of $t = 0$). Even when $2d/\sigma^2 \geq 1$, the
 1649 inequality $B(q) < 1$ may still hold for most q if $u(q)$ is typically small (i.e. when $\tanh(\beta q) \approx 1$).

1650 Combining these remarks we conclude:

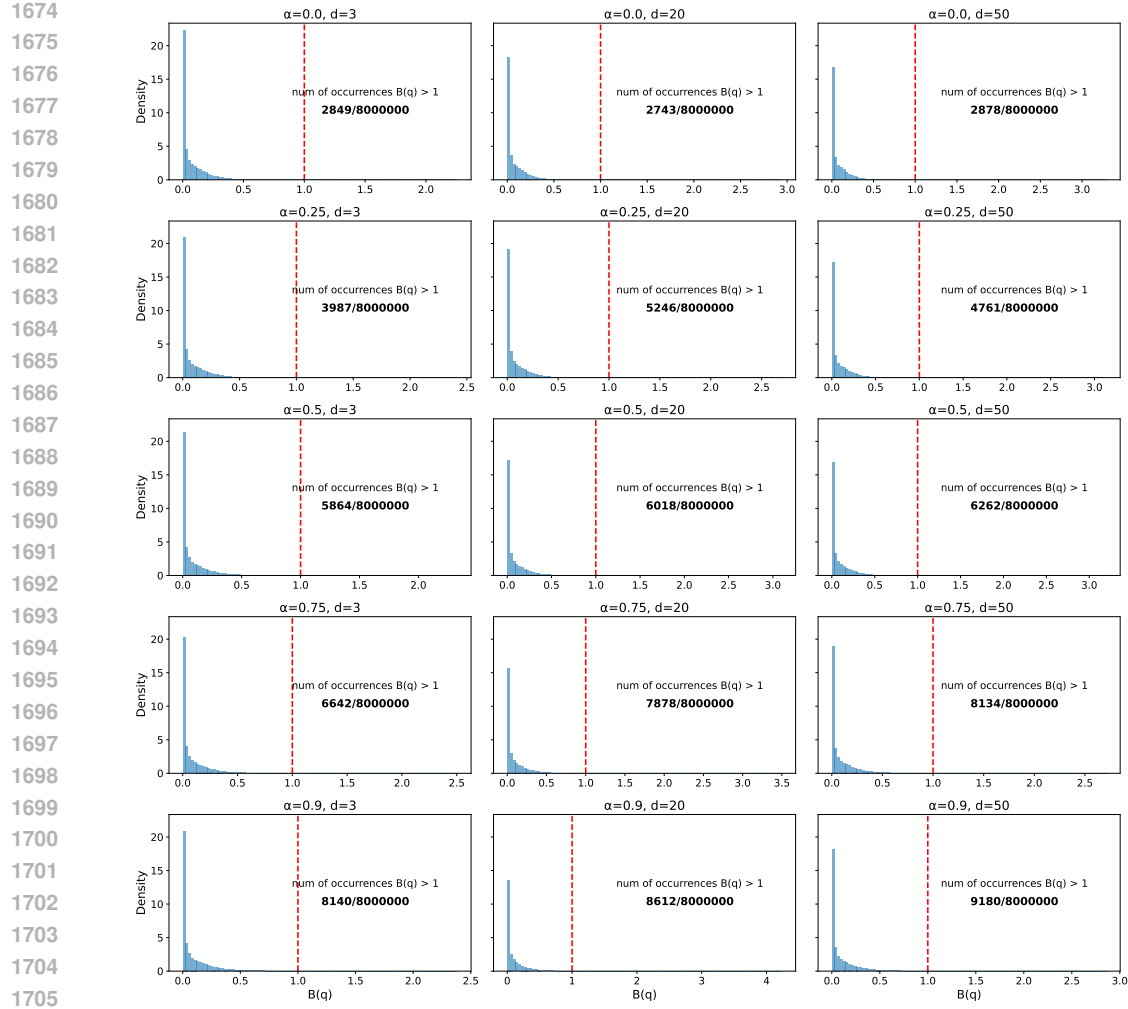
- 1652 • There always exist times (in particular sufficiently large t) for which $B(q) < 1$, so the
 1653 nonlinear scheme will suppress linear-CFG effects at those times.
- 1654 • For small d or sufficiently large noise variance σ^2 (more precisely when $2d/\sigma^2 < 1$), one
 1655 also has $B(q) < 1$ near $t = 0$ for all q , so the nonlinear scheme suppresses CFG uniformly
 1656 at early times as well.
- 1657 • In practice, therefore, the nonlinear power-law CFG will often reduce the unwanted CFG
 1658 side-effects (mean overshoot and excessive confinement) across substantial portions of the
 1659 trajectory; this is the regime exploited in our experiments.

1660 This means that the proposed simple nonlinear version of the CFG will always be more beneficial
 1661 than standard CFG by reducing its unwanted effects. We now proceed to argue about the frequency
 1663 of the event $B(q) > 1$.

1664 In practice, we found that setting $\alpha > 0$ throughout generation performed well, without explicitly
 1665 disabling nonlinear guidance when $B(q) > 1$. For simplicity, we adopted this approach across all
 1666 our experiments. In Fig. 11, we show specifically that for a wide range of data parameters, numer-
 1667 ical simulations indicate that the event $B(q) > 1$ happens very rarely. Nonetheless, we anticipate
 1668 that adaptively switching may provide further improvements in very low-dimensional settings, with
 1669 minor gains in higher dimensions.

1670 F EXPERIMENTAL DETAILS: GAUSSIAN MIXTURES

1671 In this section, we present experimental details for the numerical simulations involving Gaussian
 1673 mixtures, describing the procedures and the hyperparameter configurations.



1728 **G EXPERIMENTAL DETAILS: REAL-WORLD ANALYSES**
17291730 **G.1 ASSETS**
17311732 In Table 2 we list the datasets and models used in our work along with their licensing.
17331734 **Table 2: Assets used for our work.**

Name	License/Link
COCO’14	https://www.cocodataset.org
ImageNet	https://www.image-net.org
CC12M	https://github.com/google-research-datasets/conceptual-12m
YFCC100M	https://www.multimediacommons.org
Florence-2	https://huggingface.co/microsoft/Florence-2-large/blob/main/LICENSE
DiT	https://github.com/facebookresearch/DiT/blob/main/LICENSE.txt
EDM2	https://github.com/NVlabs/edm2/blob/main/LICENSE.txt
MMDiT	https://github.com/lucidrains/mmdit/blob/main/LICENSE
MDTv2	https://github.com/sail-sg/MDT/blob/main/LICENSE

1744 **G.2 PERFORMING THE TIME REPARAMETERIZATION**
17451746 In the second part of the paper, we evaluate the score of DiT models, in discrete time, as introduced by [Peebles & Xie \(2023\)](#). In this context, the forward process has a linear variance schedule
1747 $\{\beta_t\}_{t'=1}^L$, where L is the time horizon given as a number of steps. Here, the variance evolves lin-
1748 early from $\beta_1 = 10^{-4}$ to $\beta_{1000} = 2 \times 10^{-2}$. An unguided sample, at timestep t' , denoted $\vec{x}(t')$ can
1749 be expressed readily from its initial state, $\vec{x}(0) = \vec{a}$, as
1750

1751
$$\vec{x}(t') = \sqrt{\bar{\alpha}(t')} \vec{a} + \sqrt{1 - \bar{\alpha}(t')} \vec{\xi}(t')$$

1752 where $\bar{\alpha}(t') = \prod_{s=1}^{t'} (1 - \beta_s)$ and $\vec{\xi}$ is standard Gaussian noise. This equation corresponds to the
1753 discretization of the Ornstein-Uhlenbeck Eq. (9) under the following timestep t' reparameterization,
1754

1755
$$t = -\frac{1}{2} \log(\bar{\alpha}(t')) ,$$

1756 where time t is as defined in the main manuscript. This gives the map between our theoretical
1757 timescale used in Gaussian mixtures, and the one used in real-world settings. We note that, as the
1758 neural network predicts the noise, in order to calculate the score, one needs to normalize the output
1759 by the standard deviation (depending on the variance schedule). In this case, this corresponds to
1760 dividing the neural network output by $\sigma(t') = \sqrt{1 - \bar{\alpha}(t')}$. **In numerical experiments, we divide**
1761 **the CFG-added-term** by $\sigma(t') + 1$ to avoid numerical errors. This is theoretically justified due to
1762 the fact that, as discussed in main paper, the score difference $|S_{t'}(\vec{x}, c) - S_{t'}(\vec{x})|$ for large forward
1763 times decays exponentially (as $e^{-t'}$) to zero.
17641765 For completeness, we present the full comparison of numerical simulations to real-world using
1766 the time-reparameterization to plot the timesteps on the same time-scale. Our findings are por-
1767 trayed in Figure 12. As each framework uses a separate time reparameterization, the x-axis
1768 needs to be recalculated accordingly. For the EDM2 framework ([Karras et al., 2022](#)), this can
1769 be done as follows: given a noise schedule $\sigma(t)$, the reparameterization can be calculated as
1770 $t'(t) = (1/2) \log(1 + \sigma^2(t))$, assuming that $s(t) = 1$. For the case $s(t)$, one needs to resort to
1771 equation Eq. (2).
17721773 **G.2.1 APPLYING THE FORMULA TO VELOCITY FLOW-MATCHING.**
17741775 For velocity-based flow models ([Achilli et al., 2025](#)) it follows that: $\tilde{u}_t(x|y) = u_t(x|y) +$
1776 $\omega[u_t(x|y) - u_t(x)]$ and from their Lemma 1, $u_t(x|y) + b_t \nabla \log p_t(x|y)$. This implies that
1777 $|u_t(x|y) - u_t(x)|^\alpha = b_t^\alpha |\nabla \log p_t(x|y) - \nabla \log p_t(x)|^\alpha$. In the case of straight paths, where
1778 $\alpha_t = \tan \sigma_t = 1 - t$ (as used in our experiments), $b_t^\alpha = (\frac{1-t}{t})^\alpha$. Therefore, Power-Law CFG
1779 with $\phi_t(s) = \omega s^\alpha$ does indeed correspond to scaling the velocity difference according to the afore-
1780 mentioned equations. However, since the score difference $\delta S_t = |\nabla \log p_t(x|y) - \nabla \log p_t(x)|$
1781

1782 decays exponentially, both approaches - simply exponentiating v^α and scaling the velocity difference
 1783 to determine the score- satisfy the nonlinear guidance condition $\lim_{s \rightarrow 0} s\phi_t(s) = 0$. Directly
 1784 exponentiating v^α corresponds to the choice $\phi_t(s) = \omega b_t^\alpha s^\alpha$. In our experiments, to stay consistent
 1785 with the definition of Power-Law CFG where $\phi_t(s) = \omega s^\alpha$, we scaled the velocity difference ac-
 1786 cording to formulas above. We also examined directly exponentiating v^α : although it did improve
 1787 over standard CFG, it underperformed compared to Power-Law CFG.

1788 G.3 HYPERPARAMETER CONFIGURATIONS

1790 Here, we give exact hyperparameters used for reproducing all our experiments. The real-world
 1791 experiments are performed using NVIDIA H100 Tensor Core - 80GB HBM3. The EDM2-S model
 1792 has a model size of 280 Mparams and 102 Gflops, whereas the DiT-XL/2 model has model size of
 1793 675 Mparams and 525 Gflops. Parameter α is tuned in $(0.3, 0.95)$ with an increment of 0.05 and
 1794 parameter ω is tuned in $(1., 12.)$ with an increment of 0.05. To tune ω , we first perform a small grid
 1795 search of the increment of 1. and then do a further extensive search of the best performing ω_{prelim}
 1796 in the range $(\omega_{prelim} - 2., \omega_{prelim} + 2.)$ with the 0.05 increment. We begin with the hyperparameters
 1797 used in our figures.

1798 In **Figure 1**⁴, we plot the generation of images starting from 7 initial seeds for the DiT/XL-2 model
 1799 trained on ImageNet-1K (256×256) for (1) conditional model without using guidance, (2) standard
 1800 CFG with $\omega = 4.$, and Power-Law CFG with $\alpha = 0.9, \omega = 8.$

1801 In **Figure 2**, the plots correspond to the histograms of the samples generated using the backward
 1802 process with dimensions $d \in \{200, 5, 5\}$ and guidance parameter $\omega \in \{0, 0.2, 15\}$, with $\sigma^2 = 1$,
 1803 averaged over 10,000 trajectories. The non-linear parameter has $\alpha = 10.$

1804 In **Figure 4**, we use 20-dimensional Gaussian simulation with $\sigma^2 = 1$ and vary the nonlinear param-
 1805 eter as shown in the legend. For the real-world experiments we use the Class-conditional EDM2-S
 1806 trained on ImageNet-1K 256x256 and an in-house text-to-image model with MMDiT architecture.

1807 In **Figure 5**, we perform sensitivity analysis for EDM2-S trained on ImageNet-1K (512×512),
 1808 taking α from 0. to 0.99 with 20 evenly spaced values, and ω from 1. to 10. with 20 evenly spaced
 1809 values as well. The right plot involves α values of 0.2, 0.4, 0.6, 0.8, 0.9 with ω in the range of 1. to
 1810 12.5 with evenly spaced 20 points.

1811 In **Figure 6** we show generations of DiT/XL-2 trained on ImageNet-1K (256×256). The red panel
 1812 contains generations from weak and strong standard CFG (corresponding to $\omega = 2.$ and $\omega = 5.$
 1813 respectively). The green panel corresponds to power-law CFG ($\alpha = 0.9$) with weak and strong
 1814 guidance (corresponding to $\omega = 2.$ and $\omega = 10.$). The blue panel corresponds to combinations of α
 1815 and ω $(0, 2.5), (0.25, 4.), (0.5, 6.)$ and $(0.9, 8.).$

1816 In **Figure 3**, we plot the evolution of the 1D backward dynamics with means at ± 4 and unit variance.
 1817 The potential plotted corresponds to equation $V(q, t) = \frac{1}{2}q^2 - 2 \log \cosh(qe^{-(t-t_s)})$. For the
 1818 derivation of this potential, see Appendix B.2 in [Biroli et al. \(2024\)](#).

1819 In **Figure 7**, we examine the following functions:

$$1820 V_{\text{class}}(q, t; c) = \frac{1}{2}q^2 - ce^{-(t-t_s)}q + 2$$

$$1821 V_{\text{extra}}(q, t; c) = -ce^{-(t-t_s)}q + \log \left(\cosh \left(qe^{-(t-t_s)} \right) \right) + \log(2),$$

1822 where the plots correspond to V_{class} , V_{extra} and $(V_{\text{class}} + \omega V_{\text{extra}})$ with $\omega = 3$ respectively. We select
 1823 $c = 1$, and fix the speciation time to $t_s = .5$. The additive constants are added for clarity only.

1824 In **Figure 8**, the first two plots correspond to the histograms of the samples generated using the
 1825 backward process with dimensions $d \in \{2, 200\}$ and guidance parameter $\omega \in \{0, 0.2, 15\}$, with
 1826 $\sigma^2 = 1$, averaged over 10,000 trajectories. The last two plots correspond to the actual trajectories
 1827 projected onto the target mean $+\bar{m}$ for values of $\omega \in \{0., 5., 10., 15., 20.\}$.

1828 ⁴We expect that the images of bees on yellow flowers correspond to a high-likelihood mode of the bee
 1829 class distribution. A similar trend appears for jellyfish, where stronger guidance produces images with more
 1830 extensive blue backgrounds (Figure 6, left panel). This likely reflects stronger guidance pushing samples toward
 1831 higher-likelihood regions—a connection also noted in the Autoguidance paper [[Karras et al., 2024a](#), Sec. 3],
 1832 linking optimal score matching to ML estimation.

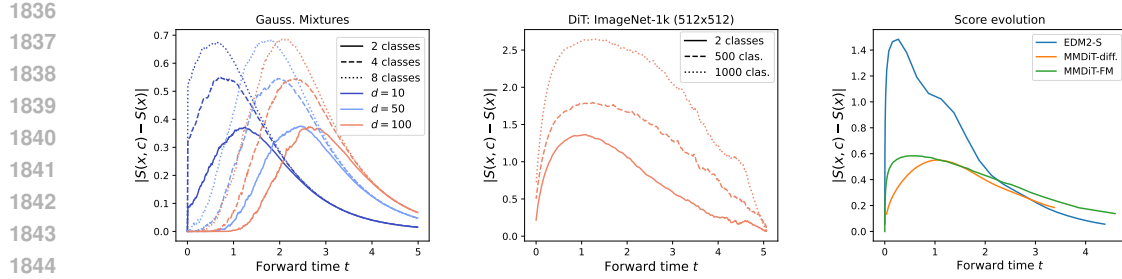


Figure 12: **Evolution of the score differences for numerical simulations and real-world experiments** projected onto the same time-scale for direct comparison. **First:** Numerically simulating mixture of two, four, and eight Gaussians with equidistant means on a sphere ($r = \sqrt{d}$), with varying dimension d , with $\omega = 4$, $\sigma^2 = 1$, averaged over 10,000 trajectories. As d increases, the score difference starts to increase at an earlier backward time τ . Additionally, as the number of classes increases, the magnitude of the score difference grows, as well as the duration of large difference between the scores. **Second:** Three DiT/XL-2 models trained on ImageNet-1K using 2, 500, and 1000 classes (image size 512×512). We observe a similar pattern: as d increases, the score difference becomes larger at an earlier time. Furthermore, as the number of classes increases, the magnitude of the score difference increases, together with the duration for which the difference remains large. **Third:** evolution of the remaining models used in our experiments (EDM2-S, MMDiT and MDTv2). We observe a similar behavior to theory and the DiT/XL-2 models.

Table 3: Hyperparameter configurations used throughout the experiments.

(α, ω)	DiT/XL-2	EDM2-S	Diff. MMDiT CC12m	Diff. MDTv2 IMN-1K	FM MMDiT COCO	FM MMDiT CC12M
Standard	(0., 1.5)	(0., 1.4)	(0., 1.55)	(0., 1, 2)	(0., 2.)	(0., 2.1)
Non-linear	(0.75, 4.85)	(0.85, 11.4)	(0.6, 7.0)	(0.8, 8.5)	(0.7, 10.15)	(0.6, 8.05)
Non-lin. + Limited	(0.8, 4.95)	(0.9, 12.05)	(0.55, 8.25)	(0.85, 8.25)	(0.75, 10.05)	(0.65, 7.85)
Non-lin. + CADS	(0.7, 4.75)	(0.80, 11.75)	(0.75, 8.15)	(0.80, 8.40)	(0.75, 10.75)	(0.55, 7.90)

In Figure 9, we plot the backward diffusion in a Gaussian mixture model with $d = 16$, $\sigma^2 = 4$, $\omega = 8$. The CFG is either run at all times (top curve), stopped at times t_1 or not used at all (bottom curve).

In Figure 10, we perform linear CFG with $\omega = 8$ from $t = 5$ to $t = t_1$, after which we turn CFG off ($\omega = 0$) at times $t_1 = 0.69, 1.38, 3.19$.

In Figure 12, we use DiT/XL-2 model trained on 2, 500 and 1000 classes. For 2 classes, we have selected the same classes as in Biroli et al. (2024), and for the 500 classes we selected the first 500 classes in ImageNet-1K. The x-axis represents the Forward time t , where the parameterization is obtained as explained in Section G.2.

In Figures 33-34, we perform the same experiment as in Figure 12 and use $d = 16$ and $\sigma^2 = 4$.

Finally, in the **first column** of Figure 35, we plot the estimated Jensen-Shannon Divergence between the target samples corresponding to a randomly selected class and the diffusion particles throughout the backward trajectory. Note that this is performed in latent space. For obtaining the **middle column**, we first take all data samples from one class, embed them into the latent space and calculate the centroid corresponding to this class. Then, we normalize the centroid (making it unit norm) and plot the dot product of the particles throughout the backward diffusion process with the calculated centroid. The **right column** corresponds to the score difference. Across all experiments, we selected $\omega = 4$, sampled using DDPM (Ho et al., 2020) using 250 sampling steps, averaged over 25 samples. All other hyperparameter configurations are set to the default.

Table 3 displays the hyperparameters used to obtain the results given in Table 1. The evaluation code relied on EvalGIM library by Hall et al. (2024).

G.4 FURTHER RESULTS

Here, we detail the remaining experiments conducted. We provide the following:

- Diversity and coverage metrics corresponding to experiments in Table 1 (see Table 4)

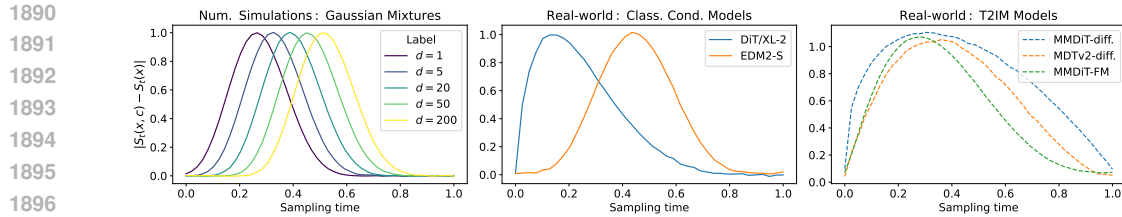


Figure 13: **Evolution of the CFG score difference, from noise ($t = 1$) to data ($t = 0$).** **Left (stand. CFG):** Numerically simulating mixture of two Gaussians: as d increases, the score difference becomes substantial earlier (this happens during Regime I). **Middle and Right (stand. CFG):** Real-world experiments using advanced models show consistent behavior with theory: monotonically increasing score difference followed by decay after a certain point.

- Ablation studies showing that Power-Law CFG outperforms standard linear CFG when changing the number of steps (see Tables 5-10)
- Sensitivity analysis showing the FID benefit for increasing value of α (see Section G.4.1, Figures 14-16)
- Further qualitative analyses of power-law CFG for either fixed ω and varying α or varying ω and varying α (see Sections G.8.1 and G.8.2)
- Further generation examples of DiT/XL-2 and MMDiT diffusion model (see Sections G.8.3 and G.8.4)

Diversity and coverage metrics. In Table 4 present additional quantitative evaluations of our method, focusing on diversity and coverage metrics (as described in Hall et al. (2024)), which complement the results shown in Table 1. Our analysis compares power-law CFG to standard CFG and state-of-the-art guidance methods, including combinations with CADS (Sadat et al., 2023) and limited-guidance (Kynkänniemi et al., 2024), which proved to be the most competitive approaches. As demonstrated in the main manuscript, power-law CFG generally outperforms standard CFG (indicated by arrows in the table). Moreover, when combined with CADS and limited-interval guidance, it yields improved results over existing methods in many cases.

Ablation studies. In Tables 5 through 10, we conduct ablation studies on two class-conditional and four text-to-image models, demonstrating that non-linear power-law CFG consistently surpasses standard CFG across varying sampling steps. The results show improved FID performance and enhanced outcomes across multiple metrics when using the non-linear approach compared to standard CFG.

Sensitivity analysis. In Section G.4.1, we present additional sensitivity analyses that build on Section 5 and Figure 5, demonstrating that high values of α consistently enhance performance, improving robustness and stability during ω tuning. As noted in the main manuscript, while power-law CFG introduces an additional hyperparameter, α , extensive hyperparameter tuning was unnecessary, with large values like $\alpha = 0.9$ consistently performing well. This is evidenced in Section G.4.1, Figures 14 to 16, which show that higher α values reliably improve FID scores. Class-conditional models (Figure 14) exhibit greater benefits than text-to-image models (Figures 15 and 16), though both show improved performance with Power-Law CFG compared to standard CFG.

Further qualitative analyses. In Sections G.8.1 and G.8.2, we provide additional qualitative examples for DiT-XL/2. Specifically, we conduct two studies: one varying the guidance parameter ω with a fixed α , and another varying α with a fixed ω . When α is fixed, increasing ω can lead to issues such as complete mode collapse (e.g., for the *jellyfish* class), oversaturation (e.g., for the *bee* class), or a significant loss of diversity (e.g., for the *dung beetle* class), which are common artifacts of standard classifier-free guidance. These effects are mitigated when using a non-linear power-law guidance approach. The second study explores the impact of increasing α while keeping ω constant, demonstrating enhanced diversity as α strength increases. In Figure 13, we plot how the score difference evolves for other CC and T2IM models used in our analyses.

1944
 1945 **Further generation examples.** In Sections G.8.3 and G.8.4, we present additional generation
 1946 examples for class-conditional (DiT/XL-2) and text-to-image (MMDiT) models, demonstrating how
 1947 power-law CFG enhances image details, thereby improving image quality and fidelity for individual
 1948 images, and increases diversity when examining a set of images for a specific class.
 1949

1950 Table 4: Comparison of EDM2-S on ImageNet-1K 512x512 data, Diffusion trained text-to-image
 1951 MMDiT on CC12m data, and Flow-matching trained text-to-image MMDiT on COCO data. **Bolded**
 1952 are the best results and underlined are the second best.
 1953

Model	EDM2-S (CC, IM-1K 512)		DiT/XL-2 (CC, IM-1K 256)		Diff. MMDiT (T2IM, CC12m)		FM MMDiT (T2IM, COCO)	
	Density	Coverage	Density	Coverage	Density	Coverage	Density	Coverage
Standard (Ho & Salimans, 2022)	0.850	0.764	0.951	0.801	1.091	0.840	0.902	0.772
Scheduler (Wang et al., 2024)	0.867	<u>0.780</u>	<u>1.117</u>	0.790	1.266	0.860	0.908	0.795
Limited (Kynkäinniemi et al., 2024)	0.845	0.777	1.130	0.840	1.258	0.857	0.915	0.808
Cosine (Gao et al., 2023)	0.850	0.769	1.102	0.822	1.106	0.840	0.920	0.802
CADS (Sadat et al., 2023)	0.854	0.765	0.999	0.853	1.222	0.860	<u>0.923</u>	0.779
APG (Sadat et al., 2024)	0.845	0.760	1.033	<u>0.867</u>	1.095	0.858	0.915	0.797
REG (Xia et al., 2024)	0.850	0.771	1.112	0.833	1.091	0.855	0.903	0.783
CFG++ (Chung et al., 2024)	N/A	N/A	N/A	N/A	1.265	0.859	0.919	0.784
Power-law CFG (Ours)	0.845 (U)	0.760 (G)	0.986 (T)	0.844 (G)	1.128 (T)	0.850 (G)	0.918 (G)	0.778 (G)
Power-law CFG + Limited (Ours)	0.850 (G)	0.778 (G)	1.115 (L)	0.835 (L)	1.286 (G)	<u>0.860</u> (G)	0.920 (G)	0.795 (L)
Power-law CFG + CADS (Ours)	0.862 (G)	0.782 (G)	1.071 (G)	0.876 (G)	<u>1.279</u> (G)	0.862 (G)	0.924 (G)	0.804 (G)

1961
 1962 Table 5: **Ablation study:** Changing the number of sampling steps for Class-conditional: DiT
 1963 ImageNet-1K 256x256
 1964

Version	Num. steps	α	ω	FID (\downarrow)	IS (\uparrow)	Precision (\uparrow)	Recall (\uparrow)	sFID (\downarrow)
Stand. CFG	50	0	1.5	3.33	259.88	0.8163	0.5474	7.406
	100	0	1.4	2.64	233.72	0.8027	0.5831	5.720
	150	0	1.3	2.38	233.52	0.8032	0.5936	5.462
	200	0	1.35	2.29	234.92	0.8031	0.5950	5.331
	250	0	1.5	2.27	278.30	0.8291	0.5840	4.601
Non-lin. CFG	50	0.6	4.35	3.03	284.55	0.8215	0.5757	7.110
	100	0.6	3.4	2.32	274.36	0.8199	0.6012	5.432
	150	0.6	3.4	2.19	274.39	0.8202	0.6071	5.512
	200	0.75	4.8	2.17	276.98	0.8204	0.5956	5.567
	250	0.75	4.85	2.05	279.90	0.8310	0.5950	4.670

1975
 1976 Table 6: **Ablation study:** Changing the number of sampling steps for Class-conditional: EDM2-S
 1977 ImageNet-1K 512x512
 1978

Version	Num. Steps	α	ω	FID (\downarrow)	α	ω	FID _{DINO} (\downarrow)
Stand. CFG	8	0	1.95	4.78	0	2.3	103.33
	16	0	1.50	2.52	0	2.3	57.47
	32	0	1.40	2.29	0	2.3	54.78
	64	0	1.50	2.25	0	2.15	54.39
Non-lin. CFG	8	0.05	2.30	4.74	-0.25	1.5	100.81
	16	0.25	2.30	2.32	-0.05	2.15	56.92
	32	0.85	11.40	1.93	0.35	2.5	52.77
	64	0.85	11.30	1.89	0.35	2.1	52.56

1998

1999 Table 7: **Ablation study:** Changing the number of sampling steps for Diffusion text-to-image:
2000 MMDiT CC12m

Version	Num. Steps	α	ω	FID (\downarrow)	Clip score (\uparrow)	Coverage (\uparrow)	Density (\uparrow)	Precision (\uparrow)	Recall (\uparrow)
2001	20	0	1.75	8.98	22.581	0.8392	1.104	0.6623	0.5545
	35	0	1.75	8.79	22.532	0.8450	1.124	0.6717	0.5590
	50	0	1.55	8.58	22.111	0.8401	1.109	0.6612	0.5692
	100	0	1.75	8.38	22.298	0.8462	1.117	0.6765	0.5698
2002	20	0.25	3.05	8.94	22.773	0.8424	1.114	0.6619	0.5495
	35	0.65	7.5	8.40	22.590	0.8491	1.126	0.6638	0.5582
	50	0.60	7.0	8.11	22.415	0.8503	1.128	0.6703	0.5532
	100	0.75	9.5	8.02	22.563	0.8472	1.115	0.6747	0.5723

2003

2004 Table 8: **Ablation study:** Changing the number of sampling steps for Diffusion text-to-image:
2005 MDTv2 ImageNet-1K 512x512

Version	Num. Steps	α	ω	FID (\downarrow)	Clip score (\uparrow)	Coverage (\uparrow)	Density (\uparrow)	Precision (\uparrow)	Recall (\uparrow)
2011	20	0	1.55	5.30	23.949	0.8218	1.167	0.7475	0.5133
	30	0	1.55	4.09	23.998	0.8292	1.233	0.7492	0.5264
	40	0	1.6	3.85	24.011	0.8311	1.178	0.7602	0.5294
	50	0	1.2	3.68	24.306	0.8318	1.150	0.7510	0.5989
2012	20	0.6	6.0	4.88	24.154	0.8251	1.236	0.7503	0.4916
	30	0.6	6.0	4.03	24.033	0.8344	1.205	0.7583	0.5332
	40	0.7	7.0	3.73	23.367	0.8353	1.181	0.7557	0.5546
	50	0.8	8.5	3.57	25.339	0.8361	1.170	0.7513	0.5609

2013

2014 Table 9: **Ablation study:** Changing the number of sampling steps for Flow-Matching text-to-image:
2015 MMDiT on COCO

Version	Num. Steps	α	ω	FID (\downarrow)	Clip score (\uparrow)	Coverage (\uparrow)	Density (\uparrow)	Precision (\uparrow)	Recall (\uparrow)
2021	20	0	2.85	6.84	26.373	0.7529	0.8820	0.6121	0.5604
	30	0	1.95	5.84	25.948	0.7581	0.8668	0.6051	0.5879
	40	0	2.05	5.62	25.817	0.7651	0.8798	0.6091	0.5978
	50	0	2.00	5.20	25.714	0.7726	0.9026	0.6299	0.5940
2022	20	0.5	9.75	6.47	25.981	0.7241	0.7762	0.5719	0.5851
	30	0.5	9.45	5.62	26.003	0.7577	0.8457	0.6105	0.5874
	40	0.6	9.05	5.45	25.113	0.7633	0.8549	0.6149	0.6030
	50	0.7	10.15	4.81	25.848	0.7782	0.9183	0.6208	0.6191

2016

2017 Table 10: **Ablation study:** Changing the number of sampling steps for Flow-Matching text-to-image:
2018 MMDiT on CC12m

Version	Num. Steps	α	ω	FID (\downarrow)	Clip score (\uparrow)	Coverage (\uparrow)	Density (\uparrow)	Precision (\uparrow)	Recall (\uparrow)
2031	20	0	2.75	10.75	25.224	0.8289	1.069	0.6396	0.5803
	30	0	1.95	9.85	24.935	0.8318	1.068	0.6946	0.6000
	40	0	2.0	9.50	25.018	0.8461	1.103	0.7064	0.5907
	50	0	2.1	9.46	25.133	0.8520	1.145	0.7159	0.5946
2032	20	0.2	3.25	10.68	25.585	0.8301	1.075	0.7101	0.5815
	30	0.5	10.0	9.81	25.002	0.8338	1.085	0.6968	0.5909
	40	0.6	9.35	9.17	24.794	0.8352	1.087	0.6909	0.6030
	50	0.6	8.05	9.00	24.723	0.8397	1.087	0.6911	0.6023

2033

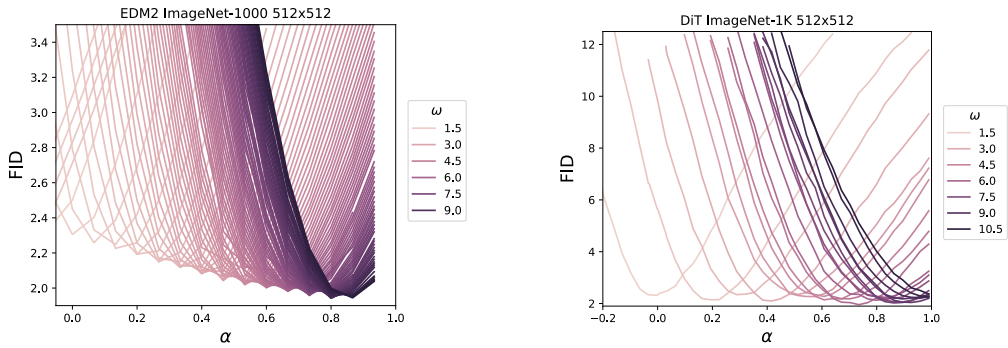
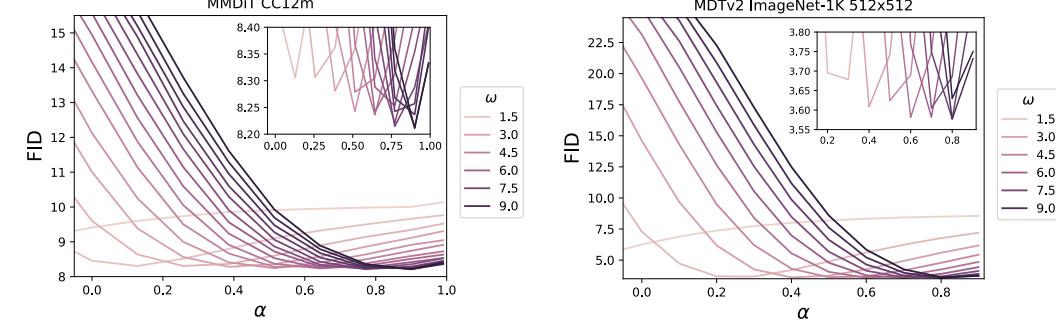
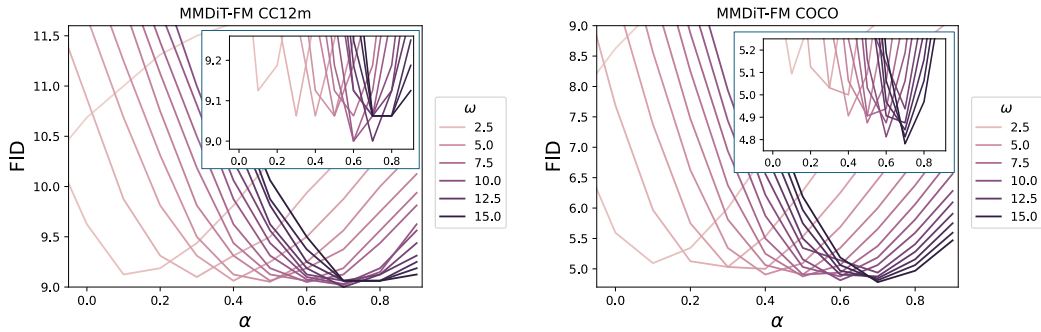
2041 In the following experiments, we have trained a U-ViT-like model (Bao et al., 2022) on lower-dimensional datasets to confirm that nonlinear CFG provides further improvements to standard CFG in lower-dimensional settings. For CIFAR10 the architecture closely mimics that of U-ViT-S/2 and for ImageNet64x64 and ImageNet32x32 U-ViT-M/4. We have obtained ImageNet32x32 by using bilinear downsampling on ImageNet64x64.

2042

G.5 LOW-DIMENSIONAL EXPERIMENTS

2043

2044 Regarding sampling, for CIFAR10 we used *'euler_maruyama_sde'* sampler with a maximum of 1000
2045 steps (we did not find further improvement by further increasing step size). For ImageNet32x32 and
2046 ImageNet64x64 we used *'dpm_solver'* with a maximum number of sampling steps equal to 100 (we
2047 did not find improvements by further increasing it from 100).

2052 G.4.1 SENSITIVITY ANALYSIS
20532066 Figure 14: **Class-conditional diffusion**: image quality benefits from non-linear scheme, yielding
2067 lower FID for larger values of α .2082 Figure 15: **Text-to-image diffusion models**: image quality benefits from non-linear scheme, yielding
2083 lower FID for larger values of α .2098 Figure 16: **Text-to-image flow matching**: image quality benefits from non-linear scheme, yielding
2099 lower FID for larger values of α .2103 The results from the first experiment, showing the lower-dimensional improvements in FID can be
2104 seen in Tables 10-12, whereas the experiment of choosing very small guidance scale can be seen
2105 in Table 13. The findings are as follows: as the dimension decreases and the unwanted effects of
CFG get stronger, the benefit from applying non-linear CFG further increases, as can be seen from a

2106
 2107 **Table 11: Comparison of CFG variants on ImageNet-1K (pixel space)** for Matryoshka Diffusion and
 2108 Pixelflow Flow Matching. Second row represents the performance with fixed $\alpha = 0.9$, last row with tuned α .

Version	Matryoshka Diffusion (Gu et al., 2023)			Pixelflow Flow Matching (Chen et al., 2025b)		
	FID \downarrow	Prec \uparrow	Rec \uparrow	FID \downarrow	Prec \uparrow	Rec \uparrow
Standard CFG	3.51	0.81	0.54	2.43	0.83	0.56
Nonlinear CFG ($\alpha=0.9$)	3.39	0.82	0.55	2.29	0.83	0.58
Nonlinear CFG ($\alpha=0.65/0.45$)	3.17	0.83	0.56	2.12	0.85	0.59

2113
 2114
 2115 more pronounced improvemenet in FID. Secondly, for very small ω , the performance of linear and
 2116 non-linear CFG equals that of the conditional, unguided model.

2117
 2118 **G.6 NUMERICAL SIMULATIONS: MIXTURES OF GAUSSIANS WITH DIFFERENT MEANS,
 2119 VARIANCES AND MIXTURE PROBABILITIES**

2120 In this section, we present experimental results comparing standard Classifier-Free Guidance (CFG)
 2121 and Nonlinear CFG on Gaussian mixtures with 3 and 4 components.

2122
 2123
 2124 **Experiment 1: 3-Component Gaussian Mixture ($d = 2$)** We first investigate a two-dimensional
 2125 ($d = 2$) setting using a Gaussian mixture model composed of 3 components with assignment prob-
 2126 abilities of 30%, 40%, and 30%.

2127 The results align with our two-mixture Gaussian analysis:

2128

- Standard CFG, especially with strong guidance parameters, can induce **unwanted effects** (as shown in Figure 17).
- By selecting Nonlinear Guidance with $\alpha \neq 0$, these negative effects can be **dampened** (as shown in Figure 18).

2134
 2135 **Experiment 2: 4-Component Gaussian Mixture ($d = 2$ vs. $d = 1000$)** The second exper-
 2136 iment examines the improvements offered by Nonlinear Guidance over standard CFG, as well as
 2137 the mitigating effect of high dimensionality on CFG’s unwanted behaviors. We use a 4-component
 2138 Gaussian mixture for a small-dimensional experiment ($d = 2$) and a large-dimensional experiment
 2139 ($d = 1000$).

2140 The findings are consistent with the two-Gaussian component analysis (and can be seen in Figures
 2141 19 and 20):

2142

1. Nonlinear CFG effectively **dampens** the effects of **mean overshoot** and **variance shrink-
 2143 age** induced by standard CFG.
2. As the dimensionality (d) increases, the **mean overshoot** and **variance shrinkage** effects
 2144 associated with standard CFG **diminish**.

2145
 2146 **G.7 RESULTS FOR PIXEL-SPACE VS LATENT SPACE**

2147 Here, we provide the table for the experiment conducted in Section 5.3. We show that the benefit
 2148 of power-law CFG can also be observed when applying non-linear guidance in pixel space, and not
 2149 just latent space.

2150
 2151 **G.8 ROBUSTNESS ANALYSIS: RESOLUTION, SCHEDULING, AND ALTERNATIVE METRICS**

2152 In this section, we discuss the robustness of the Power-Law formulation across different vector
 2153 norms (resolution), noise schedules, and distance metrics.

2154 **Resolution and Vector Norms.** In high-dimensional spaces, the vector norm of the score difference
 2155 is sensitive to the dimensionality of the data (e.g., a 512^2 pixel-space image vs. a 32^2 latent).

2160
 2161 Table 12: Comparison of Standard CFG, Cosine-based variants, and Power-Law (Nonlinear) CFG
 2162 on EDM-2/S ImageNet-1K (512×512).

2170 2171 2172 2173 2174 2175 2176 2177 2178 2179 2180 2181 2182 2183 2184 2185 2186 2187 2188 2189 2190 2191 2192 2193 2194 2195 2196 2197 2198 2199 2200 2201 2202 2203 2204 2205 2206 2207 2208 2209 2210 2211 2212 2213	2170 2171 2172 2173 2174 2175 2176 2177 2178 2179 2180 2181 2182 2183 2184 2185 2186 2187 2188 2189 2190 2191 2192 2193 2194 2195 2196 2197 2198 2199 2200 2201 2202 2203 2204 2205 2206 2207 2208 2209 2210 2211 2212 2213	Version	FID \downarrow	FID DINO \downarrow
2170 Standard CFG	2171 2.29	2172 54.76		
2170 Cosine CFG	2171 2.26	2172 54.28		
2170 Cosine CFG w. α	2171 2.21	2172 54.09		
2170 Nonlinear CFG (Ours)	2171 1.93	2172 52.77		

2170 While the intrinsic manifold dimensionality may remain similar, the Euclidean norm scales with
 2171 resolution. Theoretically, the overall shape of the score difference curve remains consistent (hump-
 2172 shaped behavior tending to zero at $t \rightarrow 0$ and $t \rightarrow 1$), but the absolute scale changes. In the context
 2173 of Power-Law CFG, this resolution-based scaling is effectively managed by the renormalization
 2174 provided by the hyperparameters; Specifically, choosing the optimal guidance scale ω renormalizes
 2175 the score difference for the given resolution regime. We validated this by evaluating Power-Law
 2176 CFG on pixel-space methods (Matryoshka-diffusion (Gu et al., 2023) and PixelFlow (Chen et al.,
 2177 2025b)), confirming that the method generalizes robustly to high-resolution pixel space without
 2178 requiring explicit resolution-based formulation changes.

2179 **Noise Schedule Scaling.** The magnitude of the score difference is naturally influenced by the dif-
 2180 fusion time t (and consequently σ_t). While one could theoretically define a schedule-specific non-
 2181 linear guidance of the form $\phi_t(s, \sigma_t) = s^\alpha f(\sigma_t)$ to decouple these effects, we find that the standard
 2182 Power-Law formulation is sufficient to improve upon standard CFG. The exponential decay of the
 2183 score difference at boundary times theoretically mitigates the need for complex, schedule-dependent
 2184 scaling functions $f(\sigma_t)$ in high dimensions, but we suspect further empirical improvements might
 2185 be observed by tuning for optimal $f(\sigma_t)$.

2186 **Euclidean Difference vs. Cosine Distance.** Finally, we investigated whether the performance
 2187 gain of Power-Law CFG stems purely from directional alignment or if the magnitude of the score
 2188 difference is essential. We compared our method against "Cosine CFG," where the guidance is
 2189 scaled based on the cosine distance (purely directional), and "Cosine CFG w. α ," where the cosine
 2190 distance is raised to a power α . We evaluated these variants using EDM-2/S on ImageNet (512×512
 2191 latent space). As shown in Table 12, while using Cosine distance improves over standard CFG,
 2192 it does not match the performance of Power-Law CFG. This suggests that the "built-in" scaling
 2193 provided by the Euclidean norm—which accounts for both the angular difference and the relative
 2194 magnitude of the conditional and unconditional scores—is a critical component of effective non-
 2195 linear guidance.

Version	Num. steps	α	ω	FID (↓)	Precision (↑)	Recall (↑)
Lin. CFG	100	0	1.55	3.50	0.6569	0.5932
	250	0	1.40	2.77	0.6938	0.6115
	500	0	1.35	2.03	0.6894	0.6262
	1000	0	1.45	1.80	0.7071	0.6186
Nonlin. CFG	0	100	0.9	3.90	2.94	0.6653
	250	0.9	4.35	2.16	0.6688	0.6298
	500	0.9	4.35	1.62	0.6688	0.6298
	1000	0.9	4.75	1.48	0.7228	0.6506

Table 13: CIFAR-10 Results

Version	Num. steps	α	ω	FID (↓)	Precision (↑)	Recall (↑)
Lin. CFG	25	0	1.55	5.81	0.3842	0.4632
	50	0	1.40	4.01	0.4161	0.4750
	75	0	1.60	3.81	0.4120	0.4724
	100	0	1.65	3.35	0.4306	0.4967
Nonlin. CFG	25	0.9	3.40	4.97	0.4022	0.4564
	50	0.9	3.35	3.90	0.4241	0.4672
	75	0.9	3.40	3.33	0.4431	0.5050
	100	0.9	3.85	2.88	0.4539	0.5263

Table 14: IMNET-32 Results

Version	Num. steps	α	ω	FID (↓)	Precision (↑)	Recall (↑)
Lin. CFG	25	0	1.60	5.32	0.3996	0.4845
	50	0	1.80	4.48	0.4484	0.4962
	75	0	1.70	4.37	0.4576	0.5137
	100	0	1.75	4.34	0.4511	0.5267
Nonlin. CFG	25	0.9	3.80	4.76	0.4212	0.4718
	50	0.9	4.00	4.02	0.4656	0.5183
	75	0.9	4.20	3.75	0.4734	0.5512
	100	0.9	4.15	3.71	0.4883	0.5563

Table 15: IMNET-64 Results

Method	CIFAR-10 FID (\downarrow)	IMNET-32 FID (\downarrow)	IMNET-64 FID (\downarrow)
Uncond.	3.142	3.891	5.930
Cond.	2.401	3.167	4.277
Lin. CFG w. $\omega + \epsilon$	2.400	3.176	4.299
Nonlin. CFG w. $\omega + \epsilon$	2.399	3.194	4.285

Table 16: FID Comparison Across Datasets

GMM Diffusion Sampling with Standard Classifier-Free Guidance

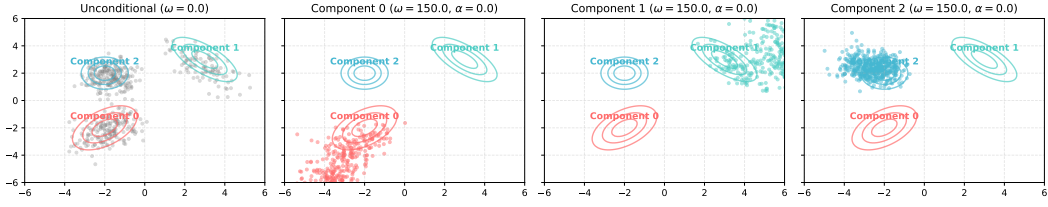


Figure 17: Numerical simulation of Standard CFG in a mixture of 3 Gaussians

GMM Diffusion Sampling with Nonlinear Classifier-Free Guidance

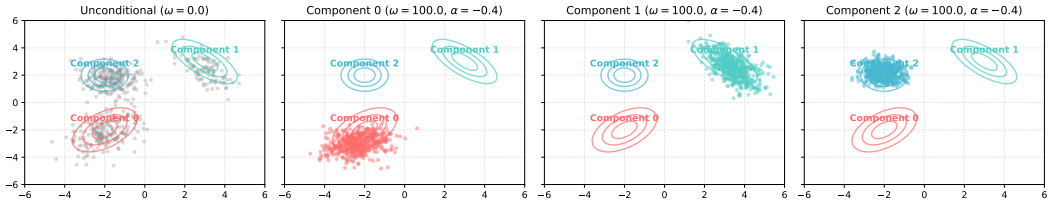


Figure 18: Numerical simulation of Nonlinear CFG in a mixture of 3 Gaussians

Projection Histograms for 4-Component GMM (D=2, \omega = 100.0, \alpha = 0.9)

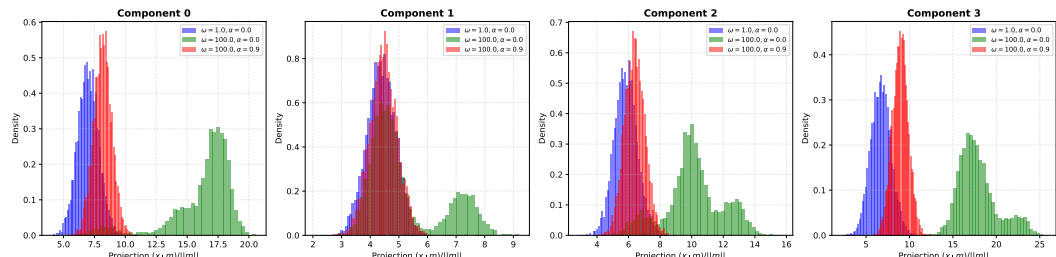


Figure 19: Numerical simulation of Standard CFG in a mixture of 4 Gaussians

Projection Histograms for 4-Component GMM (D=1000, \omega = 100, \alpha = 0.9)

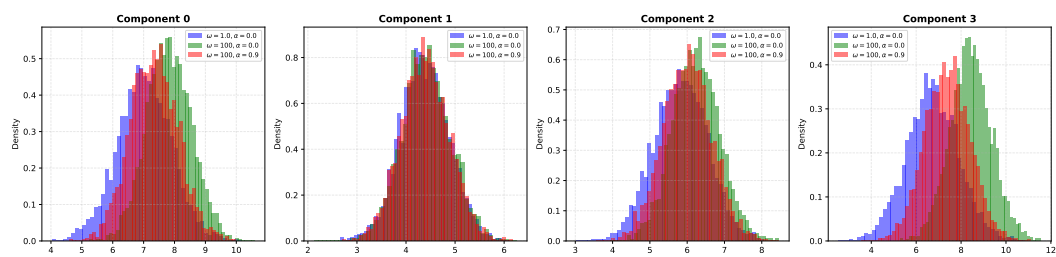
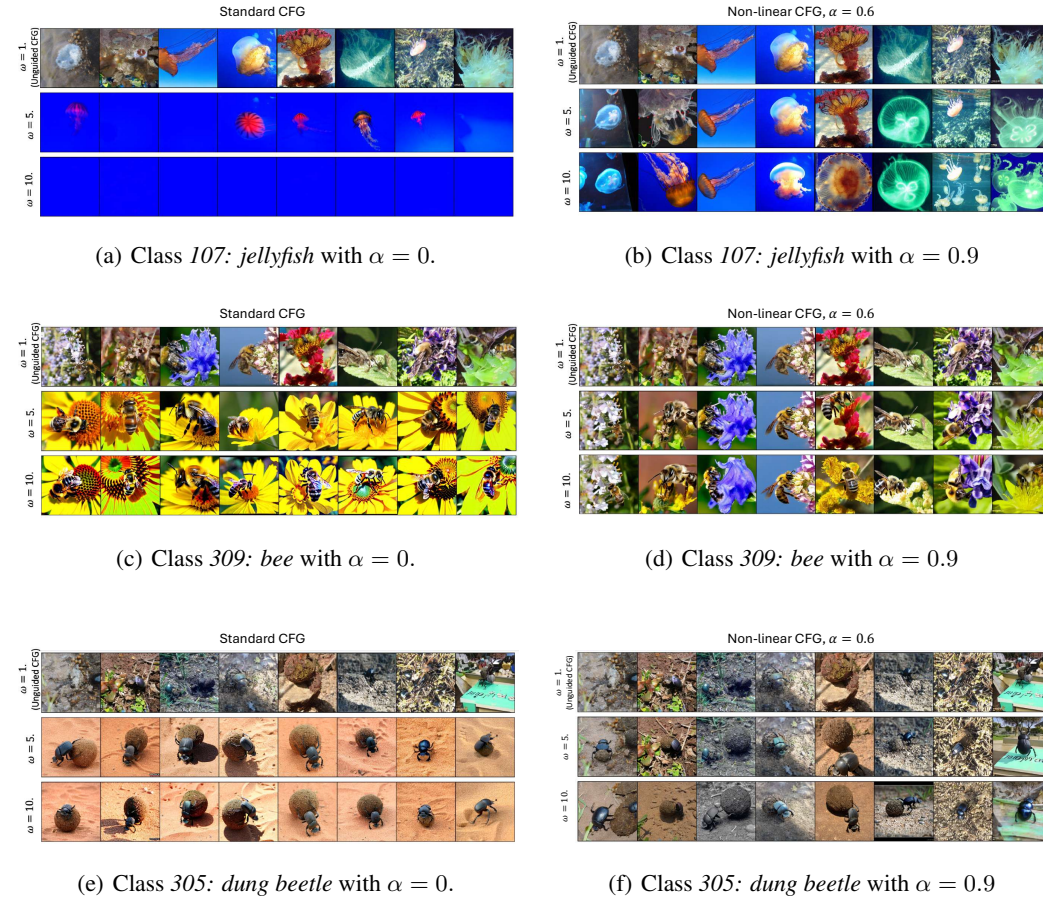
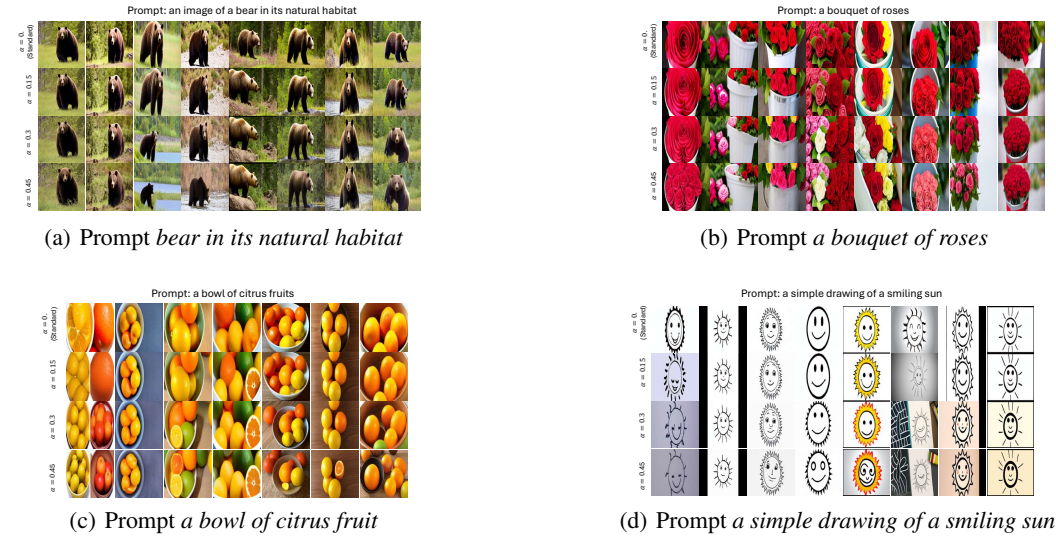
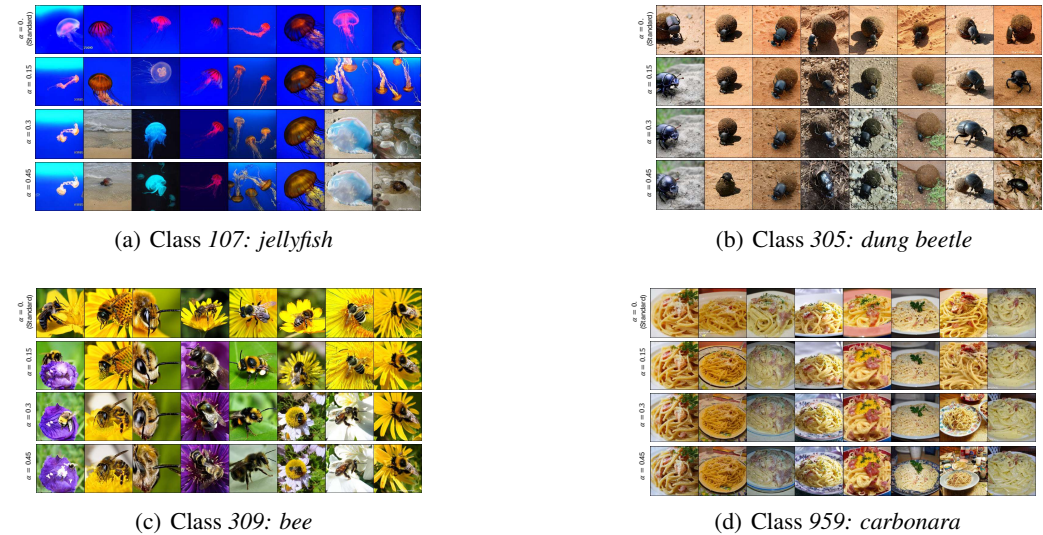
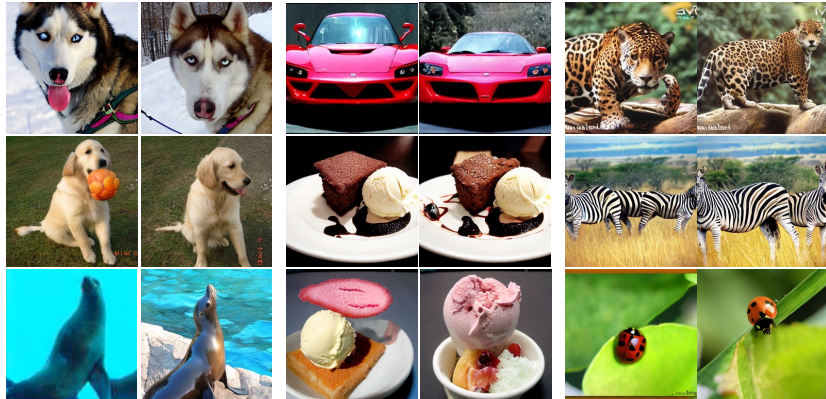


Figure 20: Numerical simulation of Nonlinear CFG in a mixture of 3 Gaussians

2322 G.8.1 QUALITATIVE ANALYSIS: VARYING ω , FIXED α .2355 Figure 21: Generated images for different classes for varying values of ω and α . Each panel shows
2356 the effect of changing α from 0 to 0.9, demonstrating the impact on diversity and image quality.

2376 G.8.2 QUALITATIVE ANALYSIS: FIXED ω , VARYING α .
2377Figure 22: T2IM generated images for different prompts with $\omega = 4.$ and varying value of α .Figure 23: CC generated images for different classes with $\omega = 4.$ and varying value of α .

2430
2431 G.8.3 GENERATED IMAGES BY DiT/XL-2 (256x256)2446 Figure 24: Additional examples generated by DiT/XL-2 using Standard CFG ($\omega = 4$) and Power-
2447 Law CFG ($\omega = 8$, $\alpha = 0.7$). Image pairs start from the same noise (same seed). The resulting pairs
2448 represent Standard CFG on the left and Power-Law CFG on the right.2459 Figure 25: Gen. images conditioned on the class *pineapple* with Standard CFG
2460 ($\omega = 4$).2470 Figure 26: Gen. images conditioned on class *pineapple* with Power-Law CFG
2471 ($\omega = 8, \alpha = 0.7$).

2484

2485

2486

2487

2488

2489

2490

2491

2492

2493

2494

2495

2496



2497 Figure 27: Gen. images conditioned on the class *water ouzel, dipper* using Standard CFG with
2498 $\omega = 4$.

2499

2500

2501

2502

2503

2504

2505

2506

2507

2508



2509 Figure 28: Gen. images conditioned on the class *water ouzel, dipper* using Power-Law CFG
2510 with $\omega = 8, \alpha = 0.7$.

2511

2512

2513

2514

2515

2516

2517

2518

2519

2520

2521



2522 Figure 29: Gen. images conditioned on the class *vine snake* using Standard CFG with $\omega = 4$.

2523

2524

2525

2526

2527

2528

2529

2530

2531

2532

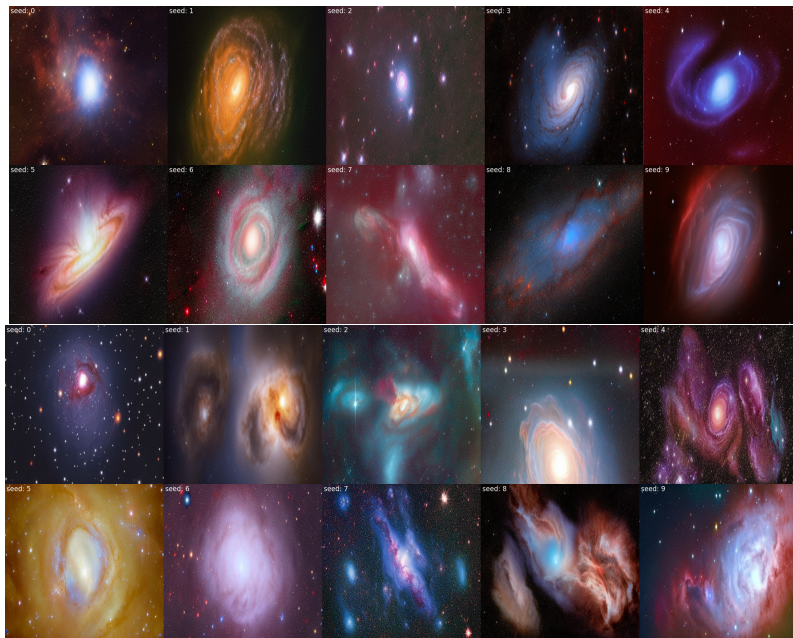


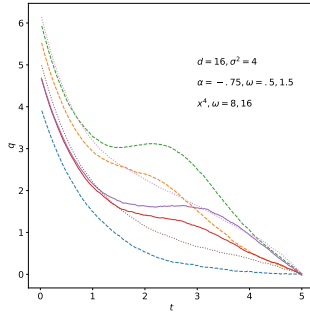
2533 Figure 30: Gen. images conditioned on the class *vine snake* using Power-Law CFG with $\omega =$
2534 $8, \alpha = 0.7$.

2535

2536

2537

2538
2539 G.8.4 GENERATED IMAGES BY MMDiT MODEL (DIFFUSION OBJECTIVE, RESOLUTION
2540 512x512)
25412550
2551 Figure 31: Images generated conditioned on the textual prompt *Glowing mushrooms in a*
2552 *dark forest.* using Standard CFG with $\omega = 3$ (top two rows) and Power-Law CFG with
2553 $\omega = 10, \alpha = 0.8$ (bottom two rows).
25542555
2556 Figure 32: Images generated conditioned on the textual prompt *Stunning, breathtaking view of a*
2557 *galaxy or nebula* using Standard CFG with $\omega = 3$ (top two rows) and Power-Law CFG with
2558 $\omega = 10, \alpha = 0.8$ (bottom two rows).
25592560
2561
2562
2563
2564
2565
2566
2567
2568
2569
2570
2571
2572
2573
2574
2575
2576
2577
2578
2579
2580
2581
2582
2583

2592 **H FURTHER NOTES ON NON-LINEAR CFG**
2593

2607 Figure 33: $\langle q \rangle$ versus time in the Gaussian binary mixture with $d = 16$ and $\sigma^2 = 4$. The dashed
2608 line are obtained by the standard linear CFG with $\omega = 0, 8, 16$ from bottom to top. The dotted line
2609 are obtained with the Power-Law non-linear scheme $f(x) = \omega x^{-.75}$ with $\omega = .5, 1.5$ from bottom
2610 to top. The full lines are obtained with the non-linear guidance of Eq.(44) with $\gamma = 4$ and $\omega = 8, 16$ from
2611 bottom to top. The Rescaled Power-law non-linear scheme departs from $q = 0$ at large time
2612 on a trajectory similar to the linear scheme and to the Power-Law non-linear scheme. But it gives a
2613 smaller bias at $t = 0$.

2614 The first non-linear CFG proposal, the power-law CFG with $\phi_t(s) = \omega s^\alpha$ and $\alpha > -1$ (in main
2615 paper we focus on $\alpha > 0$ but the guidance can be applied in fact for any $\alpha > -1$) results in the
2616 following guidance scheme:

2617
$$\vec{S}_t^{\text{PL}}(\vec{x}, c) = S_t(\vec{x}, c) + \omega [S_t(\vec{x}, c) - S_t(\vec{x})] \left| \vec{S}_t(\vec{x}, c) - \vec{S}_t(\vec{x}) \right|^\alpha. \quad (43)$$

2618 As mentioned, the ℓ_2 distance between scores $\delta S_t = |\vec{S}_t(\vec{x}, c) - \vec{S}_t(\vec{x})|$ is exponentially small
2619 both at the beginning of the backward process (as both conditional and unconditional distributions
2620 are standard Gaussian clouds) and before exiting Regime I (as shown in Section 4), after which it
2621 remains zero. This non-linear scheme automatically switches off in Regime II and has the following
2622 properties: choosing $\alpha < 0$ provides guidance which speeds up convergence to the target at early
2623 times, while $\alpha > 0$ dampens the guidance for small δS_t and strengthens it for large δS_t . In practice,
2624 we found positive values for α to perform best. In numerical experiments for finite dimension it
2625 biases the distribution obtained at $t = 0$ (see Fig.35).

2626 One would like to have different non-linearities applying to the regimes $t \gg t_s$ and $t < t_s$. One
2627 possibility is to use the following version, which extends to more general effective distributions
2628 $P_0(\vec{a})e^{-\vec{a}^2 s(t)/(2s(t)^2 \sigma(t)^2)}$ with non-standard $s(t)$ and $\sigma(t)$.

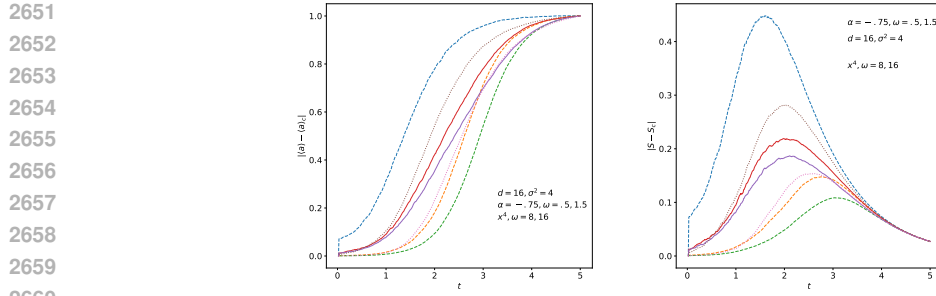
2629 **Rescaled Power-law CFG.** Here, by denoting with $\langle \cdot \rangle$ the expectation w.r.t. the effective distribution
2630 $P_0(\vec{a})e^{-\vec{a}^2 s(t)/(2s(t)^2 \sigma(t)^2)}$, the score difference can be expressed as $|\vec{S}_t(\vec{x}, c) - \vec{S}_t(\vec{x})| =$
2631 $(1/(s(t)\sigma(t)^2)) |\langle \vec{a} \rangle_{\vec{x}, c} - \langle \vec{a} \rangle_{\vec{x}}|$, where $s(t)$ and $\sigma(t)$ are related to the functions $f(t)$ and $g(t)$ by
2632 $s(t) = \exp \int_0^t d\tau f(\tau)$ and $\sigma(t) = \int_0^t d\tau g(\tau)^2 / s(\tau)^2$. Therefore the non-linear function depends
2633 on the difference between the estimators of the initial value \vec{a} , given $\vec{x}(t)$, in the class and in the
2634 full distribution. This difference is typically a function that decreases with the time of the backward
2635 process. This suggests to use a non-linear CFG of the form

2636
$$\begin{aligned} \vec{S}_t^{\text{RPL}}(\vec{x}, c) &= \vec{S}_t(\vec{x}, c) + \omega \left[\vec{S}_t(\vec{x}, c) - \vec{S}_t(\vec{x}) \right] \left| \langle \vec{a} \rangle_{\vec{x}, c} - \langle \vec{a} \rangle_{\vec{x}} \right|^\gamma \\ &= \vec{S}_t(\vec{x}, c) + \omega \left[\vec{S}_t(\vec{x}, c) - \vec{S}_t(\vec{x}) \right] \left| \vec{S}_t(\vec{x}, c) - \vec{S}_t(\vec{x}) \right|^\gamma s(t)^\gamma \sigma(t)^{2\gamma}, \end{aligned} \quad (44)$$

2637 with positive γ . As we will show in Figures 33-34, this non-linear guidance term has interesting
2638 performance in terms of combining a rapid drift toward the desired class c at early stages of the
2639 backward process together with small bias in the finite distribution in finite dimensional problems.

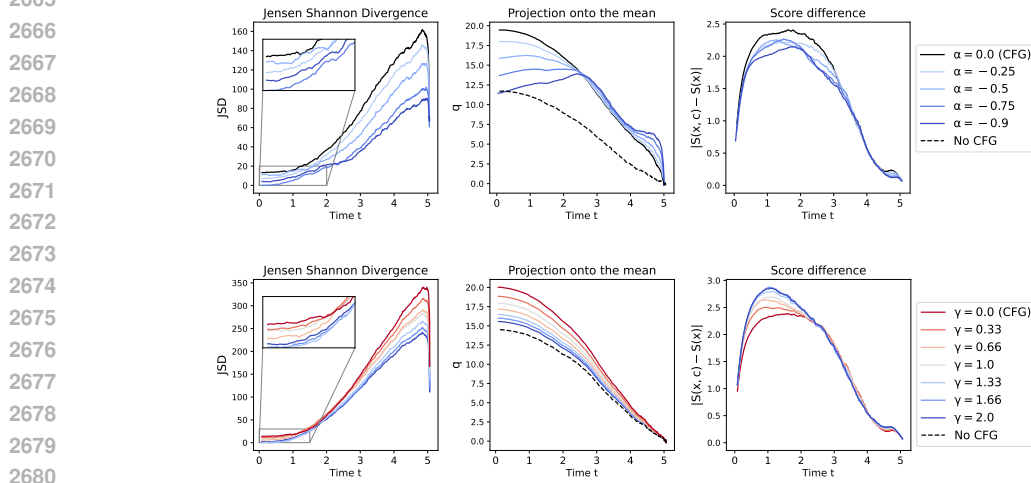
2646 The behavior of both versions is portrayed in Figure 35: both non-lin. versions yield smaller bias
 2647 at $t = 0$. Furthermore, Figure 35 also displays additional experiments highlighting the benefits of
 2648 non-linear versions.
 2649

2650



2661 Figure 34: We perform the same experiment as in Fig. 33. Left: the value of $|\langle \vec{a} \rangle_{\vec{x}=\vec{0},c} - \langle \vec{a} \rangle_{\vec{x}=\vec{0}}|$.
 2662 Right: the value of $|S_t(\vec{x}, a) - S_t(\vec{x})|$, with the same linestyle and color code as in Fig. 33.

2663



2664 Figure 35: Real-world experiments using DiT/XL-2 (Peebles & Xie, 2023) trained on ImageNet-
 2665 1000 (Deng et al., 2009): randomly selected class with $\omega = 4$, using DDPM (Ho et al., 2020)
 2666 with 250 sampling steps, averaged over 25 samples. **First column:** Power-Law CFG. **Second**
 2667 **column:** Rescaled Power-Law CFG (44). **Left column:** Jensen-Shannon Divergence between the
 2668 embedded data points corresponding to randomly selected class and the generated samples as a
 2669 function of reverse time τ . **Middle column:** mean dot product of the normalized class centroid
 2670 and the diffusion trajectories $\vec{x} \cdot \vec{c}_i / \|\vec{c}_i\|$ (both in the latent space) as a function of reverse time τ .
 2671 **Right column:** Evolution of the distance between conditional and unconditional scores. From all
 2672 three plots, we can see that using first (second) version of non-linear CFG with $\alpha < 0$ ($\gamma > 0$)
 2673 results in paths that have smaller JSD, estimated as in Wang et al. (2009), throughout the whole
 2674 trajectory and smaller overshoot of the distribution's mean at $\tau = 0$. We can also see that the
 2675 score difference $|S_\tau(x, c) - S_\tau(x)|$ has the same qualitative behavior as in numerical simulations of
 2676 Gaussian mixtures.
 2677

2678

2679

2680

2681

2682

2683

2684

2685

2686